

MSURJ

MCGILL SCIENCE UNDERGRADUATE RESEARCH JOURNAL

VOLUME 5 | ISSUE 1 | MARCH 2010

MSURJ.MCGILL.CA



101010110
10101

0101011010101

11010
1001011010
1010100

01010110101

001101010101001010101

**SCIENTIA EST
POTENTIA** KNOWLEDGE IS POWER

**ON
THE
COVER**

DESIGNED BY TEAGAN WHITE

The front cover features an illustration of a dragonfly, illustrating the interwoven nature of the different disciplines of science, and celebrating of the International Year of Biodiversity. The back cover features illustrations from René Descartes, the 17th century French philosopher and mathematician, hypothesizing about the nature of the universe. Though the Cartesian universe has long been replaced by one infinitely more complex, the legacy of scientists past, an unwavering pursuit for knowledge, remains with us today.

**THE
2009-2010
MSURJ
COMMITTEE**

MCGILL SCIENCE UNDERGRADUATE RESEARCH JOURNAL 805 SHERBROOKE ST. WEST ROOM 1B21 MONTREAL, QUEBEC, H3A 2K6 CANADA

EDITORS-IN-CHIEF

MARZIEH GHIASI (ANATOMY AND CELL BIOLOGY)
DANIEL TING (MICROBIOLOGY AND IMMUNOLOGY)

MANAGING EDITOR

ERIC ECKBO (PSYCHOLOGY)

ASSOCIATE EDITOR

DANIEL FRIEDLANDER (BIOMEDICAL SCIENCES
AND PHILOSOPHY)

BOARD OF EDITORS

EMILY FOXEN-CRAFT (PSYCHOLOGY)
YI 'ARIEL' LIU (BIOCHEMISTRY)
ALEXIS MALOZEMOFF (COMPUTER SCIENCE)
ERIN MAY (BIOCHEMISTRY)
MICHELLE MAYER (ANATOMY & CELL BIOLOGY)
LAKSH PURI (PSYCHOLOGY)
MICHAEL WALES (PHYSICS B.S., LAW)
MARNIE WILSON (MICROBIOLOGY & IMMUNOLOGY)
LISA ZHANG (IMMUNOLOGY)
ERIC ZHAO (PHYSICS)

ASSISTANT EDITOR

NEIL ISSAR (BIOLOGY)

FACULTY OF SCIENCE ADVISOR

VICTOR CHISHOLM (OFFICE FOR UNDERGRADUATE
RESEARCH IN SCIENCE)

LAYOUT DESIGNER

ARLENE BAACO (ARLENE.BAACO@GMAIL.COM)

GRAPHIC DESIGNER

TEAGAN WHITE (TEAGAN_WHITE@HOTMAIL.COM)

P. 514.398.6979
F. 514.398.6766
E. MCGILLSURJ@GMAIL.COM
W. MSURJ.MCGILL.CA

07	FORWARD
09	ACKNOWLEDGEMENTS
11	Ehsan Dadvar GENOMIC AND PHENOTYPIC VARIABILITY OF MYCOBACTERIUM AVIUM SUBSPECIES
18	Amanda Grant-Orser, Fabio Canneva ERK-CREB SIGNALING DYSREGULATION WITH INCREASING LEVELS OF THE β -AMYLOID PROTEIN
24	Mina Khorashadi DIFFERENTIAL EFFECTS OF ESTROGEN ON MEMORY PROCESSES AND LEARNING STRATEGIES: A SELECTIVE REVIEW OF ANIMAL STUDIES
30	Emily R. Lindemer, Ali Syed THE DISCRIMINATION OF CORRELATED AND ANTI-CORRELATED MOTION IN THE HUMAN VISUAL SYSTEM
35	Lai Chung Liu, Bradley J. Siwick A NEW SOFTWARE PACKAGE TO STIMULATE THE PATTERN OF PROPOSED TRANSIENT CHEMICAL STRUCTURES USING THE MULTISLICE SIMULATION OF THE DEBYE-SCHERRER DIFFRACTION PATTERN FOR GOLD NANOPARTICLES
42	Vimarsha Swami, Lorraine E. Chalifour BISPHENOL A IMPACTS CARDIOMYOCYTE DIFFERENTIATION IN VITRO BY MODULATING CARDIAC PROTEIN EXPRESSION
49	David A. Tiberi, Minseon Kim NEW INSIGHTS INTO TEMPLATE-BASED PROTEIN MODELING TECHNIQUES
55	Kerry Weinstein, Zofia Czajkowska, Amélie Nantel-Vivier, Robert O. Pihl CAFFEINATED ALCOHOLIC BEVERAGE CONSUMPTION IS ASSOCIATED WITH BINGE DRINKING AMONG CANADIAN COLLEGE STUDENTS
61	Marnie Goodwin Wilson, Thi Lien-Anh Nguyen, Laura Shulak, Peyman Nakhaei, John Hiscott EPIGENETIC MODIFIERS ENHANCE VESICULAR STOMATITIS VIRUS-MEDIATED ONCOLYSIS IN THE REFRACTORY PC3 CELL LINE
67	Simon Yang, David A. Carozza, Lawrence A. Mysak RE-TUNING THE WALKER-KASTING GLOBAL CARBON CYCLE BOX MODEL USING A PARAMETER SENSITIVITY ANALYSIS

FORWARD

DEAR READER,

Undergraduate research has a long history at McGill University. In the 1950s, Thomas Chang developed the first artificial cells in his dormitory in Douglas Residence Hall. Two decades later, Jack Szostak launched his research career as a McGill undergraduate, a career that culminated in the 2009 Nobel Prize in Physiology or Medicine. This tradition has enriched the pre-eminent scientific research done at McGill and must continue to be cultivated.

In 2006, McGill students took a major step in addressing this need by founding the McGill Science Undergraduate Research Journal (*MSURJ*). *MSURJ* was the first peer-reviewed undergraduate scientific journal in Canada, and since its inception has inspired the founding of other scientific journals across the country. While our mission is to promote and publish undergraduate research, our mandate extends to promoting effective communication in science. We therefore make a concerted effort to present our articles with clear and accessible writing.

This year, we have implemented two major initiatives aimed at increasing the breadth and scope of our journal. We partnered with Professor Linda Cooper, an expert in scientific writing, to actively instruct our editorial board in the proper organization and presentation of scientific results. These lessons ensured a higher standard of writing clarity in our publication. We also implemented a community outreach program aimed at science students at local CÉGEPs, encouraging them to become involved in research as undergraduates and to develop strong writing habits.

Part of our strength at *MSURJ* derives from our multidisciplinary nature. Members of our editorial board are from diverse backgrounds and represent a wide-range of departments. Furthermore, the articles in this issue represent domains that range from structural bioinformatics to psychology to physical chemistry. Our hope is that this diversity will allow you, the reader, to sample the range of possibilities at McGill, and to open your eyes to the new paths being forged by young investigators in science.

MARZIEH GHIASI AND DANIEL TING

EDITORS-IN-CHIEF

ACKNOWLEDGEMENTS

The launch of the fifth edition of the McGill Science Undergraduate Research Journal would not have been possible without the support of many individuals.

We thank Professor Martin Grant, Dean of the Faculty of Science, whose unwavering support throughout the past five years has allowed this journal to flourish.

We thank all of our donors in the McGill community for their generous support

Biochemistry Undergraduate Society
Chemistry Undergraduate Student Society
Department of Earth & Planetary Sciences
Faculty of Medicine
Faculty of Science
McGill Alumni Association
McGill Anatomy and Cell biology Student Society
School of Environment
Science Undergraduate Society
SSMU Campus Life Fund

We also extend our gratitude to

Mr. Victor Chisholm for providing us with continued encouragement at every step of the way.

Professor Linda Cooper for providing us with guidance and tools for effective science writing.

Dr. Frédéric Guichard of the Department of Biology and Dr. John Stix, Chair of Earth and Planetary Sciences, for their enthusiasm and support for this initiative.

We wish to thank the professors and post-doctoral fellows who graciously offered their time to review students' article submissions.

We would like to acknowledge the tireless efforts of the MSURJ board of editors in assembling this edition of the journal. Lastly, we wish to recognize the student contributors whose commendable efforts have made this journal possible.

Genomic and phenotypic variability of *Mycobacterium avium* subspecies

Ehsan Dadvar*¹

¹Department of Microbiology and Immunology, McGill University, Duff Medical Building, 3775 University Street, Montreal, Quebec, Canada, H3A 2B4

ABSTRACT

Introduction: *Mycobacterium avium* complex consists of *M. intracellulare* and the subspecies of *M. avium* subsp. *avium*, *M. avium* subsp. *paratuberculosis* and *M. avium* subsp. *hominissuis*. Despite their taxonomic relationship, these subspecies are organisms with distinct phenotypes, ranging from environmental bacteria that cause infections in immuno-compromised hosts to pathogens targeting birds and ruminants. The reasons for the variable pathogenicity and host range of *M. avium* subspecies are not known. We hypothesize that genotypic differences between *M. avium* subsp. *avium* and *M. avium* subsp. *paratuberculosis* can explain different pathogenic outcomes. **Methods:** We used tri-genomic comparisons to look for DNA fragments unique to each subspecies. We also used an acute model of mouse infection to determine different phenotypic outcomes in response to infection with different *Mycobacterium* subspecies. **Results:** Through tri-genomic comparisons we identified genetic regions of interest that may contain genes to explain phenotypic or pathogenic differences among subspecies. In an 8 week course infection, mice infected with *M. avium* subspecies *avium* had the highest bacterial burden in their spleens and livers. At the same time, mice infected with *M. avium* subspecies *paratuberculosis* had the lowest bacterial burden. **Discussion:** Differences in the genomic sequences of the *M. avium* subspecies suggests that these sequences encode pathogenic factors. Consequently, this study shows that the sequencing of *M. avium* subspecies genomes can be useful for predicting and explaining variation in pathogenesis.

KEYWORDS

Mycobacterium avium, Tri-genomic comparison, Shotgun sequencing

*Corresponding author:

ehsan.dadvar@mail.mcgill.ca

Received: 3 June 2009

Revised: 16 March 2010

INTRODUCTION

The genus *Mycobacterium* has over 130 well-characterized species. The most characteristic feature of these species is their thick, hydrophobic cell wall containing mycolic acid, which makes them very resilient and naturally resistant to many antibiotics. It is also responsible for the acid-fast staining property most commonly used to identify the mycobacterium. Most *Mycobacterium* species are strictly saprophytic and not known to cause disease in humans or animals; however, some species are pathogens. Among the pathogenic mycobacteria are *Mycobacterium tuberculosis* and *Mycobacterium leprae*, etiologic agents of tuberculosis (TB) and leprosy respectively. Whilst there has been a decline in the total number of leprosy cases, TB remains a threat to public health on a global scale. Despite an attenuated vaccine having been available for more than 50 years, approximately 2 million people

die from *M. tuberculosis* infections every year and one-third of the world's population is latently infected with *M. tuberculosis* (1).

After *M. tuberculosis*, the most commonly isolated mycobacterial pathogens in clinical laboratories are organisms of the *M. avium* complex (MAC). MAC consists of *M. intracellulare* and the subspecies *M. avium* subspecies *avium* (MAA), *M. avium* subspecies *paratuberculosis* (MAP) and *M. avium* subspecies *hominissuis* (MAH) (2,3). Together these organisms account for over 70 percent of non-tuberculosis mycobacterial disease in the United States (4,5) and for more than 95 percent of non-tuberculosis mycobacterial disease among persons with HIV/AIDS (6).

M. avium appears to comprise two broad ecotypes of organisms: host-associated bacteria and environmental organisms. Host-associated subspecies include MAA and MAP. MAA is a poultry pathogen causing pulmonary TB in birds. MAP is an obligate pathogen of ruminants causing Johne's disease, which is characterized by chronic enteritis. Johne's disease is a significant economic problem in the cattle industry. A United States Department of Agriculture report from April 2008 suggests that as many as 70% of US dairy herds are infected. Although the condition is easy to identify once symptoms arise (diarrhoea, weight loss and decreased milk production), it is challenging to diagnose in the early, asymptomatic stages of infection. Healthy, but infected, animals transmit the organism through milk and feces, invisibly spreading the infection to younger animals. Recent studies have shown that MAP can survive pasteurization and has been identified in off-the-shelf milk from retail grocery stores in the US and the European Union (7). Recent reports also implicated MAP in cases of Crohn's disease in humans, a condition characterized by intestinal pathology that is reminiscent of Johne's disease in cattle (8,9). People with Crohn's disease have been shown to be seven times more likely to have MAP infection than those who do not have Crohn's disease (8). These observations have led to the hypothesis that MAP causes Crohn's disease in susceptible hosts. To date, despite all of the efforts to address the role of MAP in this context, the hypothesis that MAP is the cause of Crohn's disease remains neither proven nor refuted (10).

MAH is the environmental strain of *M. avium*. MAH is ubiquitous in the environment and can be isolated from fresh and saltwater, municipal water systems, pools, house dust and soil (11,12). MAH is also known to cause opportunistic infections in humans, including lymphadenitis in children, disseminated *M. avium* disease in immuno-compromised patients and pulmonary disease in immuno-competent adults (13,14). The most important risk factor for pulmonary *M. avium* infection in patients without HIV infection is underlying lung disease such as cystic fibrosis or chronic obstructive lung disease (11). MAH is the most commonly isolated clone of *M. avium* from humans (3); this

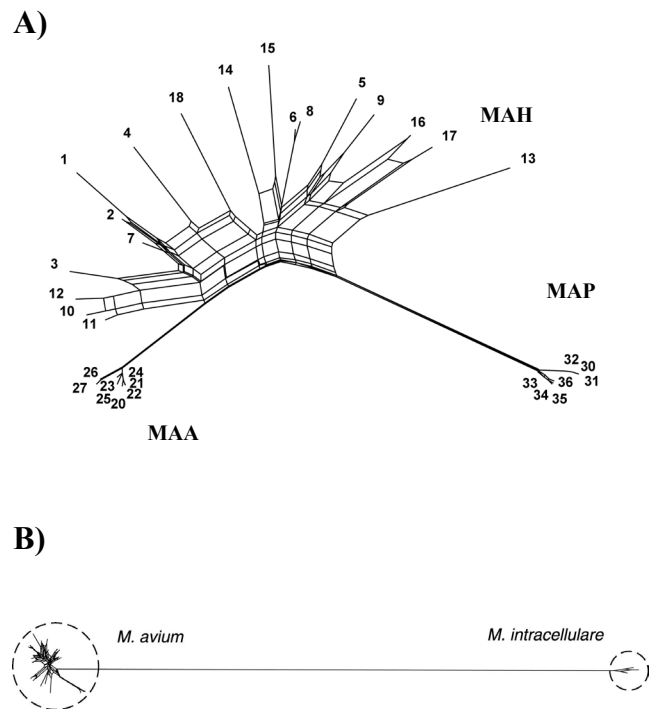


Fig. 1. Phylogenetic Representation of *M. avium*. (A) Unrooted Phylogenetic representation of *M. avium* subspecies based on 10 genes generated in SplitsTree4. The host-associated pathogen lineages are present as two independent branches that extend outward from the complex web containing exclusively strains of MAH. (B) Phylogenetic analysis of *M. avium*, based on six genes, using *M. intracellulare* as an out-group. As one can see, *M. intracellulare* remains quite distant from *M. avium*. (This Fig. was taken from "Mycobacterium avium subsp. paratuberculosis and *M. avium* subsp. avium are independently evolved pathogenic clones of a much broader group of *M. avium* organisms" by Turenne *et al.*)

may be due to the fact that MAH is ubiquitous in the environment and we are exposed to it more readily than host-associated subspecies that are not commonly found in the environment.

Multilocus sequence analysis, performed on 56 strains of *M. avium* and based on 10 housekeeping genes shared among all the subspecies of *M. avium*, confirms the classification scheme presented (Fig. 1) (2). As seen in Figure 1A, the two independent branches extending outward from the complex web consist exclusively of environmental strains, meaning that there is relatively small variation among host-associated pathogens. A follow-up study recently published by Alexander *et al.* demonstrated that MAP has evolved independently in a bi-phasic process from MAH, characterized by insertion of novel DNA followed by deletion events leading to genomic down-sizing (15). Whether this is the case for MAA remains to be seen. Despite this genetic model,

the reasons for the variable pathogenicity and host range of *M. avium* subspecies are not known. As a result, we decided to conduct a series of experiments to further characterize *M. avium*.

Our hypothesis is that phenotypic differences between subspecies of *M. avium* are encoded in their genomes, such that comparative genomic analysis can help explain the variance among these closely-related organisms. In recent years, genome projects have been completed for two of the three major subspecies of *M. avium*: MAP K-10 (type strain of MAP) and *M. avium* 104 (type strain of MAH). The K-10 genome is 4.83 Mb long, and contains 4,350 open reading frames. *M. avium* 104 has an additional 700 kb of DNA, for a total genome size of 5.48 Mb. Both genomes have a G+C content of approximately 69% and comparison of orthologous genes reveals 99% sequence identity. Because there are three major subspecies of this organism, bi-genomic comparisons between these two strains provide an incomplete portrait of the genomic diversity of these subspecies. As a result, we decided to sequence the type strain of the remaining subspecies, *M. avium* subspecies avium ATCC 25291 as a first step towards a set of genomic studies.

The genome project for MAA ATCC25291 is in its final stage. A shotgun library has been generated and 40% of the gaps in it have been closed. Through tri-genomic comparisons, we observed genomic variation compatible with the bi-phasic model of evolution. We showed that whereas host-associated pathogens had smaller genomes than environmental strains, they possess approximately 200 kb of extra DNA unique to each pathogen.

We also examined the phenotype of *M. avium* subspecies by injecting a representative of each subspecies intraperitoneally in a neutral, non-natural host: the C57BL/6 mouse. In a neutral host, neither subspecies has a replication advantage, which allows a comparison of pathogenicity. The murine model is a well-characterized model for mycobacterial infection, and has been used to study *M. tuberculosis* for many years. Mycobacterial burden in the livers and spleens of infected mice were examined one, four and eight weeks post-infection. We showed that although *M. avium* subspecies behave differently in the host, they do not have a common pathogenic profile. This is the first study comparing the relative virulence of all three subspecies.

MATERIALS AND METHODS

GENOME SEQUENCING

Whole-genome shotgun sequencing is currently the most widely used approach for whole genome sequencing. This approach has been used successfully to completely sequence both microbial

and mammalian genomes. We employed shotgun sequencing to determine the complete genome sequence of *M. avium* subsp. avium ATCC 25291. In the shotgun sequencing method, all the DNA of the organism of choice is isolated, randomly fragmented, size selected and cloned to produce a random library in *E. coli*. The clones are then sequenced using the chain termination method. By following this procedure for several copies of the same long DNA strand, overlapping fragments are created. Finally, computer programs align these overlapping sequences and determine the original sequence. Once a sufficient number of sequences are generated, the sequences are assembled into continuous DNA assemblies of the consensus sequence from the shorter individual clone sequences. In practice, gaps in the genome are likely to occur due to repeat areas and unclonable regions in the genome. The last step in the shotgun sequencing method is to close the gaps.

SUBSPECIES	STRAIN NAME	INOCULUM DOSE
<i>M. AVIUM</i> SUBSPECIES <i>HOMINISSUIS</i>	<i>M. AVIUM</i> 104	4 X 10 ⁷ CFU
<i>M. AVIUM</i> SUBSPECIES <i>AVIUM</i>	ATCC 25291	10 ⁷ CFU
<i>M. AVIUM</i> SUBSPECIES <i>PARATUBERCULOSIS</i>	K10	4 X 10 ⁶ CFU

Table 1. Strain name and inoculum dose of *M. avium* subspecies injected intraperitoneally into C57BL/6 mice.

Our collaborators at the University of Minnesota generated the shotgun library and we took the responsibility of closing the gaps. The gaps of the MAA genome were bridged by generating polymerase chain reaction (PCR) products across the gaps. Using *M. avium* MAP-K10 and *M. avium* 104 genomes, we assembled the DNA fragments and identified the gaps, after which we linked the gaps by PCR. The PCR products were sequenced by Genome Quebec. The sequences were then inserted into the genome, linking the DNA fragments.

DNA EXTRACTION AND PCR CONDITIONS

Bacterial DNA (*M. avium* subsp. avium ATCC 25291) was extracted using ribolyzer protocol. Primers were designed in Primer3 (<http://primer3.sourceforge.net/>). All PCRs were performed in a final reaction volume of 50 µl and contained 100 ng of DNA template, 2.5 mM MgCl₂, 1× Taq buffer with (NH₄)₂SO₄ (Fermentas), 5 µl of 50% acetamide (Sigma), 0.2 mM dNTPs, 0.5 µM of each primer and 1.5 U of Taq DNA polymerase (Fermentas). PCR was performed using an Applied Biosystems Gene Amp 2700 PCR System under the following conditions: 94 °C for 3 min; 30–35 cycles of 94 °C (30 sec), 55 °C (30 sec) and 72 °C (1.5 min); 72 °C for 5 min, then held at 4 °C. A higher annealing temperature was necessary with some PCRs to minimize non-specific amplification. We verified the amplification of PCR

products through electrophoresis with 1.5% agarose gels. In cases where PCR product was not obtained, we increased the MgCl₂ concentration to 3.5 mM. As a positive control, we also amplified the *hsp65* gene (~1.5 kb) with every PCR reaction.

MICE AND BACTERIAL CULTURE

We used germ-free, 8-10 week old male C57BL/6 mice which were purchased from Harlan Laboratories and maintained in the McGill University Health Centre animal facility. Bacterial strains used in our experiments included *M. avium* MAP K-10, *M. avium* 104 and *M. avium* ATCC 15291. The strains were all grown in Middlebrook 7H9 medium containing ADC supplement (Difco Laboratories, Detroit, MI) plus 0.04% of Tween 80 (Sigma, St Louis, MO) and Mycobactin J (Allied Monitor) at 37 °C.

INTRAPERITONEAL MURINE MODEL OF INFECTION

Because these organisms have different natural hosts, we chose a neutral, non-natural host: the C57BL/6 mouse. We challenged 20 C57BL/6 mice intraperitoneally with ~107 CFU of each *M. avium* subspecies (Table 1). The livers and spleens from the infected mice were collected at one, four and eight weeks post-infection. We sacrificed six animals per group per time-point, then homogenized, serially diluted and plated the tissue in Middlebrook 7H10 medium with OADC supplement (Difco) plus Mycobactin J (Allied Monitor) and PANTA (Becton Dickinson Diagnostic Instrument Systems, Sparks, Md.), which is a mixture of antibiotics intended to suppress the growth of contaminating organisms. The cultures were incubated at 37 °C and the colony forming units (CFU) were quantified after three weeks in the case of MAH and MAA, and 8 weeks in the case of MAP. Only plates containing 25 to 250 CFU were considered.

RESULTS

M. AVIUM SUBSPECIES ARE GENOTYPICALLY DIFFERENT

To determine the genomic variability of *M. avium* subspecies, we decided to do a tri-genomic comparison. Since full genome sequences for only two of *M. avium* subspecies are available, we, along with collaborators at the University of Minnesota, decided to sequence the genome of the remaining subspecies. Our colleagues in Minnesota generated the shotgun library and we took the responsibility of closing the gaps, as described below.

CLOSING THE GAPS IN MAA GENOME.

Initially, there were 401 gaps in the MAA ATCC 25291 genome. We bridged 160 gaps through PCR. There was a tremendous amount of variation in the gap sizes. The largest gap closed was ~1500 base pairs and the smallest gap was 0, which means there

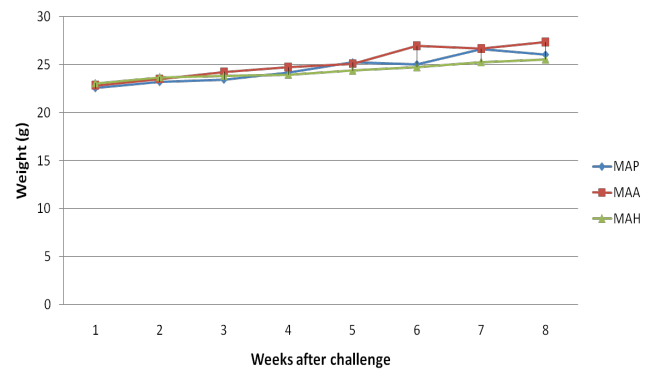


Fig. 2. Weight of Infected Mice over Time. Weight change in response to infection with different subspecies of *M. avium*. The mice in all groups gained weight and did not show any clinical sign of illness.

was no gap separating the adjacent contigs, which are sets of overlapping DNA segments from a single genetic source. The average gap length, however, was 153 base pairs. Since there were 401 gaps and 160 of them were closed, the efficiency of PCR in bridging the gaps was 40%. The sequences I bridged have been deposited in GenBank database on 22-Jan-2009. This project is ongoing. Given the average gap length is 150 base pairs, we estimate the full genome sequence of MAA contains approximately 4.9 Mb.

PRELIMINARY TRI-GENOMIC COMPARISON: GENOMIC VARIABILITY IN DIFFERENT *M. AVIUM* CLONES IS RELATIVELY GREAT.

To determine the degree of genomic variability of *M. avium* subspecies, we compared the three genomes. Early work based on the comparison of the two completely sequenced genomes of *M. avium* MAP-K10 and *M. avium* 104 and the incomplete sequenced genome of MAA ATCC 25291 revealed that these organisms share a core set of approximately 4000 genes with 99% identity at the DNA sequence level. However, there is also significant variability between them, as revealed by the presence of ~850 kb of DNA unique to *M. avium* 104, ~260 kb of DNA unique to *M. avium* MAP K-10 and ~200 kb of DNA unique to MAA ATCC 25291.

M. AVIUM SUBSPECIES ARE PHENOTYPICALLY DIFFERENT

To determine the relative virulence of the three sequenced strains of *M. avium*, we injected groups of C57BL/6 mice intraperitoneally with ~107 CFU of each *M. avium* subspecies. To ensure that we injected the right dose into each group, extra stocks were made, serially diluted and plated. The results can be seen in Table 1. As one can observe, there was some variation in the bacterial inocula. The initial differences were taken into account when we compared the bacterial burden at different time points by normalizing the CFU values.

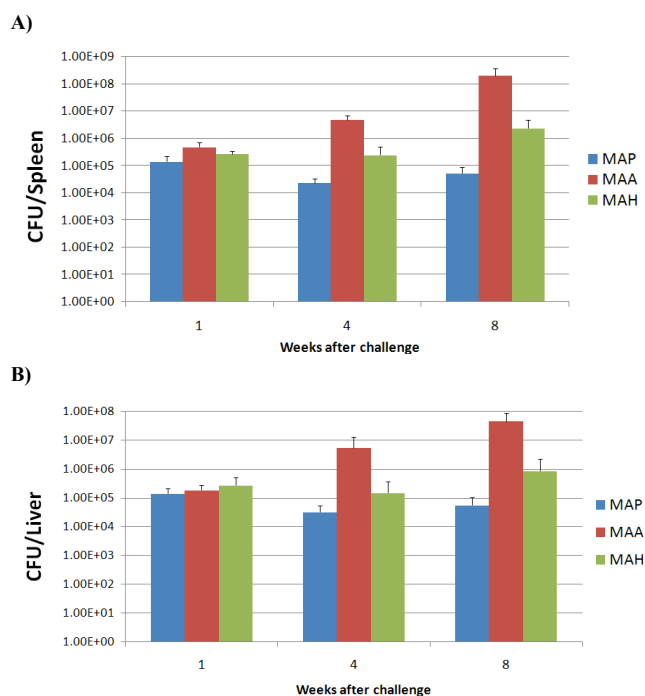


Fig. 3. Bacterial Burden in the Spleen and Liver of Infected Mice. Bacterial burden in the spleen (A) and liver (B) of mice infected with MAP, MAA and MAH. Bacterial burden is approximately the same for all groups at week 1 before diverging in subsequent weeks. MAP results are normalized to make up for its lower inoculum dose.

PHYSIOLOGIC RESPONSES TO *M. AVIUM* INFECTION: MICE INFECTED WITH DIFFERENT SUBSPECIES OF *M. AVIUM* DID NOT SHOW ANY CLINICAL SIGN OF ILLNESS OR GROWTH RETARDATION.

We monitored the animals' weights weekly as a marker of pathology since weight-loss or growth retardation is a global indicator of illness. Weight change over time in response to infection with different *M. avium* subspecies is shown in Fig. 2. The mice from all groups gained weight and did not show any clinical signs of illness. Mice infected with MAH gained 2.5 g, the ones infected with MAA gained 4.5 g and finally mice infected with MAP gained 3.5 g. Paradoxically, the mice infected with host-associated strains (MAA and MAP) appeared to gain more weight than the mice infected with the environmental strain (MAH). From previous experiments we know that C57BL/6 mice infected with PBS gain about 2.5 g over 8 weeks.

SUBSPECIES OF *M. AVIUM* HAVE DIFFERENT PATHOGENIC PROFILE IN ACUTE MODEL OF INFECTION.

To determine the relative virulence of *M. avium* subspecies, we quantified the bacterial burden from spleens and livers of infected mice at different time points. We expected that the mice infected with the most virulent subspecies would have the high-

est bacterial burden measured by the number of CFU. Given that MAA and MAP are obligate pathogens and MAH is an environmental strain, we expected that the mice infected with MAH would have the lowest bacterial burden compared to the pathogenic clones. The results are shown in Fig. 3.

We observed similar trends in both the spleens (Fig. 3A) and livers (Fig. 3B). At week 1, spleen and liver bacterial burden were approximately the same for all groups. However, by week 4, CFU values started to diverge. Over 8 weeks, the bacterial burden in the spleen and liver of mice infected with MAH was relatively stable. There was a drastic increase in the spleen and liver bacterial burden of the group infected with MAA, from ~105 CFU at week 1 to ~108 CFU at week 8. Unexpectedly, the bacterial burden of the group infected with MAP decreased over time even though MAP is considered one of the pathogenic strains of *M. avium*.

Looking at the CFU values, it was not possible to distinguish host-associated subspecies from the environmental strain. MAA, a causative agent of avian-TB, showed excellent proliferative capacity inside the host. MAP, a causative agent of Johne's disease in cattle, showed a poor proliferative capacity. The environmental strain was somewhere in between. Our results show that different pathogenic subspecies apparently behave quite differently in a standardized model of in vivo bacterial replication.

DISCUSSION

M. avium consists of a genetically related yet diverse group of bacteria in terms of environmental niches, host types and disease phenotypes. The basis of this variation is unknown. In order to explain this variability, we decided to compare the genomes of the three major subsets of *M. avium*. Since there are three major *M. avium* subsets and the genome projects for only two of the subsets are available, our first step was to initiate the genome project for the representative of the third subset, MAA ATCC 25291. Through collaboration with the University of Minnesota, we generated a shotgun library and bridged 40% of the gaps in the library. Tri-genomic comparisons revealed that although all the subspecies share about 4000 genes and are classified as single species, the genetic variability is significant. The host-restricted subsets, MAA and MAP, have smaller genomes and each contain approximately 200 kb DNA unique to them. Given that MAP and MAA are pathogens and MAH is an environmental strain, the genes present in the extra fragments of DNA are excellent virulence factor candidates that may account for the phenotypic heterogeneity of *M. avium* strains.

We also examined the virulence of *M. avium* subspecies in C57BL/6 mice. It was expected that the pathogenic clones would distinguish themselves from the environmental strain by a

common pathogenic profile. Unexpectedly, in an acute model of murine infection, it was not possible to distinguish pathogenic subspecies of *M. avium* based on weight of infected mice or bacterial burden.

The infected mice from all groups gained weight and did not show any signs of illness. If the mice were infected with *M. tuberculosis*, which is a known mycobacterial pathogen, growth retardation would be expected at the bacterial burdens we observed. Therefore, we can conclude that *M. avium* subspecies are not very virulent. It is worth noting that in the case of MAA, the bacterial burden was very high (~108 CFU in spleen at week 8) and the animals still did not show any sign of illness or weight loss. In *M. tuberculosis* infections, bacterial burdens never rose above 106 CFU in the spleen, as by that time all the mice had died. This shows that although MAA proliferates rapidly inside the host, it is not particularly virulent.

Although no one has ever compared all three subspecies of *M. avium* in vivo, it has been shown that MAA replicates better inside the host and hence is more virulent than MAH. In the present study, MAA was shown to replicate more rapidly in vivo, whereas MAH was shown to replicate more slowly (Fig. 3). This result is consistent with the findings reported by Young et al. that MAA is more virulent than MAH (16). In vitro studies comparing MAA and MAH have shown that MAH replicates more rapidly within murine macrophages and, unlike MAA, induces a strong inflammatory cytokine production, particularly tumor necrosis factor-alpha (16,17). It has been hypothesized that the rapid proliferation of MAA in vivo may result from its ability to suppress host responses, including inflammatory cytokines. In contrast, the induction of inflammatory cytokines by MAH may result in a more effective host control of infection. However, these in vitro observations need to be confirmed in vivo to determine whether strong cytokine production in vivo correlates with a decreased capacity to replicate inside the host. Future experiments to test this hypothesis would consist of immunological assessment one week after infection, when the bacterial burden is the same for all subspecies. This experiment would help clarify whether MAA replicates better in the host due to its ability to subvert host immune responses.

In contrast to MAA, MAP burden in the spleen and liver decreased over 8 weeks (Fig. 3). Unpublished data from our lab shows that following intravenous injection of 106 CFU of MAP into C57BL/6 mice, there is a persistent infection for up to 6 months. After combining the results, it appears that MAP is more of a stealth pathogen that replicates very slowly inside its host and, as a result, is able to persist for a long time. We believe that this is why MAP has infected 70% of dairy herds.

Our results in the present study show that the acute model of murine infection holds promise to study MAA virulence factors, but is unlikely to serve as a good model to understand MAP-specific virulence. Using the acute model of murine infection, we can start to screen MAA mutants for their virulence and identify the virulence factors. We can start with open reading frames identified as potential virulence factor genes through the tri-genomic comparison.

Subspecies of *M. avium* behave differently inside the host and have different approaches to pathogenesis. MAA proliferates rapidly inside the host without generating a deleterious immune response. In contrast, MAH presented a reduced capacity to replicate inside the host, likely associated with the induction of a strong cytokine response (16,17). MAP did not proliferate as well as other subspecies in this model, but from other studies in the lab, appears to survive the longest of these three subspecies within the host. Very little is known about the biological differences between environmental, opportunistic and host-restricted pathogenic members of *M. avium*, including their virulence mechanisms.

However, we have begun to identify genetic regions of interest that may contain candidate genes that confer phenotypic or pathogenic differences among them, helping guide future functional studies. We also showed that acute models of murine infection, while not very helpful in screening MAP knock-outs, can be useful to screen MAA knock-outs for loss-of-virulence.

ACKNOWLEDGMENTS

This research was supported by the Canadian Institute of Health Research (CIHR).

REFERENCES

1. "Global tuberculosis control: a short update to the 2009 report" (World Health Organization, Geneva, Switzerland, 2009).
2. C.Y. Turenne, D.M. Collins, D.C. Alexander, M.A. Behr, *J. Bacteriol.* **190**, 2479-2487 (2008).
3. C.Y. Turenne, R. Wallace Jr., M.A. Behr, *Clin. Microbiol. Rev.* **20**, 205-229 (2007).
4. C.R. Horsburgh Jr., *N. Engl. J. Med.* **324**, 1332-1338 (1991).
5. R.J. O'Brien, L.J. Geiter, D.E. Snider Jr., *Am. Rev. Respir. Dis.* **135**, 1007-1014 (1987).
6. C. Reed et al. *Am. J. Epidemiol.* **164**, 32-40 (2006).
7. J.L. Ellingson et al. *J. Food Prot.* **68**, 966-972 (2005).
8. M. Feller et al. *Lancet Infect. Dis.* **7**, 607-613 (2007).

9. S.A. Naser, G. Ghobrial, C. Romero, J.F. Valentine, *Lancet*. **364**, 1039-1044 (2004).
10. M.A. Behr, V. Kapur, *Curr. Opin. Gastroenterol.* **24**, 17-21 (2008).
11. C.B. Inderlied, C.A. Kemper, L.E. Bermudez, *Clin. Microbiol. Rev.* **6**, 266-310 (1993).
12. M.A. Telles *et al.* *Epidemiol. Infect.* **122**, 435-440 (1999).
13. L.E. Bruijnesteijn van Coppenraet, P.E. de Haas, J.A. Lindeboom, E.J. Kuijper, D. van Soolingen, *Eur. J. Clin. Microbiol. Infect. Dis.* **27**, 293-299 (2008).
14. J.O. Falkinham III, *Emerg. Infect. Dis.* **9**, 763-767 (2003).
15. D.C. Alexander, C.Y. Turenne, M.A. Behr, *J. Bacteriol.* **193**, 1018-1025 (2007).
16. S.L. Young *et al.* *Infect. Immun.* **75**, 2833-2840 (2007).
17. V. Falcone, E.B. Bassey, A. Toniolo, P.G. Conaldi, F.M. Collins, *FEMS Immunol. Med. Microbiol.* **8**, 225-232 (1994).

ERK-CREB signaling dysregulation with increasing levels of the β -Amyloid protein

Amanda Grant-Orser*¹, Fabio Canneva²

¹Department of Anatomy and Cell Biology, McGill University, 3640 University Street, Montréal Québec, H3A 2B2

²Department of Pharmacology and Therapeutics, McGill University, McIntyre Medical Building, 3655 Promenade Sir William Osler, Montreal, Quebec, Canada, H3G 1Y6

ABSTRACT

Introduction: Alzheimer's Disease is characterized by cognitive impairment and neurodegeneration, for which the pathogenic cause is considered to be the accumulation of the β -amyloid peptide ($A\beta_{42}$). The Swedish and Indiana mutations of the amyloid precursor protein gene ($APP_{Swe,Ind}$), found in the genetic familial form of AD, increase $A\beta_{42}$ levels due to augmented enzymatic cleavage. Previous experiments demonstrate that high levels of soluble $A\beta_{42}$ upregulate extracellular regulated kinase 1/2 (ERK1/2) and downregulate cyclic AMP-response element (CRE) binding protein (CREB) phosphorylation. Increasing levels of soluble $A\beta_{42}$ protein are hypothesized to dysregulate the ERK-CREB signalling pathway. **Methods:** Three plasmid constructs containing wild type amyloid precursor protein (APP_{Wt}), APP_{Swe} or $APP_{Swe,Ind}$, each producing increasing levels of $A\beta_{42}$, were stably transfected into eukaryotic cell lines. Immunocytochemistry was performed using the McSA1 antibody to measure the amount of $A\beta$ protein in the $APP_{Swe,Ind}$ and APP_{Wt} cell lines. Cells were stimulated with forskolin and KCl. ERK and CREB phosphorylation were analyzed by western blot. **Results:** McSA1 staining demonstrated increased $A\beta$ protein in the $APP_{Swe,Ind}$ cell line compared to the APP_{Wt} cell line. Upon cell stimulation at 30 minutes, the APP_{Wt} cell line demonstrated the highest levels of CREB phosphorylation and $APP_{Swe,Ind}$ demonstrated the lowest levels. ERK phosphorylation increased upon stimulation and was sustained across all four time points, but there was no significant difference in levels between the clones. **Discussion:** These results suggest that the $A\beta$ protein has beneficial effects on CRE-regulated gene expression at physiological levels and negative consequences that mimic Alzheimer's Disease at pathogenic levels.

KEYWORDS

Amyloid precursor protein, ERK, CREB

*Corresponding author:

amanda.grant-orser@mail.mcgill.ca

Received: 3 January 2010

Revised: 18 March 2010

INTRODUCTION

Alzheimer's Disease (AD) is currently the leading cause of dementia, affecting 10% of the Canadian population over the age of 65. AD is clinically characterized by a gradual decline in cognitive abilities, and biologically by neuron death in the cortex and hippocampus (1). The pathogenic cause of Alzheimer's disease has been attributed to the β -amyloid protein which exists in two isoforms: ($A\beta_{40}$) at a length of 40 amino acids and $A\beta_{42}$ at 42 amino acids. Since $A\beta_{42}$ is more hydrophobic and prone to aggregation, it seems to be the pathogenic isoform (2). $A\beta$ is cleaved from the amyloid precursor protein (APP) by the β and γ -secretases sequentially. There also exists a separate processing pathway not

linked to AD, in which APP is cleaved by the α -secretase (3). Genetic variants of APP have been discovered in familial forms of AD (FAD), whereby mutations at the sites of secretase cleavage favour the production of $A\beta_{42}$. Other FAD-related mutations have been described for the genes encoding presenilin 1 and 2, the catalytic components of the γ -secretase, which also result in augmented $A\beta_{42}$ production (4). Harnessing these FAD mutations has led to the manipulation and study of AD in both *in vivo* and *in vitro* models to obtain a better understanding of the cellular pathology and more effective therapeutic remedies.

Early stages of AD are characterized by the accumulation of intracellular oligomeric $A\beta$ (i $A\beta$). In later stages of disease, indicators of AD pathology include a wide variety of physiological and behavioural consequences including, but not limited to, abnormal neuron projections, inflammation, neurotransmitter defects, extracellular $A\beta$ plaque deposition and intracellular neurofibrillary tangles (NFTs), which consist mainly of hyperphosphorylated microtubule-binding Tau protein (5-9). While many investigations have studied the consequences of extracellular $A\beta$ plaques, researchers have more recently focused on the significance of i $A\beta$ accumulation in the progression of behavioural impairments characteristic of the disease. Current research is also examining the roles of neuroinflammation and neurodegeneration (10). This "pre-plaque" phenotype of accumulated i $A\beta$ has been shown to have downstream effects on the phosphorylation of extracellular regulated kinase 1/2 (ERK 1/2), an intracellular kinase coupled to an extracellular activation signal, and cyclic AMP (cAMP) response element binding protein (CREB), a transcription factor which binds cAMP response elements on DNA to regulate transcription (11). ERK is an activation kinase of another kinase called p90RSK, which phosphorylates CREB. Upon phosphorylation, CREB acts as a transcription factor for the cAMP response element (CRE)-regulated genes. CRE-regulated genes are implicated in learning and memory, namely in the development of long term potentiation (LTP) at synapses (12-13), a process involved in synaptic strength increase and which is greatly disrupted in AD.

Previous *in vivo* studies suggest that when the $A\beta$ protein is over-produced, CRE-regulated gene expression is downregulated (11). The effect of $A\beta$ levels on CRE-regulated gene activation has also been demonstrated *in vitro* using transiently transfected cells in the lab (14), whereby nucleic acids were introduced into the cell by non-viral methods and transiently expressed. The use of stably transfected cell lines where there is genomic integration of the introduced nucleic acids, however, would allow for a more precise assay of ERK-CREB signalling regulation and better reproducibility of previous experiments. Our hypothesis is that with increasing levels of soluble $A\beta_{42}$ protein, ERK/CREB phosphorylation and CRE-directed gene expression will be dys-

regulated. This dysregulation is expected to correspond to the amount of $A\beta_{42}$ produced. To test this idea, three plasmid constructs for the expression of wild type APP (APP_{Wt}), APP_{Swe} and $APP_{Swe,Ind}$ variants, each leading to increased levels of the $A\beta$ protein, respectively, were stably transfected into eukaryotic cell lines. The consequent dysregulation of ERK-CREB signalling was evaluated by measuring ERK and CREB phosphorylation before and after chemical stimulation of the cells.

METHODS

The DNA constructs were all derived from the pIRES vector backbone in which the transgenic protein (APP variants) is expressed under the control of the human cytomegalovirus (CMV) promoter and co-translated with the enhanced green fluorescent protein (EGFP). Three transgenic proteins were used: APP_{Wt} , APP_{Swe} and $APP_{Swe,Ind}$. Stable transfections were done on PC12 cells using G418, a neomycin analog, 48 hours after transfection for selection. Cells were selected into homogenous populations of APP expression using fluorescence activated cell sorting (FACS). Immunocytochemistry was used to detect the presence of $A\beta$ protein using the MCSA1 antibody. To test the ERK-CREB signalling pathway, cells were stimulated with KCl and forskolin at varying time points and analysed via western blot. Results were analyzed by one-way (FACS cell sorting) or two-way (cell stimulation) ANOVA tests. Differences were considered statistically significant at $p < 0.05$ (*). ($p < 0.001$ is indicated by ***). In a separate cell stimulation experiment with time points of 30 minutes, 1 hour, 2 hours and 3 hours, results were analyzed qualitatively, since $N = 1$.

RESULTS

TRANSFECTIONS

PC12 cells were successfully and stably transfected with the four clones; pIRES (control), APP_{Wt} , APP_{Swe} and $APP_{Swe,Ind}$. All subsequent results shown are from the PC12 transfected cell lines.

POPULATION STANDARDIZATION BY FACS

Levels of transgene expression can vary with the amount of plasmid integrated into the cell genome. To ensure that the cell lines being tested expressed APP homogeneously and were comparable, EGFP was used as a second selectable marker for protein expression. FACS selected cells based on their emitted green fluorescence. Sorting resulted in a standardized population of cells with an average of over 75% EGFP positive in all cell lines (Fig. 1). The APP_{Swe} clone is shown before and after the sorting process (Fig. 2) as a qualitative example of the homogenized population of increased EGFP expression.

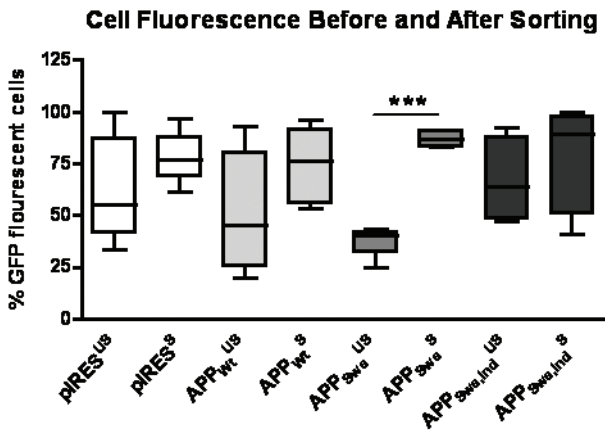


Fig. 1 Cell Fluorescence Before and After Sorting
 Comparison of GFP% positive unsorted (US) and sorted (S) cells. Only the APP_{Swe} clone had a statistically significant increase in green fluorescence ($p < 0.001$).

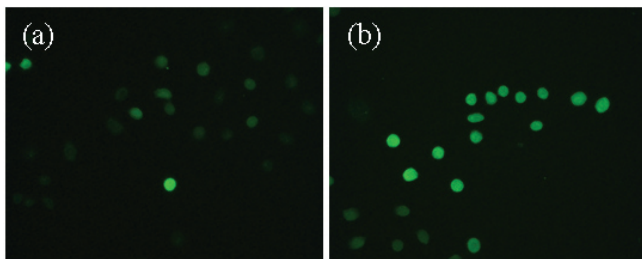


Fig. 2 APP_{Swe} clone FACS selection (A) before selection (B) after selection

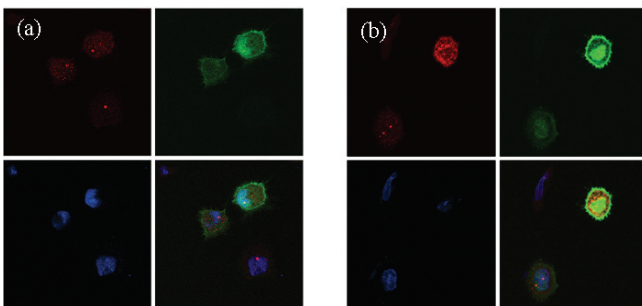


Fig. 3 ICC Confocal microscopy
 Evidence for the differential expression of the A β protein between the (a) APP_{wt} and (b) APP_{Swe,Ind} clones.

QUALITATIVE A β EXPRESSION

Immunocytochemistry (ICC) was used to qualitatively analyze A β protein expression between the different clones. Cells were examined at 63x magnification on a confocal microscope, with Blue DAPI staining identifying cell nuclei. The primary antibody used was McSA1, which is specific for the human A β protein, and the secondary antibody used was Rhodamine flourophore. The negative control (no primary antibody applied) showed minimal rhodamine fluorescence, demonstrating the specificity of the secondary antibody for McSA1 (results not shown). The APP_{wt} clone had more intense McSA1 staining than the background pIRES (control) as well as a unique peripheral pattern. McSA1 staining correlated with the intensity of EGFP fluorescence, indicating that green fluorescence correlated with transgene protein expression. Comparison of the APP_{wt} and APP_{Swe,Ind} clones (Fig. 3) demonstrated that levels of A β protein production were much greater in the APP_{Swe,Ind} clone than in the wild-type, as evidenced by increased McSA1 staining. The peripheral staining pattern in the APP clones suggests A β could be contained in peripheral vesicles.

CREB PHOSPHORYLATION BEFORE AND AFTER STIMULATION

UNSTIMULATED (NI), 5 MINUTES, 15 MINUTES, 30 MINUTES

Western blot analysis was used to determine levels of phosphorylated CREB (pCREB) in PC12 cells transfected with APP_{wt}, APP_{Swe} and APP_{Swe,Ind} clones. There was no statistically significant difference (2-way ANOVA) of pCREB levels between the clones in unstimulated cells (Fig. 4). Cells were stimulated with Forskolin and KCl. Stimulation for 5 minutes demonstrated that the presence of moderate A β levels, produced by the APP_{Swe} clone, increased the cell's responsiveness to CREB phosphorylation ($p < 0.05$). After 15 minutes, high levels of A β produced by the APP_{Swe,Ind} clone appear to inhibit the phospho-

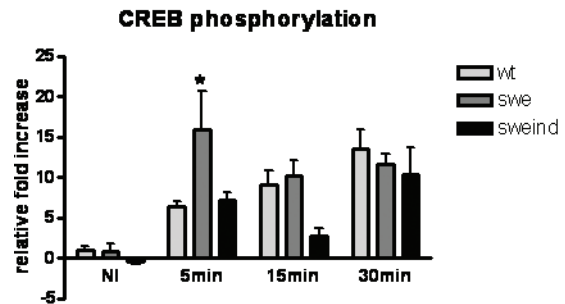


Fig. 4 CREB phosphorylation levels normalized against β -tubulin before and after stimulation

At 5 min. the rise A β levels caused a statistically significant increase in cell's responsiveness ($p < 0.05$). At 30 min. intermediate levels of A β caused a progressive decrease in CREB phosphorylation levels, although results were statistically nonsignificant (NS).

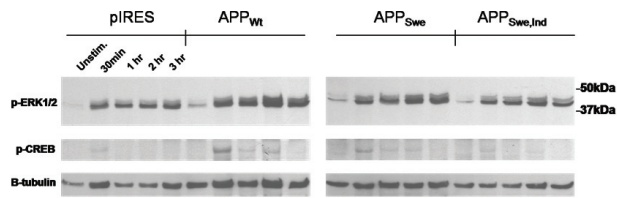


Fig. 5 Stimulation of transfected PC12 cells
pERK activation is increased upon stimulation and was sustained across all time points. pCREB increased upon stimulation and had the greatest increase in the APP_{Wt} clone. Among the APP clones, Wt had the greatest and Swe,Ind the lowest level of pCREB activity.

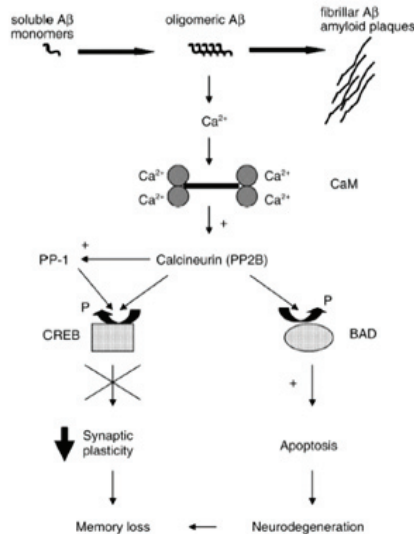


Fig. 6 PP2B signaling pathway proposed by Taglilatela et al.
Decreased CREB phosphorylation and activation of the BAD pro-apoptotic protein BAD result in the presence of high levels of oligomeric A β

rylation of CREB, though this result did not reach statistical significance. At 30 minutes, increasing levels of the A β protein (APP_{Wt} < APP_{Swe} < APP_{Swe,Ind}) caused a progressive decrease in CREB phosphorylation.

UNSTIMULATED, 30 MINUTES, 1 HOUR, 2 HOURS,
3 HOURS STIMULATION

A second western blot analysis was used to determine CREB phosphorylation levels (Fig. 5), with pIRES CREB phosphorylation used as a control. Upon stimulation, CREB phosphorylation was greatest at 30 minutes for all clones; the largest increase in pCREB was evident in the APP_{Wt} clone, followed by the APP_{Swe} clone and finally the lowest increase was in the APP_{Swe,Ind} clone. At all other time points, however, there was no significant difference in pCREB levels between the clones.

ERK PHOSPHORYLATION BEFORE AND AFTER STIMULATION

UNSTIMULATED, 30 MINUTES, 1 HOUR, 2 HOURS,
3 HOURS STIMULATION

Upon stimulation, pERK levels were increased in all clones (Fig. 5), and phosphorylative activation was sustained for all four time points. The difference in pERK levels between the clones was not significant.

TOTAL PROTEIN EXPRESSION

Total protein expression in the transfected PC12 cells was determined by β -tubulin levels. Western blot results showed an irregularity in the amount of protein loading between the samples (Fig. 5). All western blot statistical analyses of pCREB and pERK were normalized to these levels.

DISCUSSION

The goal of studying the consequences of low pathogenic levels of the A β protein is to enable intervention in the early stages of AD while intracellular A β is present, prior to plaque formation. The hope is to cure behavioural abnormalities and reverse the decline of cognitive function. The motivation prompting the use of the three different stably transfected genes was to correlate increasing levels of the A β protein to the amount of dysregulation in ERK-CREB signalling and the subsequent effects on CRE-regulated gene expression.

The three stably transfected cell lines used in this study expressed homogenous levels of APP protein. Constant expression was achieved by three methods: first, the same promoter was used for all three plasmid constructs; second, a selectable marker of transgene expression, EGFP, was co-translated with the inserted gene; third, the cells were selected using FACS. Stimulation of the cells by intracellular Ca²⁺ and cAMP production activated ERK-CREB signalling. The level of pathway activation was influenced by the amount of A β protein present, which increased across the APP_{Wt}, APP_{Swe} and APP_{Swe,Ind} cell lines.

ERK phosphorylation levels increased upon stimulation and were sustained during all four time points in all four cell lines. *In vivo*, this phosphorylation is greatest in APP_{Swe,Ind} compared to wild-type animals (unpublished results) suggesting the A β protein induces constitutive signalling; however, these results were not replicated *in vitro*. Arvanitis *et al.* observed a peak CRE-regulated gene expression 30 minutes after PC12 cell stimulation in APP transfected cells (15). In the current study, the first investigative time point for ERK phosphorylation was 30 minutes. Therefore, investigating an earlier time point could yield more conclusive results since ERK phosphorylation is upstream of CRE activation.

There was a statistically significant ($p < 0.05$) increase in pCREB levels at 5 minutes, with moderate levels of the $A\beta$ protein, as expressed by the APP_{Swe} clone (Fig. 4). The intermediate time point of 15 minutes demonstrated that high levels of the $A\beta$ protein, expressed by the APP_{Swe,Ind} clone, inhibited CREB phosphorylation. At 30 minutes, CREB phosphorylation levels progressively decreased with increasing levels of $A\beta$ protein (Fig. 4). The APP clones differed in their amount of CREB phosphorylation; the wild-type clone demonstrated the largest increase, followed by the Swe clone and then the APP_{Swe,Ind} clone, (Figs. 4 and 5). These results corroborate the theory that APP has an endogenous role in the cell by favouring CRE-regulated gene expression, while the overexpression of $A\beta$ has negative consequences on CREB phosphorylation and subsequently CRE-regulated gene expression.

Taglitatela et al. (18) have suggested a possible explanation for increased ERK phosphorylation, a kinase of CREB, and decreased CREB phosphorylation in the presence of $A\beta$. Since ERK is upstream of CREB, it is theorized that there are phosphatases activated simultaneously or after ERK which could act to dephosphorylate and rescue CREB activation. One such phosphate being investigated is the Ca²⁺/calmodulin dependent phosphatase calcineurin (PP2B). Supporting this idea, calcineurin showed increased activity with the application of exogenous $A\beta$ oligomers (Fig. 6) (16), suggesting a potential explanation for the results shown here. After 15 minutes of stimulation, increased PP2B activity induced by the high level of $A\beta$ protein could have rescued CREB from activation, elucidating why pCREB levels were lowest in the APP_{Swe,Ind} clone. Accordingly, PP2B may not have been activated at 5 minutes, allowing moderate levels of the $A\beta$ protein to exert positive effects on CREB phosphorylation. The time course of PP2B activation upon stimulation and its interaction with intracellular $A\beta$ will have to be investigated to verify this hypothesis.

Another interesting feature of calcineurin which implicates the phosphatase in the pathogenesis of AD is its activation of the proapoptotic protein BAD (17). As apoptosis is a well-characterized feature of the later stages of AD, controlling the dephosphorylative abilities of PP2B through inhibition could help manage some of the negative consequences arising from the downregulation of CREB phosphorylation and CRE-regulated gene expression seen in AD.

An alternative explanation for high pERK and low pCREB levels has been suggested by Echeverria et al. (11). Depending on the duration of stimulation, ERK could have varying consequences on its downstream substrates. p90RSK, a CREB kinase and an ERK substrate, could be hypophosphorylated either due to the simultaneous stimulation of rescue phosphatases or by the duration of ERK activity disrupting its kinase activity. This would result in a decreased level of CREB phosphorylation (18)

and CRE-regulated gene expression. Further investigations are required to confirm this hypothesis.

The work described here has several limitations. First, the level of CRE-regulated gene expression was not examined and so the final product of the ERK-CREB activation observed is still under question. Secondly, a quantitative analysis of $A\beta$ by western blot detection was unsuccessful. A likely explanation for this failure could be the low loading level of the samples. Future investigations should perform an enzyme-linked-immunosorbent-assay (ELISA) which would not only determine the level of $A\beta$ protein, but would also distinguish the isoforms $A\beta_{40}$ and $A\beta_{42}$. Nonetheless, it may be assumed that the results from the ICC of the PC12 cells represent the differential intracellular accumulation of $A\beta$ between the APP_{Wt} and APP_{Swe,Ind} clones; however, APPSwe staining has yet to be completed. In the normal human neuron, the percentage of $A\beta_{40}$ to total $A\beta$ produced is 90% and $A\beta_{42}$ only 10% (19). In contrast, the APPSwe mutation causes a shift in the ratio to 20% $A\beta_{42}$, the APPInd mutation creates a 50/50 ratio $A\beta_{40}/A\beta_{42}$, and the APP_{Swe,Ind} mutation results in almost solely $A\beta_{42}$ production (20). These investigations support the presence of increasing $A\beta_{42}$ levels within the produced cell lines. Finally, the continuing study of AD requires both an animal model which mimics the phenotype as well as a replicating cellular model. The types of cells used in vitro differ in the amplitude, magnitude and importance of their respective signaling pathways (21), hence it is difficult to produce a reliable cell line. While the rat PC12 cell line is neuronal in nature, it is not human. The McSA1 antibody used in these experiments is specific to human $A\beta$. Consequently, there is limited influence in the results from endogenously produced rat $A\beta$. Due to these collective limitations, the experiments are being repeated to confirm the reliability of the observed results.

The findings from this study can lead to a variety of future research endeavours. One possible direction will be to examine CRE-regulated genes implicated in synaptic plasticity using reverse transcriptase-polymerase chain reaction to compare gene expression levels between samples. The possibility of localizing the expressed $A\beta$ protein within the cell to specific vesicles would also be of interest. Furthermore, empirical investigations to determine the form of $A\beta$ protein accumulated by the cells should also be conducted, for example, by using the oligomeric recognizing antibody Nu1. Therapeutic testing could also be done. Therapeutic testing could be done as well, for instance by using the calcineurin inhibitor FK506 to compare its effects on varying levels of endogenously produced $iA\beta$.

To conclude, the stably transfected cell lines of APP_{Wt}, APP_{Swe} and APP_{Swe,Ind} in PC12 cells demonstrate that increased levels of the $A\beta$ protein have a downregulating effect on the phospho-

rylation of the CREB protein, validating part of the hypothesis. While not replicated in these preliminary *in vitro* experiments, ERK phosphorylation is also disrupted in the presence of increased A β *in vivo*. This study, with its intended continuation, will help to further our understanding of the AD pathology and possible therapeutic remedies.

REFERENCES

1. G. L. Wenk, *J. Clin. Psychiatry* **64**, 7 (2003).
2. R. H. Takahashi et al., *J. Neurosci.* **24**, 3592 (2004).
3. H. Zheng, E. H. Koo, *Mol. Neurodegener.* **1**, 5 (2006).
4. C. Czech, G. Tremp, L. Pradier, *Prog. Neurobiol.* **60**, 363 (2000).
5. R. Terry, *Alzheimer Disease* (Lippincott Williams & Wilkins, Philadelphia, ed. 2, 1999), pp. 457.
6. D. Games et al., *Nature* **373**, 523 (1995).
7. C. Sturchler-Pierrat et al., *Proc. Natl. Acad. Sci. U. S. A.* **94**, 13287 (1997).
8. D. Moechars, K. Lorent, F. Van Leuven, *Neuroscience* **91**, 819 (1999).
9. T. P. Wong, T. Debeir, K. Duff, A. C. Cuellar, *J. Neurosci.* **19**, 2706 (1999).
10. R. B. Maccioni, L. E. Rojo, J. A. Fernandez, R. O. Kuljis, *Ann. N. Y. Acad. Sci.* **1153**, 240 (2009).
11. V. Echeverria et al., *Neuroscience* **129**, 583 (2004).
12. A. Kelly, M. A. Lynch, *Neuropharmacology* **39**, 643 (2000).
13. R. Waltereit, M. Weller, *Mol. Neurobiol.* **27**, 99 (2003).
14. V. Echeverria, A. Ducatenzeiler, C. H. Chen, A. C. Cuellar, *Neuroscience* **135**, 1193 (2005).
15. D. N. Arvanitis et al., *J. Neurochem.* **103**, 216 (2007).
16. K. T. Dineley, D. Hogan, W. R. Zhang, G. Tagliatela, *Neurobiol. Learn. Mem.* **88**, 217 (2007).
17. L. C. Reese, W. Zhang, K. T. Dineley, R. Kaye, G. Tagliatela, *Ageing Cell* **7**, 824 (2008).
18. Z. Wang, B. Zhang, M. Wang, B. I. Carr, *J. Biol. Chem.* **278**, 11138 (2003).
19. C. Haass et al., *Nature* **359**, 322 (1992).
20. K. Maruyama et al., *Biochem. Biophys. Res. Commun.* **227**, 730 (1996).
21. W. Annaert, B. De Strooper, *Biochim. Biophys. Acta.* **1502**, 53 (2000).

Differential effects of estrogen on memory processes and learning strategies: A selective review of animal studies

Mina Khorashadi*¹

¹Department of Neurology and Neuroscience, McGill University, Montreal Neurological Institute, 3801 University Street, Montreal, Quebec, Canada, H3A 2B4

ABSTRACT

Estrogen has differential effects on learning and memory. The direction of these effects depends on a variety of factors including the type of memory process, task specific demands, dose and time course of treatment. While some processes, including working memory, spatial memory and place learning, are improved in high estrogen conditions, other processes such as amygdala-dependent associative memory, reference memory and response learning are impaired. Furthermore, learning strategy is sensitive to the effects of estrogen. Specifically, high estrogen conditions promote the use of a hippocampus-dependent strategy, while low estrogen levels bias learning towards a response strategy. In humans, the evidence for effects of estrogen on cognitive function is controversial and the mechanisms of action are not fully understood. This review will discuss major findings from animal studies, highlighting the modulatory effects of estrogen on learning and memory, possible neurobiological mechanisms underlying these effects and the implications of these findings for future investigations of the cognitive effects of estrogen in humans.

KEYWORDS

Estrogen, memory, Learning strategies, Hippocampus, Striatum

*Corresponding author:

mina.khorashadi@mail.mcgill.ca

Received: 11 January 2010

Revised: 17 March 2010

INTRODUCTION

Although normally thought to regulate reproductive behaviors, the steroid estrogen also plays a crucial role in learning and memory (1). Investigating the effects of estrogen on learning and memory has been motivated by observations of changes in the cognitive performance of female rats during different phases of the estrus cycle (2, 3), estrogen induced neuronal alterations in brain regions associated with learning and memory (4), and most importantly, epidemiologic observations indicating that estrogen replacement therapy enhances certain cognitive functions and delays the onset of memory disorders in post-menopausal women (1). In recent decades, the effects of estrogen on learning and memory have been the subject of extensive investigation. This paper reviews the major findings from animal studies regarding the modulatory role of estrogen in various memory processes, its effects on competing learning strategies and the potential neurobiological mechanisms that underlie these effects.

EFFECTS OF ESTROGEN ON VARIOUS MEMORY PROCESSES

It is generally accepted that different types of memory are mediated by distinct neural systems (i.e., interconnected brain structures). Support for this view comes from human and animal studies which show dissociations between spatial, response, working and reference memory processes following selective lesions to the hippocampus, striatum and the prefrontal cortex, respectively (5). Similarly, the steroid estrogen has been shown to modulate different memory processes by differentially affecting distinct brain regions implicated in memory (6).

WORKING AND REFERENCE MEMORY

In 1998, Fader *et al.* investigated the effects of estrogen on the performance of ovariectomized female rats in the radial arm maze (7). In this task the same subset of arms were baited in each trial and the remaining arms always remained unbaited. A working memory error constituted reentry to a baited arm and a reference memory error was committed when the animal entered an arm that was never baited. Half of the animals received estrogen injections that produced circulating levels typical of diestrus, the phase of the estrus cycle in which estrogen level is intermediate. The results showed that the animals receiving estrogen committed significantly fewer working memory errors than those who did not receive estrogen but that estrogen had no significant effect on reference memory. Estrogen-induced improvements in working memory have also been observed in other variations of the radial arm maze tasks (8, 9). In contrast, a study by Davis *et al.* showed that high levels of estrogen significantly improve reference memory but have no effect on working memory in the radial arm maze task (10). Interestingly, different doses of estrogen were used in these studies. In light of the slight differences in the experimental designs across these studies, it is important to consider whether the effects of estrogen on working and reference memory are dose-dependent.

In 2002, Holmes *et al.* designed an experiment to determine whether variable doses of estrogen result in different effects upon working and reference memory processes (11). Ovariectomized female rats were injected with high physiological doses (1.00 µg and 5.00 µg) and low physiological doses (0.32 µg) of estrogen and were tested on the working and reference memory versions of the radial arm maze. The results indicated that high physiological doses of estrogen impaired working memory whereas low physiological doses enhanced working memory. On the other hand, there were no significant differences between the high and low dose groups for reference memory. The evidence demonstrates that estrogen has a dose-dependent influence on working memory but the mechanisms through which different doses modulate this memory process are poorly understood.

ASSOCIATIVE LEARNING AND MEMORY

It has been shown that the amygdala plays a critical role in various forms of associative learning and memory (12). Though, only a few studies have investigated the role of estrogen on amygdala-dependent associative memory, the results consistently suggest that estrogen disrupts this type of memory function.

Conditioned place preference, a type of amygdala-mediated associative memory, is adversely affected by high levels of estrogen (13). In a study by Galea *et al.*, ovariectomized female rats were trained in a radial arm maze task in which only two non-adjacent arms were open. One of the arms was baited during all training trials and both arms were left unbaited during the test trial. Preference for an arm was determined by the amount of time the rat spent in each arm during the test trial. The results indicated that ovariectomized rats treated with vehicle (i.e., non-estrogen treated group) had a significant preference for the arm that was baited during training trials, while estrogen treated rats showed no preference for either arm. In other words, estrogen-treated rats were impaired in the task.

Contextual fear conditioning is another form of amygdala-dependent memory process. In one study, for example, male rats exhibited faster fear conditioning than female rats (14). Thus, it appears that high estrogen conditions disrupt amygdala-mediated memory functions. This view is further supported by reports which demonstrate that estrogen attenuates contextual fear memory in female rats (15, 16).

SPATIAL LEARNING AND MEMORY

It is generally accepted that the hippocampus processes spatial and contextual information (5, 17). Various lesion and pharmacological treatment studies indicate that this region is critical for spatial learning and memory (18-21). The effects of estrogen on spatial memory processes are not fully understood and the results are inconsistent; while some studies report estrogen induced enhancements in spatial memory, others demonstrate the opposite.

Packard *et al.* examined the effects of peripheral and intrahippocampal injection of estrogen on spatial memory in a Morris water maze task (22). In this task, a platform is submerged in an opaque liquid so that it is hidden from view. The rat is placed in the maze from different starting positions and must learn the location of the platform using distal cues in the environment (23). This experiment, which used ovariectomized female and intact male rats, showed that peripheral and intrahippocampal estrogen injections enhanced memory retention at 24 hours post-training, but only if the injection occurred immediately after training and not after a 2-hour delay. In contrast, other studies using the same task have reported that high circulating levels of estrogen impair spatial learning (24-27). It is important to note that in these

studies, levels of circulating estrogen were manipulated before rather than after training. Thus, it is possible that high estrogen conditions impair *performance* but not *acquisition* of the task. Korol and colleagues observed that rats in the water maze with high circulating levels of estrogen have an increased tendency to swim along the walls compared to rats with low levels of circulating estrogen (25). This behavior may predispose the animal to use an inefficient search strategy that can result in poor performance on the task. Thus, this impairment in performance may then be falsely interpreted as a disruption in learning.

EFFECTS OF ESTROGEN ON LEARNING STRATEGIES

While studies that manipulate estrogen levels during learning and performance of a task are inconclusive with regards to memory retention and rate of acquisition in certain tasks, they can be effective in determining the influence of estrogen on the learning strategy used to solve a task. Learning the location of an object in a maze may be solved by two different strategies: the spatial strategy involves learning the location of the object in relation to distal cues in the environment and is dependent on the hippocampus, while the response strategy involves learning the location of the object in relation to one's self and is dependent on the function of the striatum (5). Learning the place and the response tasks *require* the use of spatial and response strategy respectively.

In a study by Davis and colleagues, performance on the place and response version of the eight-arm radial maze was compared between ovariectomized female rats receiving estrogen replacement (OVX + E) and ovariectomized females without estrogen replacement (OVX) (10). Estrogen was administered systemically via 60-day release pellets. Learning rate was considered the number of training days the rat required to reach criterion. The results showed that OVX + E rats acquired the place task significantly faster than the OVX rats. On the other hand, OVX rats required fewer days to learn the response task and showed impairment in learning the place task compared to estrogen-treated rats. These outcomes are in agreement with the observations reported by Korol and colleagues (28), and support the hypothesis that hippocampus-dependent learning (spatial learning) is facilitated by high estrogen states, whereas striatum-dependent learning (response learning) is enhanced in low estrogen and impaired in high estrogen conditions.

Further studies have shown that place and response learning are impaired by lesions to the hippocampus and the striatum respectively (29). Moreover, compromising hippocampal function promotes response learning, while dysfunction of the striatum facilitates place learning (30, 31). These inverse findings suggest that

there may be a competitive interaction between the hippocampus and the striatum during learning, such that intact function of one structure somehow obstructs the relative contributions of the other to the task. Similarly, estrogen may modulate the relative contribution of the hippocampus or the striatum to task learning, biasing selection of one strategy over the other (32).

In a dual solution T-maze task, which can be solved by a spatial or a response strategy, female rats in proestrus (the estrous cycle phase during which circulating estrogen levels are high) have an increased tendency to use a spatial strategy to solve the task. Conversely, rats in estrus (the low estrogen phase of the cycle) are more likely to use a response strategy. Rats in diestrus (intermediate estrogen phase) show no bias towards either strategy (33). These findings support the notion that high levels of estrogen bias learning towards a spatial strategy, whereas low estrogen levels promote the use of response strategy. Further support for this finding comes from a study that used a dual solution version of the water maze task. Similar to previous findings, rats with high circulating estrogen levels exhibited a preference for the spatial strategy whereas, low levels of estrogen promoted the use of the response strategy (34).

SITE OF ESTROGEN'S EFFECTS

In the studies discussed above, estrogen administration was manipulated systemically, resulting in a model comparable to intact rats that went through the estrous cycle regularly. Specifically, estrogen was present throughout the nervous system including both the hippocampus and the striatum in all tasks; thus, the exact mechanism by which estrogen affects learning strategies is not clear. One possibility is that estrogen affects only the hippocampus to improve place learning and that impairment in response learning is a consequence of the increased competitive edge of the hippocampus over the striatum. An equally plausible explanation is that estrogen modulates learning through site specific effects: it directly targets the hippocampus and the striatum to improve place learning and impair response learning, respectively (32).

A study by Zurkovsky and Brown was conducted to further investigate the mechanism by which estrogen alters place versus response learning. Estrogen was injected bilaterally into the hippocampus or the dorsal striatum of ovariectomized female rats. The animals were trained and tested on the response and the spatial learning version of the Y-maze task. In the response version of the task, the location of the reward changes in each trial and the animal enters the maze from a position such that the reward is always located on its right hand side. In the spatial version of the task, the location of reward is constant in all trials and the animal enters the maze from a different starting position in every trial. Thus, the animal must learn the reward location

relative to distal cues in the room. The results of this experiment demonstrated a simple dissociation: intrahippocampal estrogen infusion only enhanced place learning without affecting response learning, whereas intrastriatal estrogen infusion only impaired response learning and did not influence place learning. The data from this experiment suggest that estrogen modulates response and place learning by directly acting on the striatum and the hippocampus respectively, most likely through independent molecular mechanisms at these brain regions (29).

NEUROBIOLOGICAL MECHANISMS UNDERLYING EFFECTS OF ESTROGEN ON LEARNING STRATEGIES

In addition to behavioral observations, neurobiological investigations have attempted to explain the differential effects of estrogen on learning and memory (6, 35). It has proven to be a challenge, however, to produce a precise working model of how estrogen interacts with the hippocampus and the striatum to modulate learning strategies. Various neurotransmitters including acetylcholine and dopamine, NMDA receptors and processes involved in synaptic plasticity have been implicated in mediating the effects of estrogen in the brain.

ACETYLCHOLINE

Substantial evidence indicates the important function of the cholinergic system in learning and memory (36–38). In 1997, Packard *et al.* observed that memory enhancing effects of estrogen may be blocked by small doses of an acetylcholine receptor antagonist. Furthermore, injections of sub-effective doses of an acetylcholine agonist along with estrogen produce synergistic memory enhancing effects (39). The results suggest that estrogen modulates hippocampus-dependent memory processes through interactions with the cholinergic system. Further evidence suggests that administration of estrogen enhances learning-induced acetylcholine release during place tasks and increases acetylcholine levels in ovariectomized rats (40). The estrogen-driven increase in acetylcholine reduces the overall transmission of the inhibitory neurotransmitter GABA, which results in reduced inhibition of CA1 pyramidal neurons in the hippocampus (10). This reduction in inhibition increases the overall excitability of the region, enhancing the function of the hippocampus which may ultimately result in improvement in place learning (41).

NMDA RECEPTOR AND LONG TERM POTENTIATION

In the past two decades numerous studies have proposed that long term potentiation and synaptic plasticity are (amongst) the underlying molecular mechanisms of learning and memory (42, 43). Both these mechanisms involve altering synaptic activity: long term potentiation refers to the strengthening of synapses based on recent patterns of activity, and plasticity refers to over-

all structural and functional changes at the synapses. It has been shown that blocking long term potentiation impairs learning and memory and that this process is dependent on the functional integrity of the N-methyl-D-Aspartate (NMDA) receptors (44–46). High estrogen levels in the hippocampus increase NMDA receptor binding density (47). Furthermore, estrogen replacement can reverse the reduction in NMDA binding density produced by ovariectomy. Finally, long-term potentiation is strongest during high estrogen states (48) and estrogen alleviates detriments in long term potentiation that are caused by NMDA receptor antagonists (49). Thus, it appears that high estrogen conditions produce a series of interacting effects that facilitate excitability and synaptic plasticity in the hippocampus, which ultimately enhance hippocampus-dependent learning. In contrast, estrogen in the striatum reduces NMDA receptors binding density which may impair long term potentiation and synaptic plasticity in this structure and ultimately resulting in deficits in response learning (47).

DOPAMINE

The mechanisms through which estrogen affects striatum-dependent learning are less understood. The striatum lacks α and β estrogen receptors (50), implying that a direct effect via estrogen receptors is unlikely and that other mechanisms must be involved. The most widely reported effect of estrogen on the striatum is by interactions with the dopamine system. Numerous studies have shown that estrogen increases the levels of dopamine in the striatum (51). Behavioral findings indicate that intrastriatal administration of amphetamine, a treatment which increases dopamine release, enhances striatum-dependent learning (52). Given that estrogen increases dopamine release in the striatum and that dopamine agonists such as amphetamines improve response learning, it is quite puzzling that estrogen has detrimental effects on striatum-dependent learning.

It is likely that other neurotransmitter systems also play a role in mediating the effects of estrogen on the striatum. Acetylcholine is a good candidate since estrogen has been shown to modulate its transmission in the striatum; low levels of estrogen decrease acetylcholine levels by reducing the concentration of the acetylcholine-synthesizing enzyme choline acetyltransferase (53). Acetylcholine is used by the tonic (constantly) active striatum interneurons. These interneurons persistently inhibit the dopaminergic cells, resulting in low basal levels of dopamine in the striatum (10). Thus, in low estrogen conditions, reduced cholinergic transmission reduces inhibition of dopaminergic neurons resulting in an increased basal levels of dopamine (54, 55). So far, it appears that both high and low estrogen states ultimately result in increased dopamine transmission in the striatum. It is important to note however, that high estrogen levels result in an overall increase in tonic basal levels and may not affect the

phasic dopamine release in the striatum (56). Phasic dopamine release, characterized by high frequency and transient activity of dopaminergic neurons, results from perception of novel environmental stimuli and is thought to be important for response learning (10, 57). Therefore, it is possible that in high estrogen conditions basal dopamine levels are so high that they mask the phasic release of dopamine in the striatum, resulting in impairment of striatum-dependent (response) learning.

DISCUSSION

Several lines of evidence from animal studies indicate that estrogen differentially modulates memory processes. While estrogen improves some processes such as working and spatial memory, it may cause impairment in others such as amygdala-dependent associative memory. The direction of estrogen's effect on these processes is further complicated by variables including dose of treatment and task specific demands such as use of a certain strategy.

Increased estrogen levels promote spatial strategy and impair the use of response strategy. Importantly, relatively low levels of estrogen do the exact opposite, impairing spatial strategy and facilitating the response strategy. Findings from studies of estrogen infusion into the hippocampus and striatum indicate that the effects of estrogen on these structures are direct and site specific. More importantly, the data show that estrogen's effects on place and response learning are independent from each other and that impairment in response learning is not simply a consequence of improved hippocampal function. It is not known, however, whether estrogen deprivation, which improves response learning, acts on the hippocampus and the striatum in a similar direct and site specific manner (32). Estrogen differentially affects plastic processes (e.g. receptor binding density, long term potentiation) across neural structures. In the hippocampus, estrogen interacts with the cholinergic system to reduce transmission of GABA and increase excitability of this structure. Furthermore, estrogen increases NMDA receptor binding density which enhances long term potentiation and synaptic plasticity. In the striatum, however, estrogen interacts with the acetylcholine and the dopamine systems to produce a series of effects which result in reduced NMDA binding density and plasticity.

The nature of estrogen's effect on plasticity is not fully understood; the hippocampus contains both α and β estrogen receptors while the striatum does not, suggesting that the effects of estrogen on this structure may be through an indirect mechanism. Despite this, neurons in both structures respond very rapidly to estrogen (58, 59), implying non-genomic effects through cytoplasmic signaling pathways following membrane or extracellular receptor activation. Thus, it is unknown whether the effects of

estrogen in these brain structures are carried through similar or different receptor or subcellular mechanisms.

The effects of estrogen are made even more complex by the evidence that suggests that duration of estrogen exposure or deprivation, and the age of the animal all play a role in determining the cognitive and neurobiological efficacy of estrogen. In a dual solution task, continuous estrogen administration to young adult female rats for eight weeks failed to produce a bias towards spatial strategy that is seen following a shorter term estrogen regimen (32). Long term estrogen deprivation due to ovariectomy was also ineffective in producing a response strategy bias. These findings suggest that effects of estrogen on learning strategy change over time. Differential effects of treatment duration have also been seen in aged rats. Cyclic or short term versus long term estrogen regimens are more effective in stimulating plastic changes (60), modulating cholinergic function (61) and learning and memory (62) in older rats.

In sum, animal studies show that effects of estrogen on learning and memory are extremely complex and that the direction of these effects are dependent on specific variables including memory type, learning strategy, dose and time course of treatment as well as age. The notion that estrogen has distinct effects on different memory processes may provide a different interpretation of the findings by the Women's Health Initiative Memory Study which showed no cognitive improvements, or in some cases impairment, in post-menopausal women taking estrogen (63). It is possible that the tests used in these investigations failed to detect task-specific actions of estrogen on cognition known to exist in humans (64). Using a more complete battery of neuropsychological tests that are more sensitive to the effects of estrogen may reveal different findings in which both improvements and impairments due to estrogen are observed. In depth investigation of these effects may provide a better framework for understanding individual differences in learning styles and cognitive changes that occur in aging post-menopausal women and foster the development of more effective treatments for aging related memory disorders.

REFERENCES

1. G. Dohanich, *Current Directions in Psychological Science* **12**, 57 (2003).
2. C. D. Conrad *et al.*, *Pharmacology Biochemistry and Behavior* **78**, 569 (2004).
3. E. J. M. a. M. Zecevic, *Psychobiology* **25**, 246 (1997).
4. K. M. Frick, J. Berger-Sweeney, *Behavioral Neuroscience* **115**, 229 (2001).
5. S. J. Y. Mizumori, O. Yeshenko, K. M. Gill, D. M. Davis, *Neurobiology of Learning and Memory* **82**, 278 (2004).
6. D. Gary, *Current Directions in Psychological Science* **12**, 57 (2003).

7. A. J. Fader, P. E. M. Johnson, G. P. Dohanich, *Pharmacology Biochemistry and Behavior* **62**, 711 (1999).
8. J. M. Daniel, A. J. Fader, A. L. Spencer, G. P. Dohanich, *Hormones and Behavior* **32**, 217 (1997).
9. H. A. Bimonte, V. H. Denenberg, *Psychoneuroendocrinology* **24**, 161 (1999).
10. D. M. Davis, T. K. Jacobson, S. Aliakbari, S. J. Y. Mizumori, *Neurobiology of Learning and Memory* **84**, 132 (2005).
11. M. M. Holmes, J. K. Wide, L. A. M. Galea, *Behavioral Neuroscience* **116**, 928 (2002).
12. A. Mayes, D. Montaldi, E. Migo, *Trends in Cognitive Sciences* **11**, 126 (2007).
13. L. A. M. Galea *et al.*, *Behavioural Brain Research* **126**, 115 (2001).
14. S. Maren, B. De Oca, M. S. Fanselow, *Brain Research* **661**, 25 (1994).
15. C. C. D. Altemus M., Dolan S. and McEwen B.S., *Bio. Psychiatry*, 14S (1998).
16. R. R. Gupta, S. Sen, L. L. Diepenhorst, C. N. Rudick, S. Maren, *Brain Research* **888**, 356 (2001).
17. J. O'Keefe, Nadel, L., in *Oxford University Press*. (Oxford, UK, 1987).
18. G. Riedel, *Progress in Neuro-Psychopharmacology and Biological Psychiatry* **33**, 751 (2009).
19. P. E. Gilbert, A. M. Brushfield, *Progress in Neuro-Psychopharmacology and Biological Psychiatry* **33**, 774 (2009).
20. N. M. White, R. J. McDonald, *Neurobiology of Learning and Memory* **77**, 125 (2002).
21. Z. Guo-rong *et al.*, *Hippocampus* **19**, 413 (2009).
22. M. G. Packard, *Hormones and Behavior* **34**, 126 (1998).
23. R. G. Morris, P. Garrud, J. N. Rawlins, J. O'Keefe, *Nature* **297**, 681 (1982).
24. E. J. Chesler, J. M. Juraska, *Hormones & Behavior* **38**, 234 (Dec, 2000).
25. D. L. Korol, Unik, K., Goosens, K., Crane, C., Gold, P., & Foster, T. C., *Society for Neuroscience Abstracts* **586.9**, (1994).
26. C. A. Frye, *Physiology & Behavior* **57**, 5 (1995).
27. S. G. Warren, J. M. Juraska, *Behavioral Neuroscience* **111**, 259 (1997).
28. D. L. Korol, L. L. Kolo, *Behavioral Neuroscience* **116**, 411 (2002).
29. L. Zurkovsky, S. L. Brown, S. E. Boyd, J. A. Fell, D. L. Korol, *Neuroscience* **144**, 26 (2007).
30. Q. Chang, P. E. Gold, *Behavioural Brain Research* **144**, 19 (2003).
31. A. S. Lee, R. S. Duman, C. Pittenger, *Proceedings of the National Academy of Sciences* **105**, 17163 (November 4, 2008, 2008).
32. D. L. Korol, *Neurobiology of Learning and Memory* **82**, 309 (2004).
33. D. L. Korol, E. L. Malin, K. A. Borden, R. A. Busby, J. Couper-Leo, *Hormones and Behavior* **45**, 330 (2004).
34. J. M. Daniel, C. D. Lee, *Neurobiology of Learning and Memory* **82**, 142 (2004).
35. B. S. McEwen, S. E. Alves, *Endocr Rev* **20**, 279 (June 1, 1999, 1999).
36. B. J. Everitt, T. W. Robbins, in *Annual Review of Psychology*. (1997), vol. 48, pp. 649-684.
37. V. Martinez, M. Sarter, *Behavioral Neuroscience* **118**, 984 (Oct, 2004).
38. G. Pepeu, M. G. Giovannini, *Learning and Memory* **11**, 21 (2004).
39. M. G. Packard, L. A. Teather, *Neurobiology of Learning and Memory* **68**, 172 (1997).
40. J. C. Pych, Q. Chang, C. Colon-Rivera, R. Haag, P. E. Gold, *Learning & Memory* **12**, 564 (November 2005, 2005).
41. R. B. Gibbs, R. Gabor, T. Cox, D. A. Johnson, *Psychoneuroendocrinology* **29**, 741 (2004).
42. Morris RGM, M. BL, *Trends in Neuroscience* **10**, 408 (1987).
43. Abraham W, B. M., *Trends in Neuroscience* **19**, 126 (1996).
44. Morris RG, Anderson E, Lynch GS, B. M., *Nature* **319**, 774 (1986).
45. Davis S, Butcher SP, M. RG., *Journal of Neuroscience* **12**, 21 (1992).
46. Tsien JZ, Huerta PT, T. S., *Cell* **87**, 1327 (1996).
47. M. Cyr, O. Ghribi, T. Di Paolo, *Journal of Neuroendocrinology* **12**, 445 (2000).
48. S. G. Warren, A. G. Humphreys, J. M. Juraska, W. T. Greenough, *Brain Research* **703**, 26 (Dec 12, 1995).
49. I. Gureviciene *et al.*, *Neurobiology of Learning and Memory* **79**, 72 (2003).
50. J. S. Paul, V. L. Malcolm, M. Istvan, *The Journal of Comparative Neurology* **388**, 507 (1997).
51. D. L. Korol, *Neurobiology of Learning and Memory* **82**, 309 (2004a).
52. M. G. Packard, *Hormones & Behavior* **34**, 126 (Oct, 1998).
53. J. Tam, N. Danilovich, K. Nilsson, M. R. Sairam, D. Maysinger, *Neuroscience* **114**, 493 (2002).
54. F. Windels, E. Kiyatkin, *European Journal of Neuroscience* **17**, 613 (2003).
55. F. Zhou, C. Wilson, A. Dani, *Journal of Neurobiology* **53**, 590 (2002).
56. J. J. Fernández-Ruiz, M. L. Hernández, R. de Miguel, J. A. Ramos, *Journal of Neural Transmission* **85**, 223 (1991).
57. G. Morris, Schmidt R, B. H., *Experimental Brain research* **200**, 307 (2010).
58. M. Wong, R. L. Moss, *Journal of Neuroscience* **12**, 3217 (1992).
59. P. G. Mermelstein, J. B. Backer, D. J. Surmeier, *Journal of Neuroscience* **16**, 595 (1996).
60. P. Miranda, C. L. Williams, G. Einstein, *Journal of Neuroscience* **19**, 3316 (1999).
61. R. B. Gibbs, *Neuroscience* **101**, 931 (2000).
62. A. L. Markowska, A. V. Savonenko, *Journal of Neuroscience* **22**, 10985 (2002).
63. M. A. Espeland *et al.*, *JAMA* **291**, 2959 (June 23, 2004, 2004).
64. B. B. Sherwin, J. McGill, *Endocrine Reviews* **24**, 133 (2003).

The discrimination of correlated and anti-correlated motion in the human visual system

Emily R. Lindemer*¹, Ali Syed²

¹Department of Neuroscience, McGill University, McIntyre Medical Building, 3655 Promenade Sir William Osler, Montreal, Quebec, Canada, H3G 1Y6

²Department of Biochemistry, McGill University, McIntyre Medical Building, 3655 Promenade Sir William Osler, Montreal, Quebec, Canada, H3G 1Y6

ABSTRACT

Introduction: How the brain integrates spatial and temporal information is not known. This issue is referred to as the “binding problem” of visual perception. It has been proposed that groups of neurons which correspond to the same elements of an image become synchronous in order to form a coherent neural representation; however, direct experimental evidence supporting this role for neural synchrony is highly controversial. As our perceptual capabilities are limited by the neural mechanism that supports them, an alternative approach to understanding neural synchrony is to instead characterize our ability to perceive synchrony. Thus, our aim was to demonstrate how correlated (i.e., synchronous) motion is perceived by the brain and how its discrimination can be enhanced or impaired. **Methods:** In this study, we used human psychophysics experiments to characterize the ability of subjects to discriminate synchrony in a moving visual stimulus. **Results:** By varying stimulus length, motion speed, and direction we found that humans were less than optimal in their ability to discriminate correlated motion when compared to an ideal mathematical model. In addition, we found that the length of the entire stimulus was not an important factor, but the length of individual motion pulses which made up the stimulus was crucial to performance. **Discussion:** Overall these results suggest that neural synchrony is likely used by the brain, but its resolution is highly limited compared to an ideal model.

KEYWORDS

Temporal structure, Binding problem, Correlation

*Corresponding author:

emily.lindemer@mail.mcgill.ca

Received: 3 January 2010

Revised: 7 March 2010

INTRODUCTION

To understand images as a whole, the brain must break down incoming visual information into basic categories. Many neurons work together in a complex network to integrate local elements into one coherent image; however, the method that the brain uses to break down visual information and piece it back together is still unclear. While several theories have attempted to reconcile this *binding problem* issue (1), one commonly accepted theory is known as *binding by synchrony* (BBS). *Binding by synchrony* suggests that detectors in the brain correspond to different low-level characteristics of an object, such as color, contrast, shape, and spatial and temporal orientation (2). Neurons which respond to each of these categories are able to fire in synchrony, integrating to create a meaningful interpretation of the object as a whole.

Synchrony of motion falls into the category of ‘temporal orientation’ and plays a very important role in visual perception. There are two ways in which this can be interpreted. Motion can either be correlated in the sense of *temporal structure*, or by means of *temporal synchrony*. When motion is correlated via *temporal structure*, the individual elements of a scene follow the same relative motion patterns over time. If, on the other hand, motion is correlated by means of *temporal synchrony*, each element of a scene changes its motion pattern at the exact same time, in the exact same direction. Research has found that the human visual system prefers to use *temporal structure* as a means of integrating synchronous motion when dealing with the binding problem (3). Directional motion is also one of the lower-level binding categories within temporal orientation, and is therefore more quickly and easily processed than higher-level properties such as colour (4). This study supports the preference of using temporal structure to detect synchronous motion. Stimuli were manipulated to test different aspects of synchronous motion, such as speed and length of presentation in human psychophysics experiments. An optimal model was then developed, which was compared against human performance to determine enhancements or impairments in the discrimination of correlated motion. Our stimuli consisted of dot patches moving together horizontally in pulses of different time lengths. Based on previous studies, it was expected that human performance would be enhanced with either the length or number of motion pulses in the stimuli (5). The question also remains whether there is a point at which human performance can no longer increase, and whether this plateau is at the same level as the optimal model.

METHODS AND MATERIALS

The stimulus consisted of two target patches that were 3 cm in diameter, each made up of random dot patterns of equal densities. The two patches were placed equidistantly with their centers 8 cm to the right of and one 3 cm above the centre focal point of the screen, and one 3 cm below, as shown in Figure 1. Motion sequences were generated for each of the two dot patches using two binary sequences. Each binary value corresponded to the direction of one motion pulse with a value of 1 corresponding to rightward motion and a value of 0 corresponding to leftward motion. Each of the two sequences was assigned to one of the dot patches, whose dots then moved accordingly. Random motion sequences were generated for the dot patches, depending on a level of correlation between -1 and 1 that was indicated by the experiment conductor (6). In the motion patterns, all dots in one patch moved together while the patch as a whole remained stationary. The correlation level between the two patches was then observed. A correlation of 1 corresponded to perfect synchrony of motion pattern between the two patches and a correlation of -1

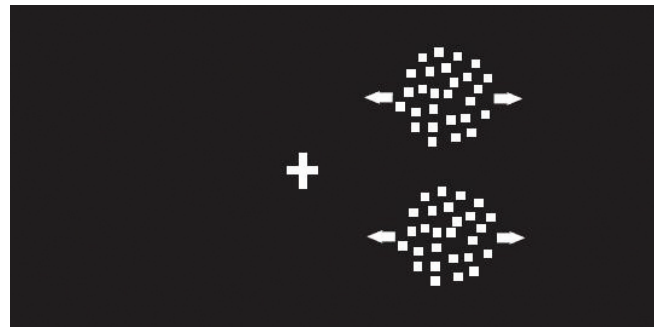


Fig. 1. Dot patches of equal density remained stationary at a fixed, equal distance from the central focal point. The dots exhibited horizontal motion according to the level of correlation specified by the experiment conductor.

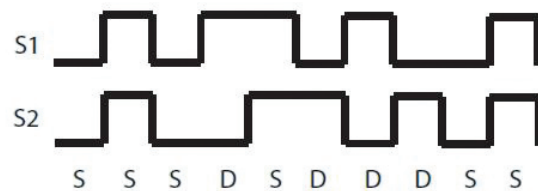


Fig. 2. Two binary sequences were generated for each trial, one corresponding to each dot patch. If the motion of the two patches was the same (S) then the motion patterns were considered “correlated.” If the motion of the two patches was different (D) the motion patterns were considered “anti-correlated.” Ten of these random pulses were generated between the two patches for each trial, with more S pulses in a trial with a higher correlation level and more D pulses in a trial with a lower correlation level.

corresponded to motion between the two patches that was perfectly opposite (Fig. 2). A 17-inch CRT monitor was used with 1280x1024 resolution and subjects were set at a distance of 60 cm from the screen. Random pulse sequences between the dot patches were generated and displayed using the Psychophysics Toolbox application for Matlab™.

Data was collected from human subjects using a two-alternative forced choice (2AFC) motion discrimination task in which the subjects were asked to respond to the motion pattern of the two dot patches with an answer of either “correlated” or “anti-correlated.” Two sets of preliminary trials were run with all subjects. In the first trial, the lengths of the motion pulses were varied while the number of pulses was held constant. In the second trial, the number of pulses presented was varied while pulse length was held constant at 100 milliseconds. This was done to determine which paradigm produced a greater variation in responses. It was found that responses varied more as the length of the pulses varied, rather than as the number of pulses presented in total varied. From this, a formal experiment was developed.

Four subjects were recruited to participate in this experiment (EL, AG, SA, and LM), three of whom were naïve to the purposes of the study, and one was the author. All subjects had normal or corrected-to-normal vision. In the experiment, subjects were asked to view a block of 200 trials per sitting; each trial lasted for the duration of ten pulses. Pulse lengths were varyingly set at five, ten, or twenty milliseconds for the entire trial block of 200. Throughout the trial block, the level of correlation of the motion between the two dot patches varied randomly from -1 (anti-correlated) to 1 (perfectly correlated) on a 0.2 scale. Each correlation level was presented an equal amount of times within the block. Each subject performed 5 blocks per pulse length, totalling 1000 trials per pulse length and 3000 trials in all. Their responses to each trial of “correlated” and “anti-correlated” were collected at the end of each trial block. Data was stored in structure variables with multiple fields by the Matlab™ program. The results from each subject were separated into three groups according to the trial pulse lengths, creating three sets of 1000 trials for each subject. An average proportion of “correlated” responses to all the levels from -1 to 1 were obtained by counting the number of “correlated” responses for each level and dividing by the total. A psychometric curve, which is a plot that is generated to fit the data of correct subject responses as a function of the changing properties of the stimulus, was then generated for each of the three groups. The Nelder-Mead nonlinear optimization method was used to minimize the maximum likelihood function for a logistic fit for the data points. This method is included in Matlab™ software packages where it is implicated in the “fminsearch” function. Three psychometric curves were generated using the average proportion values for each subject.

A model was developed to analyze what the optimal human response should be to trials of different levels of correlation for a stimulus of ten pulses. In this situation, “optimal” refers to a choice made based solely on the majority of pulses being the same or different. This model was developed by generating long motion pattern sequences at all levels of correlation. Then, the probability of two pulses in these sequences being the same (correlated) or opposite (anti-correlated) was determined. Using the generated probabilities given for each level of correlation, the Binomial Cumulative Distribution Function (Eq. 1) was used to determine the likelihood of an observer responding that a stimulus was “correlated” for each level of correlation from -1 to 1 on a 0.2 scale. A value of ten was inserted into the equation for n , corresponding to ten pulses, and a value of five was inserted for

$$F(x, p, n) = \sum_{i=0}^x \binom{n}{i} (p)^i (1 - p)^{(n-i)}$$

Eq. 1

x , corresponding to the number of correlated pulses necessary for an observer to consider the majority of the pulses as being “correlated.” These likelihoods were also generated for stimuli consisting of other numbers of pulses (Fig. 3).

RESULTS

No significant amount of variation was found in the preliminary experiments in which subjects viewed stimuli that varied by the numbers of pulses. Therefore, data was only considered from the experiment in which pulse lengths alone varied and the number of pulses was kept constant at ten pulses per trial.

For each of the three psychometric curves generated per subject, the point of most interest on each curve was at 0 correlation, because when a stimulus has 0 correlation, the subject is essentially guessing as to whether it is correlated or anti-correlated. At this

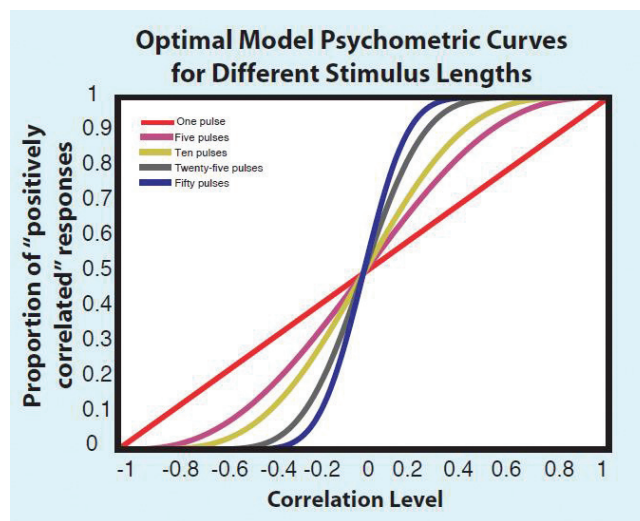


Fig. 3. Optimal model psychometric curves generated for different numbers of pulses. As the number of pulses increased, so did the slope of the curve, as well as the model’s accuracy for detecting whether a stimulus was “correlated” or “anti-correlated.”

point, each psychometric curve had a distinct slope, which could be used to compare the subject’s performance to the optimal model’s performance. Since pulse length did not factor into the optimal model’s performance, and the number of pulses was the only significant characteristic, subjects’ performances for different pulse lengths were all compared against the optimal model’s performance at ten pulses.

As pulse length increased, subjects’ performances became more similar to the optimal model’s (Fig. 4). At pulse lengths of 50 ms, the average slope for all subjects at zero correlation was a low

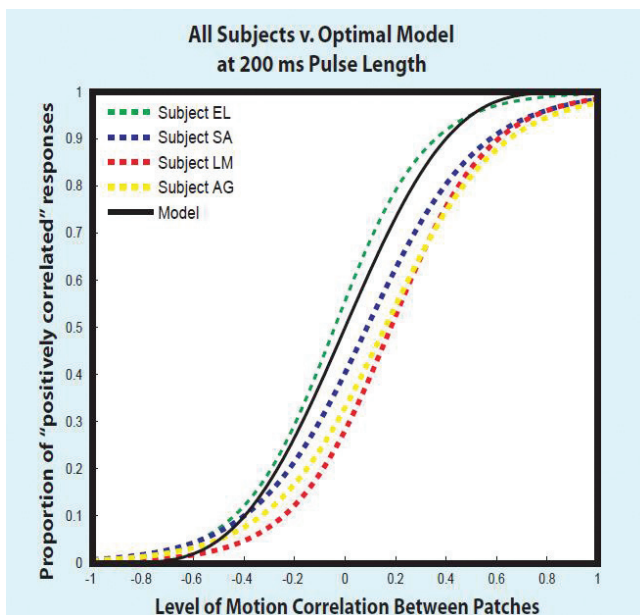


Fig. 4. At the longest experimental pulse length, 200 ms, all subjects' performances became more similar to the optimal model's.

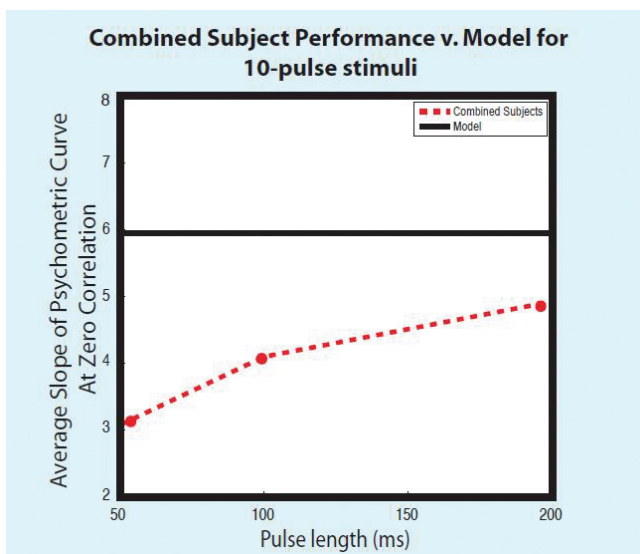


Fig. 5. The slopes of each subjects' psychometric curves were averaged for each experimental pulse length. At 50 ms, there is a great difference between subject slope and the model's slope. As the pulse length increased, the difference between subject slope and model slope became much smaller. Note that the model's slope never changes, as its decision is based solely on majority of correlated pulses, and pulse length is not a deciding factor.

3.09. As the pulse lengths increased, however, so did the slopes of the subjects' psychometric curves. At a length of 200 ms, subjects' average slope was 4.94, in comparison to the optimal model's slope, which at zero correlation for ten pulses was 5.99. The average slopes of all subjects at zero were plotted against the optimal model, with one plot for each of the three pulse lengths (Fig. 5).

DISCUSSION

In this experiment, human performance was determined according to the slope of the psychometric curve during each experimental condition. The slopes were viewed at the correlation level of zero, so as to precisely analyze the differences in response between correlated and anti-correlated stimuli. A higher slope would correspond to a more accurate subject performance, since dependent points on the psychometric curve correspond to proportions of "correlated" responses. At all negative correlation levels, an ideal observer would *never* respond with a "correlated" answer and at all positive correlation levels the response would *always* be "correlated." Human subjects are not ideal observers, however, and statistically the closest that we can come to this ideal observer is shown by the optimal model. With a greater number of pulses, the slope of the optimal model's curve becomes steeper (Fig. 3). When calculating the response probabilities with the Binomial Cumulative Distribution Function, the model's probabilistic response became more accurate with more pulses, leading to steeper curves.

Human performance was expected to approach the level of the optimal model as the number or length of the pulses increased. Preliminary data ruled out the possibility of human performance enhancement through increasing the number of pulses. This result could be due to the brain's limited integration window in perceiving visual stimuli (5). The brain is only capable of integrating with a certain level of accuracy at a given speed and pulse length. Therefore, if the motion patterns in the stimulus move at a set speed and a set pulse length, the number of pulses presented may not affect the subject's performance. Based on this result, a stimulus of ten pulses or one hundred pulses could then be presented at that same pulse length and pulse speed without any significant performance change. Although the pilot trials with increased number of pulses increased the total length of the trials, we can rule out the possibility of increased trial length affecting subject response because of the limiting factor of the brain's integration window.

In contrast, experimental data showed significant performance enhancement with increased pulse lengths and a constant pulse number, which does correspond to the second possible method

of enhancing human performance stated in the original hypothesis. The comparisons between the subjects' psychometric curves and the optimal model's ten-pulse psychometric curve can be seen in Fig. 4. The slopes of all four subjects' curves ranged from 4.5 to 5.5 at 0 correlation with a 200 ms stimulus. According to the model, optimal performance would exhibit a slope of 5.99 with a ten-pulse stimulus. The increasing slope trend is shown in Fig. 5, with the average across-subject slope approaching that of the optimal model, with all stimuli consisting of ten pulses.

The hypothesis also asked whether a threshold exists at which point human performance can no longer improve and if that threshold would equal the model's performance. Trials in this study tested pulse lengths of 50, 100, and 200 ms, and an increasing performance trend was seen throughout. Human performance approached that of the model's (Fig. 5), although the difference between the average slope and the model at the longest pulse length was still greater than 1, which was found to be a significant difference. Although the data presented here satisfies the hypothesis, further experimental data should be collected to determine if even longer pulse lengths can create greater improvement, and if a threshold pulse length exists where the difference between human performance and model performance is not significant. It is clear from this data, however, that human performance is improved with longer pulse length rather than with a greater number of pulses.

CONCLUSION

The results of this experiment appear to support and expand the *binding by synchrony* theory of the Binding Problem. *Binding by synchrony* explains how neurons that correspond to a certain property of an image fire in synchrony, but it does not investigate *why* the groups of neurons fire together or whether this synchronous firing can be made stronger or weaker.

Our data concerns the property of *temporal structure* in BBS. By manipulating temporal structure by varying stimulus pulse lengths, we have elucidated a specific mechanism within the Binding Problem. Here, we were able to study exactly how a certain property of an image can be altered to further enhance or decrease visual integration performance. The influence of temporal structure is more qualitative than quantitative when used as a binding element in visual processing. This was shown by demonstrating that the quality (length of pulses) was more important than quantity (the number of pulses actually presented) when determining whether motion pulses were correlated or anti-correlated.

This knowledge of how visual perception is enhanced qualitatively will help add to our understanding of how the human brain breaks down and integrates information from a dynamic environment to create complete, coherent images. Now that specific parameters have been established under which human performances become more similar to the optimal model, future research will be required to explore how human performance can change in comparison to an optimal model through manipulation of different stimuli, such as background distracters, contrast changes, shifts in which the two patches are offset by one or two pulses (jitter experiments), and spatial changes of the target patches.

REFERENCES

1. A. K. Engel, P. Konig, A. K. Kreiter, T. B. Schillen, W. Singer, *Trends Neurosci* **15**, 218 (Jun, 1992).
2. S. Cheadle *et al.*, *J Vis* **8**, 12 1 (2008).
3. S. E. Guttman, L. A. Gilroy, R. Blake, *Vision Research* **47**, 219 (2007).
4. A. Bartels, S. Zeki, *Vision Res* **46**, 2280 (Jul, 2006).
5. W. R. Uttal, L. Spillmann, F. Stürzel, A. B. Sekuler, *Vision Research* **40**, 301 (2000).
6. t.S. H. Lee, R. Blake, *Science* **284**, 1165 (May 14, 1999).

A new software package to stimulate the pattern of proposed transient chemical structures using the multislice simulation of the Debye-Scherrer diffraction pattern for gold nanoparticles

Lai Chung Liu*^{1,2}, Bradley J. Siwick^{1,2}

¹Department of Physics, McGill University, 3600 rue University, Montreal, Quebec, Canada, H3A 2T8

²Department of Chemistry, McGill University, 801 Sherbrooke St. W. Montréal, Québec H3A 2K6

ABSTRACT

Introduction: Much recent work in physical chemistry focuses on the ultrafast structural dynamics using new experimental tools like femtosecond electron diffraction. Due to theoretical limitations, an efficient modelling methodology is necessary to help identify and extract information on the structure of the sample under study. **Methods:** A software package was created to implement the multislice method for the purpose of dynamically simulating electron scattering in specimens with arbitrary structure. **Results:** We showed that the simulated Debye-Scherrer diffraction patterns of gold nanoparticles are consistent with experimental results. **Discussion:** Our paper demonstrates a reliable and versatile tool that experimenters can use to simulate the pattern of proposed transient chemical structures. These structures can be compared with data.

KEYWORDS

Ultrafast structural dynamics, Multislice method, electron scattering, Debye-Scherrer diffraction patterns

*Corresponding author:

lai.liu@mail.mcgill.ca

Received: 21 October 2009

Revised: 9 March 2010

INTRODUCTION

Given a substance in some physical state and under a certain set of environmental conditions, describe its properties at any later time when a perturbation is applied. Such is the general form of the riddles that natural scientists face. If the changes are of a chemical nature, the problem can be rewritten in the atomistic framework of a chemical reaction—the transformation of an initial system of molecules (reactants) to a final one composed of alternate molecules (products) via some reaction mechanism. Indeed, one of the grand goals of all theoretical and experimental chemists is to provide a real time view of chemical reactions by resolving nuclear motions that accompany the breaking and forming of chemical bonds in the transition state region of a reaction coordinate diagram (1, 2). However, the challenge lies in the extremely rapid speed at which chemical processes operate.

Two notable techniques exist for characterizing the structural properties of chemical reactions on short timescales: X-ray and electron ultrafast diffraction. Like the strobe lights used in slow

motion photography, the periodic ultrafast pulses of probing particles illuminate and capture the atomic structure of matter at an instant in time. Typically, chemical dynamics are initiated with an ultrashort (pump) light pulse and then, at various delay times, the sample is probed in transmission or reflection with an ultrashort electron (5, 4) or x-ray pulse (6). By recording diffraction patterns as a function of the pump-probe delay, it is possible to follow various aspects of the real space atomic configuration of the sample as it evolves during photoinduced structural transformations (Fig. 1). Researchers recently discovered new properties of solid-to-liquid phase transitions using this technique (5).

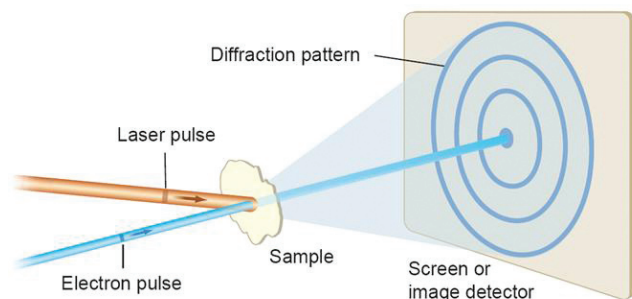


Fig. 1. Illustration of an ultrafast electron diffraction experiment.

Complementary to these novel experimental techniques is the need for an efficient and robust simulation capability. Computer models allow researchers to generate simulated electron diffraction patterns that are based on suggested structures of transient species (7). These results are compared with those obtained experimentally. To perform a simulation, researchers need a numerical method for solving the electron wavefunction in imperfect crystals using a form of the Schrödinger wave equation. Fortunately, many functional algorithms already exist, among which the multislice theory (9) and the Bloch wave method (10) are the most popular.

In this article, we describe a software package developed to take atomic structural data of a sample as input and generate the resulting electron diffraction pattern using the multislice method. We use our software to investigate the structure of gold nanocrystals as a way to test the software's applicability and consistency. We modelled various structural shapes of gold and compared the resulting diffraction images. We chose gold for the ready accessibility of its published data (11). Although much work has been done previously on the simulation of such images (12, 13, 14, 15), the main interest here lies in the development of reliable simulation software that permits direct and complete control over atomic configuration inputs. Such capability could be applied to experiments involving macromolecules, including biological systems (16).

METHODS

KINEMATICAL DIFFRACTION THEORY

The traditional general diffraction theory starts with a plane wave incident on an atom, ψ_{inc} , of wave vector \mathbf{k} , which gives rise to another plane wave and an outgoing spherical wave ψ_{scatt} :

$$\psi_{scatt}(\mathbf{r}) = f(\Delta\mathbf{k}) \frac{e^{i\mathbf{k}\cdot\mathbf{r}}}{|\mathbf{r}|} \quad [1]$$

$$f(\Delta\mathbf{k}) = -\frac{m}{2\pi\hbar^2} \int V(\mathbf{r}') e^{-i\Delta\mathbf{k}\cdot\mathbf{r}'} d^3\mathbf{r}' \quad [2]$$

where $f(\Delta\mathbf{k})$ is the scattering factor for a single scatterer with potential $V(\mathbf{r})$.

In the case of diffraction from a material, the coherently scattered wavelet amplitude from all N atoms in the material can be summed over to get the total diffracted wave $\psi(\Delta\mathbf{k})$:

$$\psi(\Delta\mathbf{k}) = \sum_{j=1}^N f(\mathbf{R}_j) e^{-i\Delta\mathbf{k}\cdot\mathbf{R}_j} \quad [3]$$

where \mathbf{R}_j is the position vector of atom j . This is the kinematical theory of diffraction.

DYNAMICAL DIFFRACTION THEORY

Since the kinematical theory only considers single scattering of electrons, a different approach to scattering is needed in order to include the effects of multiple interactions. To do so, the dynamical theory of diffraction is derived by solving for the electron wavefunction $\psi(x, y, z)$ in the Schrödinger wave equation in a periodic electrostatic potential $V(x, y, z)$:

$$\left[\frac{-\hbar^2}{2m} \nabla^2 - eV(x, y, z) \right] \psi(x, y, z) = E\psi(x, y, z) \quad [4]$$

with $E = \frac{\hbar^2 k^2}{2m}$ for purely elastic collisions. By assuming that the specimen is only a minor perturbation to the electron's motion along the z direction, this equation can be approximated in operator form as

$$\frac{\partial \psi}{\partial z} = [A + B]\psi(x, y, z) \quad [5]$$

$$A = \frac{i\lambda}{4\pi} \left(\frac{\partial^2}{\partial x^2} + \frac{\partial^2}{\partial y^2} \right) \quad [6]$$

$$B = i\sigma V(x, y, z) \quad [7]$$

where A, B are non-commuting operators and σ is an interaction parameter. As suggested by Kirkland (21), this equation has the formal operator solution of

$$\psi(x, y, z) = \exp\left[\int_0^z [A(z') + B(z')] dz'\right] \psi(x, y, 0) \quad [8]$$

After some further algebraic manipulations, a compact iterative solution can be found in terms of a convolution:

$$\psi_{n+1}(x, y) = p_n(x, y, \Delta z_n) * [t_n(x, y)\psi_n(x, y)] \quad [9]$$

where $\psi_n(x, y)$ is the wavefunction after the n th layer of atoms, $t(x, y, z)$ is the transmission function and $p(x, y, \Delta z)$ is the propagator function. Such is the form of the solution that the multislice method is implemented numerically. The action of each steps of the algorithm on the wavefunction is illustrated in Fig. 2.

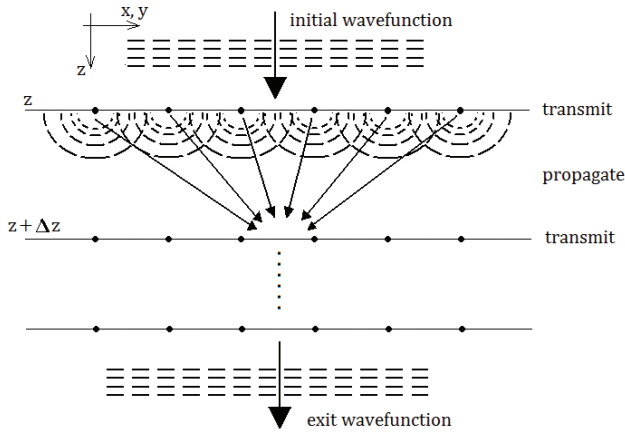


Fig. 2. Simplified diagram of the multislice method for solving the dynamical scattering problem..

In the software implementation, the wavefunction is recursively transmitted and propagated through each slice until it is all the way through the specimen. The diffraction pattern is simply the modulus square of the Fourier transform $\Psi(k_x, k_y)$ of the exit wavefunction $\psi(x, y)$:

$$\Psi(k_x, k_y) = F[\psi(x, y)] \quad [10]$$

$$I(k_x, k_y) = |\Psi(k_x, k_y)|^2 \quad [11]$$

DEBYE-SCHERRER DIFFRACTION

If the crystal structure of the specimen is known, the exit wavefunction of the probe electrons can be reliably simulated, and we can compute the resulting diffraction pattern from a particular zone axis. The width of a typical pulse of electrons is $100 \mu\text{m}$ while that of a nanoparticle is 10 \AA . Thus, the cross sectional area of a pulse can cover on the order of 10^5 particles. Therefore, such an experimental setup would not generate the spotted diffraction pattern of any particular crystal orientation, but a *Debye-Scherrer diffraction pattern* (22), which consists of a series of concentric rings resulting from summing over the diffraction image of randomly oriented particles (Fig. 4). Such patterns arise for polycrystalline and powdered samples.

The Debye scattering equation of kinematical diffraction elegantly describes the radial intensity density function in powder diffraction patterns:

$$I(\Delta k) = |f(\Delta k)|^2 \sum_{m=1}^N \sum_{n=1}^N \frac{\sin(\Delta k R_{mn})}{\Delta k R_{mn}} \quad [12]$$

where the summation is performed over all possible pairs of atoms m, n in the specimen.

In the dynamical theory of diffraction, there is no equivalent expression to Equation [12] for simply computing the scattering intensity function for a random orientation. The multislice method produces the diffraction pattern for a specific orientation (h, k, l) only, $I_{hkl}(\Delta k)$. As illustrated in Fig. 2, an integration over all possible orientations (ϕ, θ) is necessary. This is approximated by a Monte Carlo integration scheme:

$$\bar{I}(\Delta k) = \int_0^\pi \int_0^{2\pi} I(\Delta k, \phi, \theta) d\phi d\theta \quad [13]$$

$$\approx \frac{4\pi^2}{N} \sum_{m=1}^N I(\Delta k, \phi_m, \theta_m) \quad [14]$$

where (ϕ_m, θ_m) are randomly and uniformly selected points on the unit sphere, and N is the number of orientations over which the powder average is taken.

A STRUCTURAL MODEL FOR OUR SPECIMEN

Generating a description of the sample in a form that can be used in a multislice program is the most difficult part of simulating a diffraction pattern. The specimen needs to be described as a

sequence of layers (in the x,y-plane), with a spacing between each layer (along the z-axis). Clearly, not all crystals have such convenient structures. Thus, there is no general procedure to generate its multislice description. Fortunately, gold has a relatively simple structure at standard conditions, with a face centered cubic (fcc) unit cell (24).

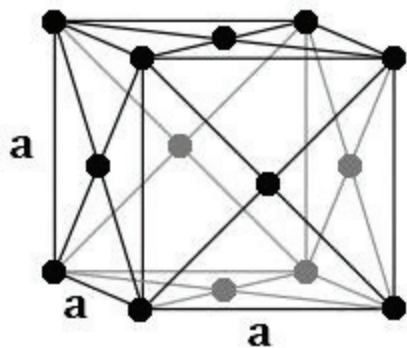


Fig. 3. A ball-and-stick model of a face-centered cubic (fcc) unit cell with lattice parameter a . Adapted from (8).

SIMULATING THERMAL VIBRATIONS IN OUR SPECIMEN

At room temperature, the atoms in the specimen vibrate slightly. Even for heavy gold atoms, the root mean square displacement \bar{u} is 0.1414 Å at 300 K (17). Therefore, it is important to be able to model the effects of thermal energy on atomic structures.

A general theory of diffraction in the presence of thermal vibrations is complicated (18, 19). A rigorous treatment would involve the quantization of these oscillations into quasi-particles (phonons) and apply Bose-Einstein statistics. Given such complexity, the frozen phonon approximation is used to numerically simulate the effects of thermal vibrations in the specimen. Here, each atomic position is displaced by a random amount. However, the outputs of a random number generator cannot be used as the thermal displacement directly since they have an uniform distribution. For the technique to be equivalent to the Debye model of the density of states for phonons, the random offsets need to have a standard Gaussian distribution (20) with \bar{u} as its standard deviation. This is accomplished by applying a Box-Muller transformation on the numbers generated.

OUR SOFTWARE PACKAGE

We developed a software package using the multislice method to model the electron diffraction patterns of gold nanoparticles, taking into account dynamical effects. To simulate the electron diffraction patterns for the gold nanoparticles that take into account dynamical scattering effects, a software package based on the multislice method was developed in the C language while making use of some pre-existing code published by Kirkland

(21). Specifically, our code includes his implementation for parameterizing the Hartree-Fock atomic potentials and for computing the two dimensional discrete fast Fourier transform.

RESULTS AND DISCUSSION

Through a direct application of kinematical diffraction theory, we computed the position and intensity of all the diffraction peaks of gold. Our results consistently match theory. In particular, the diffraction spots are correctly positioned and have the relative intensity profile as predicted by the equations of the kinematical diffraction theory. Therefore, we argue that our implementation of the dynamical multislice theory is sufficiently capable of generating accurate data at each step of the simulation.

Fig. 5 compares the radial intensity density from experimental measurements with results from our software. The actual data was extracted from Fig. 4, a powder diffraction image of 15 nm gold nanoparticles taken in a transmission electron microscope

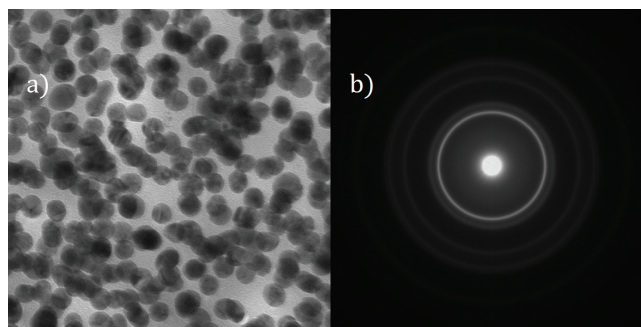


Fig. 4. Experimental data (A) TEM image of 15 nm gold nanoparticles (B) the corresponding powder diffraction pattern.

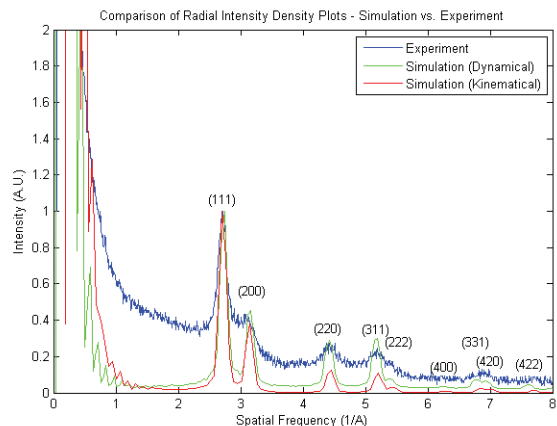


Fig. 5. Comparison of radial intensity density from experimental and simulated diffraction patterns.

(TEM). The simulations were made for 50 Å model gold particles at 300 K in a rectangular array. This graph demonstrates our software's ability to match the radial distance and height of the diffraction peaks in experimental data. However, the kinematical peak intensity decreases too rapidly, leading to significant discrepancy for higher order diffractions such as (200). In this aspect, the multislice method seems to provide a better fit with experimental results. Both approaches fail to emulate the decaying background that is featured in the actual diffraction pattern, but this is acceptable as a known consequence of inelastic electron scattering, a type of interaction not included in either kinematical or dynamical theories. Another potential problem is the broadness of the measured peaks in comparison with the relatively narrow peaks of the simulated pattern. This disparity is probably due to the energy and spatial spread of the incoming electron beam, which tends to broaden diffraction peaks (20). These effects were not included in the current simulation since our software assumes the initial wavefunction is a perfectly monochromatic planar wave.

The central peak, denoted with the Miller index (000), is caused either by the part of the electron beam that has directly transmitted through the sample or by forwardly scattered electrons. Figure 6 shows a plot of the central peak's intensity for several elements as a function of specimen thickness. The onset of these oscillations occurs later for aluminum ($Z = 13$) than for gold ($Z = 79$) or uranium ($Z = 92$). Similarly, the smallest overall decay rate of the intensity occurs for aluminum, and the largest for uranium. This limiting behaviour is consistent with the expectation that the kinematic approach to scattering remains valid for a thicker specimen that consists of lighter atoms with a weaker scattering potential.

Figure 6 also depicts the decaying oscillation of the diffraction intensity. Such behaviour is not predicted by the kinematical theory of diffraction. This reflects the need for a dynamical approach to simulating diffraction in thick specimens. The Debye scattering equation assumes that each atom is a single scatterer and that the final wavefunction is just a sum over the scattered wavelets; therefore, the intensity ought to be constant for any specimen depth. In multislice theory, electrons can scatter multiple times. This causes the forward beam to lose intensity as it leaks out and into diffracted beams. However, the diffracted beam can scatter back into the main beam. This leads to the observed oscillations in intensity at (000) (11). Given these multiple scattering events, low order diffractions, which are nominally forbidden, do occur and rapidly sap away the intensity of main beam. However, as the main beam loses intensity, these unusual scattering events become less likely, leading to a stabilization of the beam intensities.

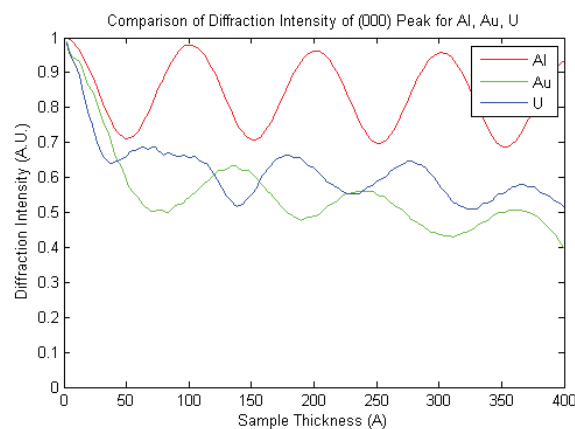


Fig. 6. Comparative plot of the intensity at the (000) point in the simulated diffraction pattern from multislice theory for a film of Al, gold and U. The same lattice structure (fcc unit cell at 4.0782 Å) was used for all three elements.

In Figure 7, we plot the dynamical radial intensity density for different particle diameters. As expected, the overall trend is the progressive sharpening of the diffraction peaks as the size of particles increases. As the number of atoms increases, diffractions favoured by the structure factor rules tend to occur more frequently and thus become increasingly better defined when compared with the kinematically forbidden ones.

Figure 8 plots the dynamical radial intensity density for different interparticle distances. Although no quantitative analysis was made, the main effect of changing the large scale structure of the specimen is an expected broadening of the diffraction peaks. In particular, a decrease in the interparticle distance causes the interference between trans-particle pairs of atoms, and the appearance of high frequency envelope. This peak envelope is simply a sinc function whose frequency is proportional to the interparticle distance.

Figure 9 illustrates the effects of thermal vibrations by comparing the radial intensity density function simulated at different temperatures (0 K, 300 K, 1337 K). Here, the diffraction peaks are observed to be increasingly suppressed as the specimen temperature rises. In addition, the intensity suppression is stronger for higher order diffractions. This is clearly shown in Figure 10, where the intensity of several prominent diffraction peaks is plotted on a logarithmic scale. On this plot, the intensities decrease linearly and do so more strongly for higher order peaks. Both plots are consistent with the effects of the Debye-Waller factor, which has the exponential form e^{-2M} , $M = \Delta k^2 \langle u^2 \rangle$. Therefore, the multislice method, supplemented by the frozen phonon approximation, has correctly reproduced the predicted diffraction features due to thermal vibrations.

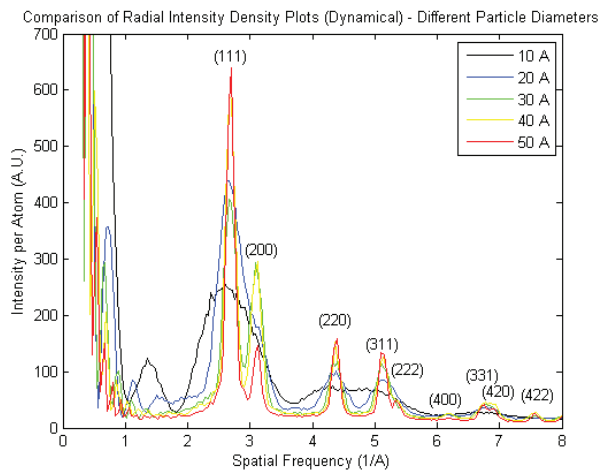


Fig. 7. Comparison of dynamical radial intensity density for different gold particle diameters.

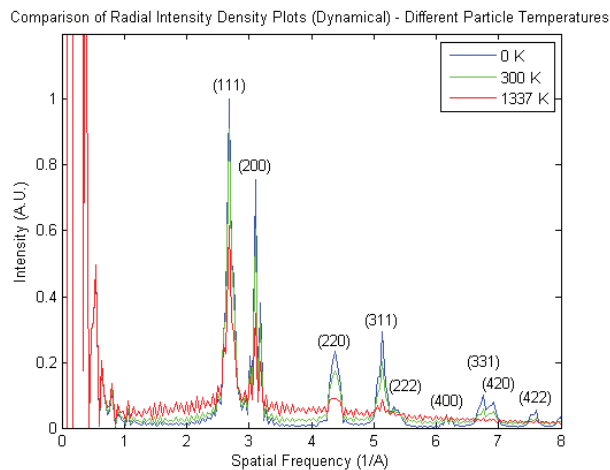


Fig. 9. Comparison of dynamical radial intensity density for different specimen temperatures.

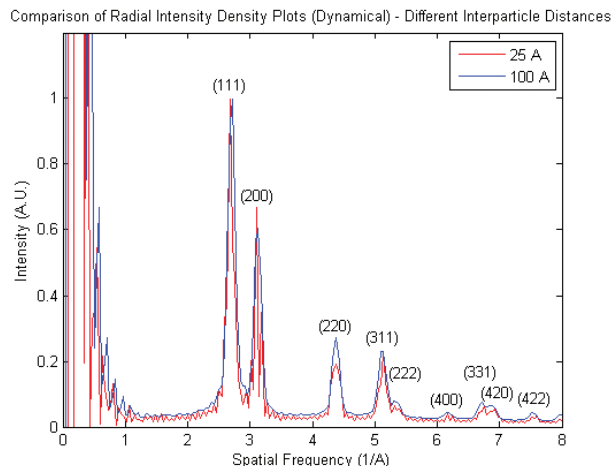


Fig. 8. Comparison of dynamical radial intensity density for different gold interparticle distances.

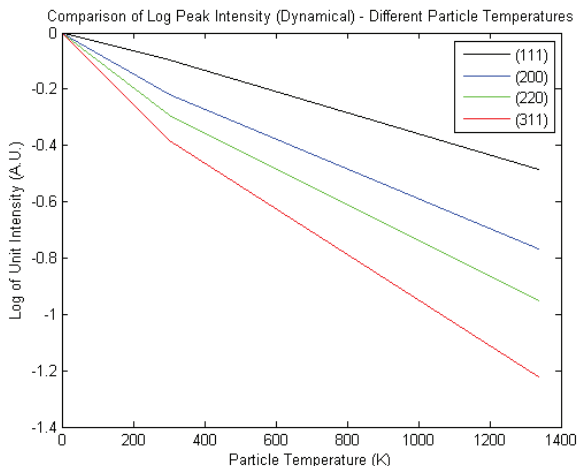


Fig. 10. Comparison of dynamical peak intensity for different diffraction peaks and specimen temperatures.

CONCLUSION

Our results demonstrate that our implementation of the multislice approach is sufficient in attaining our stated goal of generating powder diffraction patterns for gold nanoparticles. In particular, comparison between the dynamical and kinematical results show that the former provides a better fit with experimental results. Further analysis shows that the simple Debye scattering equation is not sufficient for modelling diffraction in 50 Å gold clusters since there are significant dynamical corrections. The main corrections were seen to be progressive peak broadening, suppression of (111) peak intensity, enhancement of higher order peak intensity, and inward peak shift.

Future work entails improving the software package introduced in this article. Some improvements include using complex electron scattering factors (25) to model inelastic scattering, simulating an imperfect initial electron beam by averaging the multislice diffraction pattern over a range of illumination angles to take into account a partially coherent beam (21).

ACKNOWLEDGEMENTS

Much appreciation is owed to all members of the Siwick research group. In particular, Christopher Godbout measured the data in Fig. 4. Finally, I am grateful to McGill University for supporting the work via the Science Undergraduate Research Award.

REFERENCES

1. R. Srinivasan, *et al.*, *Helv. Chim. Acta.* **86**, 1763 (2003).
2. J. R. Dwyer, *et al.*, *Phil. Trans. R. Soc. A* **364**, 741 (2006).
3. R. J. Silbey, R. A. Alberty, M. G. Bawendi, in *Physical Chemistry, Fourth Edition* (Wiley, New York, 2006).
4. C. Y. Ruan, *et al.*, *Science* **80**, 304 (2004).
5. B. J. Siwick, *et al.*, *Science* **302**, 1382 (2003).
6. F. Schotte, *et al.*, *Science* **300**, 1944 (2003).
7. U. Weierstall, *et al.*, *Ultramicroscopy* **90**, 171 (2002).
8. N. W. Ashcroft, N. D. Mermin, in *Solid State Physics* (Holt, Rinehart and Winston, New York 1976).
9. J. M. Cowley, A. F. Moodie, *Acta Cryst.* **10**, 609 (1957).
10. J. C. H. Spence, J. M. Zuo, *Electron Diffraction* (Plenum Press, New York and London, 1992).
11. B. Fultz, J. M. Howe, *Transmission Electron Microscopy and Diffractometry of Materials, Second Edition* (Springer, Berlin and Heidelberg, 2001).
12. W. J. Huang, *et al.*, *Nature Physics* **5**, 129 (2008).
13. L. Guzzi, D. Horváth, *J. Phys. Chem. B* **104**, 3183 (2000).
14. C. Y. Cai, *et al.*, *Micron* **40**, 313 (2009).
15. L. S. Bartell, B. Raoult, G. Torchet, *J. Chem. Phys.* **66**, 5387 (1977).
16. B. J. Siwick, *et al.*, *Chemical Physics* **299**, 285 (2004).
17. E. A. Owen, R. W. Williams, *Proc. R. Soc. Lond. A* **188**, 509 (1947).
18. C. R. Hall, P. B. Hirsch, *Proc. R. Soc. Lond. A* **286**, 158 (1965).
19. J. M. Cowley, A. P. Pogany, *Acta Cryst.* **24**, 109 (1968).
20. C. Kittel, *Intro. to Solid State Physics* (Wiley, New York, 1996).
21. E. J. Kirkland, *Advanced Computing in Electron Microscopy* (Plenum Press, New York and London, 1998).
22. R. E. Dinnebier, S. J. L. Billinge, *Powder Diffraction - Theory and Practice* (RCS Publishing, Chicago, 2008).
23. M. D. Graef, *Introduction to Conventional Transmission Electron Microscopy* (Cambridge University Press, Cambridge, 2003).
24. A. Maeland, T. B. Flanagan, *Can. J. Phys.* **42**, 2364 (1964).
25. Z. L. Wang, W. S. Lang, *Acta Cryst. A* **46**, 366 (1990).

Bisphenol A impacts cardiomyocyte differentiation in vitro by modulating cardiac protein expression

Vimarsha Swami*^{1,2}, Lorraine E. Chalifour^{1,2}

¹Lady Davis Institute for Medical Research, Sir Mortimer B. Davis - Jewish General Hospital, 3755 chemin Côte Ste Catherine, Montréal, Québec, Canada, H3T 1E2.

²Division of Experimental Medicine, McGill University, Lady Meredith House, 1110 Pine Avenue West, Montreal, Quebec, Canada, H3A 1A3

ABSTRACT

Introduction: Bisphenol A (BPA) is an environmental toxin commonly found in plastics and is able to mimic the actions of endogenous steroid hormones. BPA binds and activates intracellular estrogen receptors (ER α and ER β) and estrogen related receptor γ (ERR γ), all of which are present in cardiomyocytes. However, it is unclear how BPA impacts the heart. We hypothesized that BPA modulates the expression of proteins regulating cardiac structure, energy and calcium homeostasis during cardiomyocyte differentiation in vitro. **Methods:** We differentiated H9C2 cells into cardiomyocytes in hormone-replete (RM) or hormone-depleted (HD) media. We co-treated the cells with graded amounts of BPA and pure anti-estrogen ICI 182,780, which blocks ER α and ER β activity. Immunoblotting measured the expression of the structural protein β -myosin heavy chain (β MHC), calcium homeostasis protein sarcoendoplasmic reticulum calcium ATPase (SERCA2a), and the cardiac energy-producing protein creatine kinase (CK). **Results:** Expression of these proteins was hormone-dependent during cardiomyocyte differentiation, with expression highest in RM media after 72 or 96 hours of differentiation. Adding 10⁻⁸ M BPA to HD media increased cardiac structural (β MHC), energy (CK), and calcium homeostasis (SERCA2a) protein expression. Conversely, 10⁻⁷ M BPA added to RM media decreased protein expression. Co-treatment with ICI 182,780 reduced BPA-mediated induction of SERCA2a and CK expression in HD media. **Discussion:** BPA modulates cardiac structure, calcium and energy homeostasis protein expression during cardiomyocyte differentiation in vitro. Moreover, the data suggest that BPA mediates these changes in protein expression through activation of cardiomyocyte ER α , ER β , or ERR γ .

KEYWORDS

Endocrine disruptor, Estrogen receptors, Cardiomyocytes, Anti-estrogen

*Corresponding author:

vimarsha.swami@mail.mcgill.ca

Received: 4 January 2010

Revised: 5 March 2010

INTRODUCTION

Bisphenol A (BPA) is a known endocrine disruptor prevalent in the environment. Endocrine disruptors are environmental chemicals that can mimic the action of endogenous steroid hormones with some shown to alter reproductive tissue development (1). BPA is a component of polycarbonates and other plastics, and can leach into stored foods and drinks. BPA is one of the most common chemicals used in industry today and has the potential to become a major environmental toxin (2). Recent measurements indicate that greater than 92% of people have detectable levels of BPA in urine, indicating continued and chronic exposure (3). In 2008, BPA was judged by Health Canada to be a substance

that may be entering the environment in quantities sufficient to constitute a danger to Canadians' health (4). The daily exposure in Canada, mostly through diet, is estimated to be 0.67 µg/kgBW/day for adults, between 0.8 and 2.27 µg/kgBW/day for children and 0.92 to 4.3 µg/kgBW/day for infants up to 18 months old (4).

Studies have shown that when pregnant rodents were treated with low dosages of BPA, amounts commonly found in human blood and tissue, BPA entered the rodent placenta, accumulated in the fetus, and altered reproductive and non-reproductive tissues (1). BPA has been shown to impact the development of both the male and female reproductive tracts in developing fetuses (1). Chronic exposure to BPA from conception is therefore a widely-prevalent phenomenon. Researchers have shown that BPA acts in a manner similar to sex hormones, and modulates protein expression by binding estrogen receptor α (ER α) and estrogen receptor β (ER β) (5). The activated ERs then activate ER-dependent target transcription (6). Alternatively, studies have also shown that BPA behaves as an endocrine disruptor by binding estrogen related receptor γ (ERR γ) (7). Finally, BPA also inhibits the activity of the thyroid hormone triiodothyronine (T3) (8).

It is well known that men and women develop heart disease differently. Sex hormone activation is thought to play an important role in determining cardiac structure and function, and could account for differences between men and women in developing heart disease, though this is largely unresolved (9). Cardiomyocytes express androgen receptors (ARs), ER α , ER β , and ERR γ (10). Consequently, cardiomyocytes can respond to steroid hormones, and thus can also respond to environmental endocrine disruptors such as BPA. Although the impact of BPA on various mammalian tissues is well documented, little is known about the effects of this endocrine disruptor on the heart structure and function during development. In particular, BPA's possible effects on cardiomyocyte development are largely unexplored and unresolved. Cardiac differentiation requires expression of structural proteins involved in contraction, such as β -myosin heavy chain (β MHC); calcium homeostasis proteins that are also involved in the control of contraction, such as sarcoendoplasmic reticulum calcium ATPase (SERCA2a); and proteins involved in cardiac-specific energy production, such as creatine kinase (CK).

We hypothesize that BPA modulates the expression of cardiac structural, energy and calcium homeostasis proteins during cardiomyocyte differentiation *in vitro*.

MODEL AND EXPERIMENTAL PLAN

We used H9C2 cells in our experiments. This permanent cell line is derived from rat cardiac ventricular tissue (11), and can be differentiated into a cardiomyocyte lineage *in vitro*. We measured

the expression of cardiomyocyte structural (β MHC), energy (CK) and calcium homeostasis (SERCA2a) proteins.

To test our hypothesis, we cultured H9C2 cells in hormone-replete (RM) and hormone-depleted (HD) media, and determined the conditions for optimal differentiation. To test the influence of BPA on differentiation and protein expression, we added graded amounts of BPA to RM and HD media. To test the mechanism of BPA action, we treated cells with both BPA and pure anti-estrogen ICI 182,780, which binds both ER α and ER β with high affinity and blocks putative ER activity.

We expect expression of these important cardiac proteins to rise as differentiation progresses in cells treated with hormone-replete media. We also expect lower protein expression in cells treated with hormone-deficient media, compared with cells treated in hormone-replete media, since we hypothesize that sex hormones modulate gene expression during cardiomyocyte differentiation. We also anticipate increased expression of cardiac-specific proteins in cells treated with both BPA and hormone-deficient media, compared with hormone-deficient controls lacking BPA, as we expect BPA to bind and activate ERs or ERR γ . If BPA does indeed bind the ERs, we anticipate that the effects of BPA on protein expression will be reversed back to control levels when ICI 182,780 is added to cells in culture.

METHODS

CELL CULTURE

H9C2 cells were plated in 60 mm cell culture dishes and cultured in Dulbecco's Modified Eagle Medium (DMEM). Penicillin, streptomycin, and 10% Fetal Calf Serum (FCS) were added (all from Invitrogen). At 90-95% confluency, the media was changed to differentiation media. Hormone-replete differentiation media (RM) contained DMEM, 1% FCS and antibiotics. Hormone-deficient differentiation media (HD) contained phenol-free DMEM, 1% charcoal stripped-FCS and antibiotics. 10^{-8} M Retinoic Acid (RA) (Sigma-Aldrich) was added daily to induce cardiac differentiation. Media were changed every 48 hours for all experiments.

PROTEIN ISOLATION AND IMMUNOBLOT ANALYSIS

Cells were homogenized in SDS lysis buffer containing 62.5mM Tris pH 6.8, 2% weight/volume SDS, 10% glycerol, 50 mM dithiothreitol and 0.01% w/v bromophenol blue. Proteins were separated using 8% SDS-polyacrylamide gel at 80 mV, and then transferred to a Immobilon P blotting membrane (Millipore) at 90 mV for 2 hours at 4 °C using a wet transfer apparatus.

The membranes were stained with Ponceau S, and then blocked with 10% TBS-T (β MHC, CK) or 10% PBS-T (SERCA2a) in

milk for 1 hour. Membranes were then incubated overnight at 4 °C in 5% TBS-T or PBS-T milk containing primary antibody. β MHC primary antibody (MF-20 culture supernatant) was diluted 1:10, SERCA2a antibody (Santa Cruz) 1:100 and CK antibody (Sigma-Aldrich) was diluted 1:1000.

Membranes were then washed 3 x 15 minutes in TBS-T or PBS-T, and incubated for 2 hours at room temperature in 5% TBS-T or PBS-T milk containing horseradish-peroxidase coupled secondary antibody. Anti-mouse secondary antibody (Pierce) was used for β MHC (1:10000 dilution) and Creatine Kinase (1:8000 dilution). Anti-goat secondary antibody (Pierce) was used for SERCA2a (1:5000). After incubation, membranes were washed 3 x 15 minutes in TBS-T or PBS-T. We then performed chemiluminescent detection of specific binding, following the manufacturer's instructions (Pierce, Rockford IL). We then normalized protein levels using the bands obtained from the loading control gels (discussed below).

LOADING CONTROL FOR IMMUNOBLOT ANALYSIS

For immunoblot analysis, 25 μ L of homogenate was loaded in each well. For a loading control, protein samples separated on 8% SDS-Polyacrylamide gels were stained with Coomassie Brilliant Blue 250 to visualize bands. We quantified bands to compare the relative amounts of protein loaded in each well, and all experimental results were normalized to these values.

STATISTICAL ANALYSIS

Normalized and vehicle-corrected values for relative protein expression are shown in Figures 1 to 3. Paired t test was used to compare relative protein expressions when needed. Values of $P < 0.05$ were considered statistically significant.

RESULTS

EXPERIMENT 1: DIFFERENTIATION TIME COURSE FOR H9C2 CELLS IN HORMONE-REPLETE AND HORMONE-DEPLETED MEDIA

To test the impact of sex hormones on the expression of cardiac structural (β MHC), energy (CK) and calcium homeostasis (SERCA2a) proteins during the time course of cardiomyocyte differentiation, a first experiment (Experiment 1) was performed in which protein expression was measured using immunoblotting at 24, 48, 72, and 96 hour intervals after the change to differentiation media (Fig. 1) in HD and RM.

β MHC expression increased with time in RM as the H9C2 cells differentiated into cardiomyocytes (RM 72: $P < 0.002$, RM 96: $P < 0.04$ compared with RM 24). Also, the RM 72 and RM 96 treated cells showed higher β MHC expression than HD treated

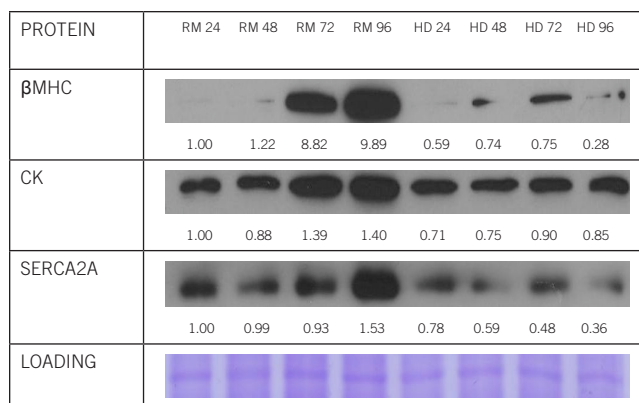


Fig. 1. Differentiation Time Course for H9C2 cells cultured in hormone-replete (RM) media and hormone-depleted (HD) media. Daily additions of retinoic acid induced cardiomyocyte differentiation. Cells were harvested after 24, 48, 72, or 96 hours. Relative protein expression (β MHC, CK, SERCA2a) was measured using immunoblotting. Relative protein expression, quantified using ImageJ software and normalized to Coomassie-stained gel used as loading control, is shown below each immunoblot (values in arbitrary units). These values are averages taken from all repeats conducted. The loading control is shown below the data for the proteins.

cells ($P < 0.002$ at 72 hours, $P < 0.035$ at 96 hours). We observed a similar pattern when the expression of SERCA2a and CK was measured. We observed higher SERCA2a and CK expression in RM treated samples than in HD treated samples, though this difference in expression was less pronounced than what was observed with β MHC. During the differentiation time course for RM treated cells, SERCA2a expression appeared to be highest after 96 hours, and CK expression appeared to be stronger after both 72 and 96 hours.

EXPERIMENT 2: EFFECTS OF BPA ON CARDIOMYOCYTE PROTEIN EXPRESSION IN H9C2 CELLS CULTURED IN RM AND HD MEDIA

To test the hypothesis that BPA modulates the expression of cardiomyocyte structural, energy and calcium homeostasis proteins, we performed a second experiment to compare protein expression in H9C2 cells treated with BPA with control groups not treated with the endocrine disruptor. Cells in the control group were differentiated in RM or HD media alone, while cells in the experimental groups had 10^{-7} M or 10^{-8} M BPA in methanol (MeOH) added to the culture at the time of differentiation induction. Controls for both types of media were treated with an equal volume of MeOH only. Cells were harvested after 72 or 96 hours. Results are shown in Fig. 2.

When 10^{-7} M BPA was added to RM media for 72 hours, expression of the structural protein β MHC was decreased ($P < 0.03$) compared with the RM 72 MeOH control. However, when 10^{-8}

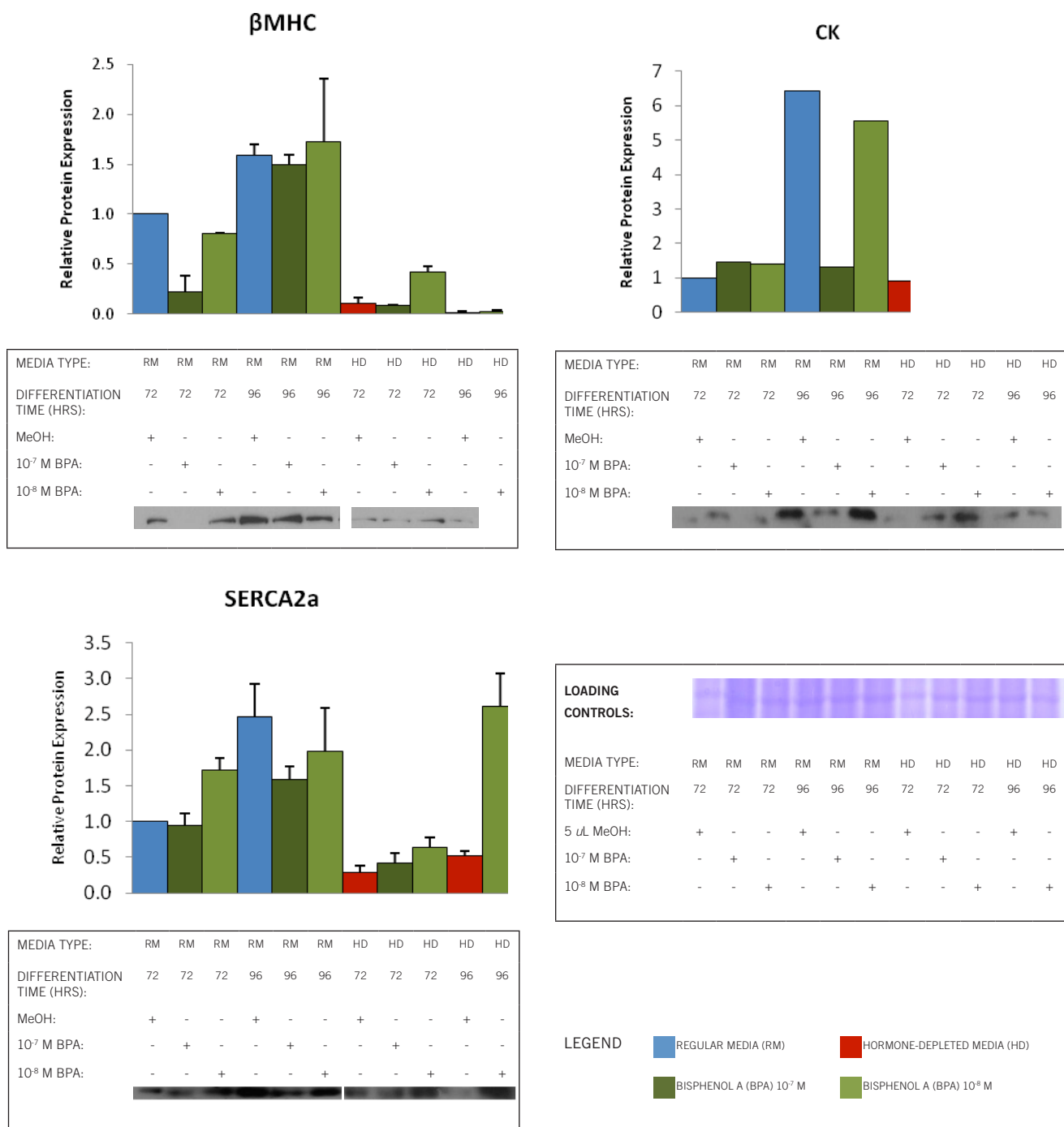


Fig. 2. Impact of Bisphenol A on Cardiomyocyte Differentiation. H9C2 cells cultured in hormone-replete (RM) media and hormone-depleted (HD) media; cells were treated with 10⁻⁷ M BPA, 10⁻⁸ M BPA, or MeOH (controls). Daily additions of retinoic acid induced cardiomyocyte differentiation. Cells were harvested after 72 or 96 hours. Relative protein expression (β MHC, CK, SERCA2a) was measured using immunoblotting. For each protein, immunoblots are shown along with a graphical representation of relative protein expression, quantified using ImageJ software and normalized to Coomassie-stained gel used as loading control. The gel used as a loading control for all 4 proteins is shown below the data for the proteins. The immunoblot images for β MHC and SERCA2a show a 1 minute film exposure for RM samples, and a 5 minute film exposure of the same gel for HD samples. Error bars are shown for β MHC and SERCA2a, for which replicates were performed.

M BPA was added to HD media for 72 hours, β MHC expression was increased ($P < 0.05$) when compared with the HD 72 MeOH control.

CK is a protein involved in energy production. When the expression of CK was measured, expression increased when cells were treated with 10^{-8} M BPA in HD media for 72 hours, compared with the HD 72 MeOH control. For cells cultured in RM media for 96 hours, 10^{-7} M BPA treatment decreased CK expression compared to the RM 96 MeOH control.

The calcium homeostasis protein SERCA2a showed decreased expression in RM media at 96 hours when treated with 10^{-7} M BPA, though the difference was not statistically significant. Cells treated in RM media for 72 hours showed increased expression when treated with 10^{-8} M BPA ($P < 0.053$). Additionally, treating cells in HD media for 96 hours with 10^{-8} M BPA caused a significant increase ($P < 0.05$) in SERCA2a expression compared to HD 96 MeOH controls.

EXPERIMENT 3: TREATMENT WITH BPA AND ANTI-ESTROGEN ICI 182,780

Finally, to investigate whether BPA modulates cardiomyocyte protein expression by binding to ERs, we performed a third experiment. H9C2 cells differentiated in RM or HD media for 72 hours, with both 10^{-8} M BPA and pure anti-estrogen ICI 182,780 (10^{-6} M or 10^{-8} M) in DMSO, were compared with two sets of controls: cells treated with BPA alone, and cells treated with media lacking both BPA and ICI 182,780. Controls were treated with MeOH, DMSO, or both to account for any possible effects the solvents may have on the cells. Immunoblot results are shown in Fig. 3. We concentrated on SERCA2a and CK expression as these were the most strongly influenced by BPA induction in Experiment 2. Statistical analysis was not performed.

Treatment with BPA and ICI 182,780 (10^{-6} M and 10^{-8} M) reduced SERCA2a expression in HD treated cells when compared with both HD 72 BPA 10^{-8} M and HD 72 controls, most particularly when 10^{-8} M ICI 182,780 was added. However, the inclusion of ICI 182,780 treatment increased SERCA2a expression in RM treated cells when compared with both RM 72 BPA 10^{-8} M and RM 72 controls. A similar trend was observed with CK in RM treated cells, with highest expression in cells treated with ICI 182,780 10^{-6} M. Treatment with BPA and ICI 182,780 also appeared to reduce CK expression in HD treated cells when compared with both HD 72 BPA 10^{-8} M and HD 72 controls.

PROTEIN	MEDIA TYPE	RM	RM	RM	RM	HD	HD	HD	HD
	DIFFERENTIATION TIME (HRS)	72	72	72	72	72	72	72	72
CK	MeOH	+	-	-	-	+	-	-	-
	DMSO	+	+	-	-	+	+	-	-
	10^{-8} M BPA	-	+	+	+	-	+	+	+
	10^{-6} M ICI 182,780	-	-	+	-	-	-	+	-
	10^{-8} M ICI 182,780	-	-	-	+	-	-	-	+
CK									
SERCA2a									
LOADING									

Fig. 3. H9C2 cells cultured in hormone-replete (RM) media and hormone-depleted (HD) media; cells were treated with 10^{-8} M BPA + 10^{-6} M ICI, 10^{-8} M BPA + 10^{-8} M ICI, 10^{-8} M BPA + DMSO, or DMSO + MeOH (controls). Daily additions of retinoic acid induced cardiomyocyte differentiation. Cells were harvested after 72 hours. Relative protein expression (CK, SERCA2a) was measured using immunoblotting. Relative protein expression, quantified using ImageJ software and normalized to Coomassie-stained gel used as loading control, is shown below each immunoblot (values in arbitrary units). Values shown were obtained from one experimental trial. The loading control is shown below the data for the proteins.

DISCUSSION

Our H9C2 cell culture system is an effective model to measure changes in cardiac structural, energy and calcium homeostasis protein expression during cardiomyocyte differentiation, and offers an appropriate basis for our experiments. In particular, since treatment with BPA produced noticeable and quantifiable effects on protein expression patterns detected through immunoblotting, our cell culture model could be useful for future research exploring the effects of endocrine disruptors on cardiomyocyte protein expression.

Our results from Experiment 1 show that cells differentiated in the presence of hormones in RM have increased expression of β MHC, SERCA2a and CK during the later stages of the time course experiment, suggesting that H9C2 cells have differentiated into cardiomyocytes by this point. As we expected, HD treated cells show lower cardiac protein expression, likely due to incomplete differentiation. This result confirms that the expression of important cardiac proteins is hormone-dependent

during cardiomyocyte differentiation, and is consistent with our hypothesis that sex hormones play a role in modulating cardiac gene expression. However, HD media contains reduced estrogen, progesterone, androgen, glucocorticoid, thyroid hormone and cortisol. It is unclear if all or only one of these factors contributes to cardiac differentiation. Further experimentation must be conducted to confirm our belief that changes in sex hormone levels specifically contribute to the observed differences in protein expression between RM and HD treated cells.

Our results in Experiment 2 strongly support our hypothesis that BPA modulates cardiac protein expression in cardiomyocytes *in vitro*. Differentiation in HD media with 10^{-8} M BPA, a concentration detectable in human urine (12), for 72 hours caused considerable increases in the expression of the structural protein β MHC and the cardiac energy-producing protein CK, compared to HD controls. We observed the same trend with the calcium homeostasis protein SERCA2a, except the increased expression in HD media due to BPA treatment was most pronounced after 96 hours of differentiation. These results show that BPA modulates the expression of cardiac structural, energy and calcium homeostasis proteins in differentiating cardiomyocytes. Furthermore, these results are consistent with our hypothesis that BPA influences cardiac protein expression by binding and activating ERs or ERR γ . BPA could be binding cardiomyocyte ERR γ and activating ERR γ -driven transcription, as demonstrated in previous studies (13). ERR γ is thought to exclusively drive the transcription of proteins involved in metabolism and energy production (14); however, our results show that BPA modulates the expression of cardiac structural and calcium homeostasis proteins as well. This suggests that BPA may also be activating cardiomyocyte ERs, which would then bind genomic DNA to regulate transcription.

Additionally, treating cells with 10^{-7} M BPA in RM media for 72 or 96 hours noticeably decreased β MHC, SERCA2a and CK expression compared to RM controls in Experiment 2. It is possible that the higher concentration of BPA was toxic, causing decreased ER- and/or ERR γ -driven transcription of cardiac proteins. This is consistent with the notion that BPA is an estrogen-like compound, as it is well known that steroid hormones function optimally in a non-monotonic fashion (15). This means that a low concentration can appear to be more toxic than a higher concentration and vice versa. BPA was effective and modulated cardiac protein expression even in hormone-replete media with all other factors for differentiation present. This suggests that ingested BPA might affect cardiac differentiation *in vivo*.

In Experiment 3, cells were treated with the anti-estrogen ICI 182,780 and BPA. The results we obtained provide further insight on the possible mechanisms of BPA action. If BPA func-

tions by activating ERs, we expect ICI 182,780 to block the ERs and reverse the changes in protein expression caused by adding 10^{-8} M BPA. In HD media, ICI 182,780 appeared to drive SERCA2a and CK expression to even lower levels than those of the controls, or when BPA alone was added to the HD media. This trend suggests that BPA could be modulating SERCA2a and CK transcription by activating ERs. Further experiments should treat cells with a wider range of ICI 182,780 concentrations. The same experiment should also be repeated using other anti-estrogens that block putative ER activity, to test whether they impact results in a similar manner as ICI 182,780.

Our research shows that cardiac protein expression during differentiation is steroid hormone-dependent, and that BPA modulates cardiac protein expression in cardiomyocytes *in vitro*. Future research must be conducted to further understand the mechanisms by which sex hormones and BPA modulate cardiac gene expression. First, we plan to treat cells with higher or lower doses of BPA to identify concentrations at which the estrogenizing effects of BPA are most strongly seen. To identify the main receptor through which BPA functions, the genes encoding ERR γ , ER α and ER β receptors in H9C2 cells can be over-expressed and under-expressed using our cell culture model. An siRNA approach can be employed to downregulate the expression of these same proteins. We can then measure changes in protein expression in BPA-treated cells as receptor expression is varied. We also plan to test whether performing mutagenesis on the consensus binding elements for ER α , ER β and ERR γ in the promoters of cardiac target genes, such as SERCA2a, significantly impacts BPA function in H9C2 cells. Additionally, chromatin immunoprecipitation (ChIP) can be used to assay for ER receptor-DNA binding interactions at SERCA2a or other gene promoters when cells are treated with BPA. Finally, an outstanding question is whether BPA regulates transcription epigenetically in cardiomyocytes, in a manner similar to sex hormones (16). Sodium bisulfite analysis can be used to sequence possible DNA methylations in CpG islands upstream of genes encoding cardiac proteins after BPA treatment.

The results of our study offer valuable insight into the impacts of sex hormones and endocrine disruptors on cardiac tissue. Given the exposure of pregnant women, children and adults to BPA on a daily basis, further research on the impact of BPA on the cardiovascular system is of major importance to public health. The ability of the environmental toxin BPA to impact the heart by functioning as an estrogenizing compound makes it an important target for future research, which could lead to a greater understanding of how sex hormones and environmental endocrine disruptors influence the development of heart disease.

ACKNOWLEDGEMENTS

We thank Amanda Kasneci, Rami Haddad and William Noiles, and the rest of the Chalifour laboratory at the Lady Davis Institute for their guidance, support, and encouragement. Funding support is from the Canadian Institutes of Health Research (CIHR).

REFERENCES

1. C.A. Richter, *Reprod. Toxicol.* **24**, 199-204 (2007).
2. E. Burridge, *Eur. Chem. News.* **17**, 14-20 (2003).
3. A.M. Calafat, X. Ye, L.Y. Wong, J.A. Reidy, L.L. Needham, *Environ. Health Perspect.* **116**, 39-44 (2008).
4. Canada Gazette. Vol 142, 17. April 19, 2008.
5. A. Vivacqua *et al.*, *Endocrine.* **22**, 275-84 (2003).
6. D.C. Dolinoy, D. Huang, R.L. Jirtle, *PNAS.* **104**, 13056-61 (2007).
7. J. Barrett, *Environ. Health Perspect.* **116**, A36 (2008).
8. M. Kruger *et al.*, *Circ. Res.* **102(4)**, 439-47 (2008).
9. J.E. Rossouw, *Cardiovasc. Res.* **53**, 550-57 (2002).
10. C. Grohé *et al.*, *FEBS LETTS.* **416**, 107-112 (1997).
11. J. Hescheler *et al.*, *Circulation Research.* **69**, 1476-86 (1991).
12. K. Becker *et al.*, *Int J Hyg Environ Health.* **212(6)**, 685-92 (2009).
13. Liu X *et al.*, *FEBS J.* **274(24)**, 6340-51 (2007).
14. Giguère V, *Endocr. Rev.* **29(6)**, 677-96 (2008).
15. R. Conolly, W. Lutz, *Toxicological Sciences.* **77**, 151-57 (2004).
16. J.A. Moolman, *Cardiovasc. Res.* **69**, 777-780 (2006).

New insights into template-based protein modeling techniques

David A. Tiberi¹, Minseon Kim*²

¹Department of Anatomy and Cell Biology, McGill University, 3640 University Street, Montréal, Québec, H3A 2B2

²Department of Microbiology and Immunology, McGill University, 3775 University Street, Montréal, Québec, H3A 2B4

ABSTRACT

Introduction: While the development of genomic sequencing methods has greatly improved the efficiency of collecting sequence data, experimental methods to obtain structure information have been lagging significantly. In order to elucidate protein structures, researchers have developed computational structural modeling techniques such as homology modeling and fold recognition (threading). The general consensus is that homology modeling is a superior approach with templates of high sequence similarity to the desired target (>30%), whereas threading is better suited for lower (<30%) sequence similarity templates. We compared recently improved threading algorithms with homology modeling to test the validity of this consensus. **Methods:** The most current versions of MODELLER and I-TASSER were used for model generation. We then used common assessment criteria (N-Dope, Q-mean and PROCHECK) to verify the validity of the models. Structure comparisons were also made using Chimera's Ca root-mean-square deviation. **Results:** Contrary to our prior expectations, the model determined by threading showed similar or even better assessment results in some criteria compared to the model generated from homology modeling. Furthermore, the structure analysis showed that homology modeling and threading protocols yield models with root-mean-square deviations of under 2 Å when used on protein sequences that share sequence identities of at least 30% to the experimentally determined protein template. **Discussion:** We believe that recent improvements in threading algorithms will allow for broader applications of this methodology in large-scale modeling efforts. The fully automated steps could provide time efficacy. In contrast to popular belief in the modeling community, we have shown that threading could be a competitive means of modeling rather than a mere backup method.

KEYWORDS

Homology modeling, fold recognition, template-based modeling, MODELLER, I-TASSER, Alpha-fetoprotein (AFP), Human serum albumin (HSA)

*Corresponding author:

minseon.kim@mail.mcgill.ca

Received: 8 January 2010

Revised: 7 March 2010

INTRODUCTION

Determining the structure of a novel protein from its primary sequence is vital to many aspects of modern biology. Its applications range from drug discovery in the pharmaceutical industry to enzyme optimization for biotechnological uses in industry (1). Due to efforts like the Human Genome Project and improved computing capabilities, the potential for molecular modeling to produce new biological insights has greatly increased (2). Currently, there are about 10.5 million protein sequences available in Swissprot and TrEMBL, of which the protein structures of barely 62,000 have been determined (3, 4). Protein structural

genomics aims to solve one protein structure for each protein family. As long as one protein structure is derived experimentally, structures of proteins in the same family can be solved using computational means (5).

Computational modeling methods are separated into three broad approaches: homology modeling, *ab-initio*, and fold recognition (threading). Template-based modeling methods, such as fold recognition and homology modeling, are the most reliable for predicting the structure of a target protein (i.e., the protein sequence under study). However, their use is limited by the availability of an optimal template, a homologous protein (similarity due to common ancestry) with an experimentally determined structure (6). Homology modeling predicts protein structures based on their sequence similarity to homologous proteins with experimentally derived structures. This approach stems from the idea that evolutionarily related proteins tend to share structural similarities, which enables researchers to predict the structure of homologous proteins. Regions of conserved structure are computationally transferred from the template to target model, while the non-conserved regions are usually calculated with respect to favored energy states. *Ab-initio*, or free modeling, relies on basic thermodynamic assumptions but is not currently a practical modeling option. Lastly, fold recognition depends on limited number of protein structural folds is limited in nature. Thus, remote homologues can be identified through the shared folds between proteins even if sequence similarity is insufficient to identify potential template proteins. Fold recognition consists of placing and aligning the sequence of amino acids against a template structure. The software first searches the fold database, and the best-fitting fragments are selected. If no suitable fold is found in the database, *ab-initio* is used to build that section of the model (7). Consensus in the field of structural bioinformatics holds that homology modeling generates models that are closer to the native protein structure than fold recognition. That is, it produces models with lower root-mean-square deviation (RMSD) to the native protein structure, and it is the preferred approach when sequence similarity to a known template ranges from 30-50%. Fold recognition is mainly used when sequence similarity drops below 30%, since it can identify targets with only fold-level homology (8).

The modeling efforts described in this paper focus on human alpha-fetoprotein (AFP), a 590-amino acid serum protein with three domains (stable and autonomously folding regions) (9). AFP belongs to the blood plasma protein family, which also consists of human serum albumin (HSA), afamin and vitamin D-binding protein. It is produced at a high level by the fetal liver and yolk sac, but only trace amounts are found in normal adults. These background levels of AFP are normally maintained throughout the life of an individual except for a transient eleva-

tion in pregnant females. AFP selectively suppresses cell-mediated immunity and promotes cell proliferation (10). Blood levels of AFP are also used in pregnant women to detect fetal abnormalities such as Down syndrome and neural tube defects (11).

Determining the three dimensional structure of AFP poses several challenges for the structural community. The size and complexity of the molecule makes it difficult to obtain via recombinant DNA methods the amounts needed for x-ray crystallography (12).

However, the availability of experimentally determined HSA structures, that are similar in size (585 amino acids) and share high sequence identity to AFP, allows for computational modeling of AFP. We used template-based methods of homology modeling and fold recognition to build models of AFP based on HSA. While the overall sequence of AFP is 40% identical to HSA, the actual sequence identities for domains I, II and III are 29%, 41% and 48%, respectively (9). Based on the current consensus in the field, we expect that homology modeling will be most successful for domains II and III since they have the highest sequence identity to the HSA template. When sequence identity to the template drops below 30%, as is the case for domain I of AFP, homology-derived models become inaccurate due to sequence misalignment. Consequently, we predict fold recognition will yield a better model for domain I of AFP (13).

METHODS

Template-based modeling techniques were applied on a domain-by-domain basis using the following domain ranges: domain-I (amino acids 2-192), domain-II (amino acids 193-384) and domain-III (amino acids 385-591) (9).

HOMOLOGY MODELING

Homology modeling depends highly on template identification and the quality of the initial alignment. These crucial steps are followed by multiple-template modeling using MODELLER and subsequent loop-refinement.

TEMPLATE IDENTIFICATION

We searched for potential templates in the Protein Data Bank (PDB) using the MODELLER script `build_profile.py`. The script identified an HSA template (1N5U) and a vitamin D-binding protein template (1KXP). Due to its high sequence similarity to AFP, we used the 1N5U template exclusively. For the multiple-template modeling process, we searched the PDB for another HSA template. The difference between the two templates is suggested to be over 2 Å RMSD (14). We therefore selected the HSA structure 1AO6, which differs from 1N5U by 4.59 Å.

MODELLER

MODELLER is a homology modeling program, which creates target models by satisfying spatial restraints. Based on the alignment information, spatial restraints are derived and target models are generated with minimal violation to such restraints. MODELLER was chosen due to its reputation as one of the best performing modeling software available (13, 15). We used Version 9v7 in this experimental protocol. MODELLER uses python scripts for each step of the process, including the manual refinements. It can be run on both Windows and Mac and is available at <http://salilab.org/modeller/>.

MULTIPLE-TEMPLATE MODELING

We aligned template structures using the MODELLER script `salgn_iterative.py`. This script incorporates automatic iteration of the alignment procedure, rendering the parameter values unnecessary. The best alignment result based on a scoring function is displayed as an output file. We used the script `align2d_mult.py` to align the target sequence onto the template structures, incorporating both sequence and structure information. We then used the `model_mult.py` script to generate a set of five different models for each domain of AFP, resulting in a total of fifteen different models.

LOOP-REFINEMENT PROCESS

From the pool of generated models, we selected for each domain the model with the lowest N-Dope score, and hence the highest accuracy. Using DOPE-profiles, which visualize DOPE scores per residue as a graph, we chose residues with higher DOPE scores for the loop-refinement process. Loop regions occur where no conservation is found in the target-template sequence alignment; no conserved structures can be adopted from the template protein structure. For such regions, MODELLER enables *ab-initio* refinement using the script `loop_refine.py`, which gives a number of independently generated alternative loop conformations. The loop conformation with the lowest energy state is selected based on the n-DOPE scores.

FOLD RECOGNITION

AUTOMATED SERVER SELECTION

The most recent (2008) Critical Assessment of Techniques for Protein Structure Prediction (CASP) study formed the basis for the selection of automated threading servers. Using a double-blind approach, organizers make available to the structure prediction community sequences for which the crystallographic structure will be solved in the next few months, and they are challenged to make predictions of these targets. The study selected I-TASSER as the best automated prediction server. In addition, the large repository of published material on this server and its widespread use by the structural community ultimately led us to select it for this experiment.

I-TASSER

The target protein sequence is submitted along with an e-mail address to which the results will be sent. I-TASSER performs profile-profile searching of the PDB using the statistical profiles for sequences based on their tendency to mutate at each position. This enables broader detection of remote homologues that cannot be identified through mere sequence based searches (16). Aligned fragments are then assembled with unaligned fragments, which are built by means of *ab-initio*. The simulation built from this first round is then used by the program in an iterative step that further refines the model and chooses the model with lowest energy conformation as the final output. I-TASSER is available at <http://zhang.bioinformatics.ku.edu/I-TASSER/>.

STRUCTURE COMPARISON AND VISUALIZATION

To compare the models that were built using homology modeling and fold recognition, we created structural alignments using the MODELLER script `salgn_iterative.py`. We then imported the output alignment file in .ali format into Chimera in order to match the alignment onto three dimensional protein structures. Chimera was chosen for visualization since it allows for simple importing of the alignment file, rendering manual adjustments unnecessary. From the imported alignment information, Chimera calculated the C α root-mean-square deviation (RMSD) between the two structures.

FINAL ASSESSMENT STEP

Following model generation, we used N-DOPE, Q-mean and PROCHECK as quality assessment criteria. To simplify the procedure, we used N-DOPE scores to choose the best models for each domain. We then performed Q-mean and PROCHECK assessments upon this selection of top models in order to confirm their quality (17).

N-DOPE

N-Dope is derived from the original DOPE score, which is a statistical potential means used to quantify model accuracy. DOPE scores are not normalized with respect to protein size and have an abstract scale, so they cannot be used to make comparisons between different models. To allow for comparisons, normalized N-Dope scores are used. Lower values are indicative of higher accuracy (14).

Q-MEAN

Q-mean is a combination of five different statistical potentials enabling both global and local structural quality assessment. It is a relatively new assessment web server, which stresses combining several independent quality measures into one score. The web server is available at <http://swissmodel.expasy.org/qmean>.

Table 1. Human serum albumin structures that have been incorporated in template-based modeling

ID	RESOLUTION (Å)	NAME
1AO6	2.50	CRYSTAL STRUCTURE OF HUMAN SERUM ALBUMIN
1N5U	1.90	STUDY OF HUMAN SERUM ALBUMIN COMPLEXED WITH HEME
1GNI	2.40	SERUM ALBUMIN COMPLEXED WITH OLEIC ACID

The summary of each structure including resolution and its identification within the PDB database has been recorded. Homology modeling was performed using 1AO6 and 1N5U while fold recognition used 1N5U.

Table 2. Model assessment control results

	N-DOPE	QMEAN	PROCHECK
DOMAIN-I	-1.824	0.721	91.9%
DOMAIN-II	-1.759	0.698	95.0%
DOMAIN-III	-1.517	0.666	92.6%

As a control, the 1N5U serum albumin structure was analyzed using the three assessment criteria; namely, N-DOPE, Q-mean, and PROCHECK. All domains of 1N5U obtained scores that confirm their stable tertiary structure, which is expected since each domain was experimentally determined.

Table 3. Improvement of the AFP domain models from homology modeling after refinement step

BEFORE	REFINEMENT	AFTER REFINEMENT
DOMAIN-I	-0.838	-1.059
DOMAIN-II	-1.481	-1.611
DOMAIN-III	-0.745	-0.873

The N-DOPE scores of the domain models before and after the refinement step have been recorded. The scores confirm that the refinement has improved the relative accuracy of the models, which was quantified using N-DOPE. The corresponding changes in the DOPE-profile can be seen in FIGURE 1.

Table 4. Assessment results for AFP domain models

	N-DOPE		QMEAN		PROCHECK	
	Homology Modeling	Fold Recognition	Homology Modeling	Fold Recognition	Homology Modeling	Fold Recognition
DOMAIN-I	-1.059	-1.039	0.603	0.608	93.1%	93.0%
DOMAIN-II	-1.611	-1.671	0.611	0.599	91.0%	91.0%
DOMAIN-III	-0.873	-1.083	0.630	95.2%	95.2%	96.0%

The results for fold recognition generated models show slightly higher accuracy compared to the models from homology modeling although they are not as accurate as the experimentally determined structures. These results show that fold recognition was able to obtain models with similar or slightly higher accuracy to those of homology modeling.

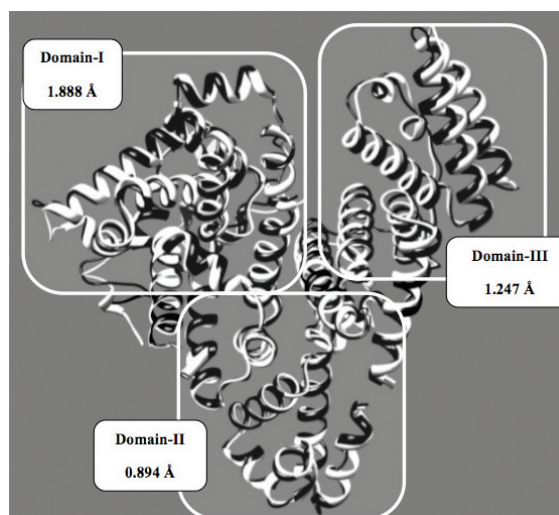


Fig. 1. RMSD measurements between the domain models made by homology modeling and fold recognition. The RMSD measurements have been utilized in order to quantify the similarity between the domain structures made in two different approaches. Yellow frame indicates homology-modeling model, while green indicates fold recognition model.

PROCHECK

PROCHECK assesses a protein model's stereochemistry, including its symmetry, geometry and packing quality (13). Among the many outputs that are given by PROCHECK, Ramachandran plots were the most utilized for our purposes. Each residue is arranged according to their stability; stable and accurate models are expected to have over 90% of their residues fall under the most favored region of the plot. PROCHECK scripts can be obtained by downloading PROCHECK-NT from http://ruppweb.dyndns.org/ftp_warning.html.

RESULTS

The assessment methods allowed us to obtain reference scores to which the generated models are compared. Table 1 describes the templates used. The assessment results performed on 1N5U are listed in Table 2. As expected, the 1N5U domain structures determined by x-ray crystallography yielded scores indicative of a native protein. This was confirmed by the three quality measurements.

Using homology modeling, AFP domain models were generated based on the 1AO6 and 1N5U templates. After the loop-refinement step, the energy profile was rendered more favorable, as evidenced by the N-Dope scores recorded in Table 3. This supports the idea that refinement steps, albeit requiring manual intervention, can improve the model quality significantly. Although all

three domains had N-DOPE scores less than zero, the domain II model has the highest relative accuracy based on N-DOPE scores. Q-mean and PROCHECK values, summarized in Table 4, also confirm that the generated models are within the acceptable range (see Methods for explanation), although the scores are shown to be less accurate than those of the control.

Table 4 summarizes the results obtained using fold recognition. I-TASSER selected 1GNI as the most suitable template, and the resulting models were subjected to the three assessment methods. Like in homology modeling, the N-DOPE scores obtained with I-TASSER were best for domain II, suggesting that domain II models were more accurate than those of domain I or domain III. Also, the N-DOPE scores obtained from fold recognition for domains II and III were more accurate than those obtained via homology modeling.

The overlay between homology and fold recognition models is shown in Fig. 1 along with the images of overlaid domain structures. All RMSD measures are below 2 Å, with domain II structures being the most similar.

DISCUSSION

Generating models of AFP allows for a comparative analysis of fold recognition and homology modeling. Our results challenge several key assumptions about these two techniques. The current consensus in structural bioinformatics is that homology modeling yields more accurate models than fold recognition. However, the assessment data we generated for these models indicate that both are capable of developing highly accurate models in the range of low to medium resolution x-ray crystallographic structures (Table 4).

The prevailing assumptions regarding the accuracy of both homology modeling and fold recognition must be revisited. The consensus is that fold recognition models often have a RMSD of 2-6 Å, with errors mainly occurring in the loop regions (8), while those of homology modeling often approach RMSD of 1-2 Å (18). This dogma was established some fifteen years ago, at a time when both of these techniques were still quite basic and unrefined. We do not dispute that for much of the last decade homology modeling has been the more accurate and preferred method of computational modeling when a template exists with sequence similarities above 30%. However, new algorithms have enabled the latest generation of fold recognition servers to generate models with accuracies that rival or surpass those of homology modeling. This result runs counter to the basic view in much of the published literature, and suggests a change in the assumptions regarding the accuracy of certain computational modeling techniques (19).

This paradigm shift first became apparent when I-TASSER generated the best 3D structure in CASP 7 in the automated server section (6, 20). Two main factors contributed to the success of I-TASSER in this and subsequent competitions. First, an improved template refinement process that uses iteration was introduced, which reduces the RMSD by approximately 1 Å in the aligned regions (20). Furthermore, incorporating the refinement step with iteration skips the manual refinement step usually required during homology modeling. Unlike manual refinement, which is performed during homology modeling, I-TASSER's automated refinement ensures the same strict calculations and algorithms will be applied every time, making the process homogeneous. Secondly, the use of consensus target-template alignments (meta-server approach) by fold recognition software, including I-TASSER, greatly improves model generating capabilities. Consequently, the line between fold recognition and homology modeling has begun to blur.

The most recent CASP studies as well as our modeling work on AFP clearly provide evidence for fold recognition's ability to serve as a viable modeling method, even when sequences share over 30% similarity to known templates. Ideally, when attempting to model proteins with sequences that are 30-50% similar to known templates, researchers are encouraged to utilize both homology modeling and fold recognition approaches. This way, the results generated may be compared to each other, and the most reliable models can be selected. However, if time constraints must be considered, we feel that fold recognition, due to its rapid and user-friendly nature, may be used exclusively to generate models within the same range of accuracy as those made using a homology approach.

While researchers have greatly improved fold recognition servers, it is important to note that due to their automated protocols, bioinformaticians are unable to modulate the level of refinement, and thus the quality, of the resulting model. A novel and potentially timesaving approach would be to generate initial models using fold recognition with subsequent manual refinements using MODELLER. In order to achieve the daunting task of modeling all of the deposited sequences, we believe large-scale structural genomics projects should focus mainly on fold recognition approaches due to their rapid, automated protocols. Although homology modeling can provide viable models, the manual refinement steps require human intervention, thus making this technique impractical for large-scale structural genomic projects. New experimental protocols based on initial fold recognition and subsequent model refinements with MODELLER may allow structural genomic projects to elucidate the vast number of protein sequences yet to be determined.

ACKNOWLEDGMENTS

We would like to thank Dr. Murgita for his guidance and supervision of this project.

REFERENCES

1. K. A. Thiel, *Nature biotechnology*. **22**, 513 (2004).
2. T. Schwede *et al.*, *Structure*. **17**, 151 (2009).
3. Swissprot and TrEMBL (<http://us.expasy.org/sprot/>).
4. RCSB Protein Data Bank (<http://www.rcsb.org/odb/>).
5. M. Tekeda-Shitaka, D. Takaya, C. Chiba, H. Tanaka, H. Umeyama, *Current Medicinal Chemistry*. **11**, 551 (2004).
6. A. Kryshchak, K. Fidelis, *Drug Discovery Today*. **14**, 386 (2009).
7. K. Mizuguchi, *Drug Discovery Today: Targets*. **3**, 18 (2004).
8. Y. Zhang, *Current Opinion in Structural Biology*. **19**, 145 (2009).
9. T. Morinaga, M. Sakai, T. G. Webmann, T. Tamaoki, *Proc. Natl. Acad. Sci. USA* **80**, 4604 (August, 1983).
10. L. Olding, R.A. Murgita R.A. *Reproductive Immunology-Current Topics in Microbiology and Immunology*. pp. 159-187. (1997)
11. C. De Mees *et al.*, *Molecular and Cellular Biology*. **26**, 2012 (2006).
12. R. Boismenu *et al.* *Protein Expression Purification*. **10**:10-26. (2007)
13. Z. Xiang, *Current Protein and Peptide Science*. **7**, 217 (2006).
14. N. Eswar, D. Eramian, B. Webb, M. Shen, A. Sali, *Methods In Molecular Biology-Clifton Then Totowa*. **426**, 145 (2008).
15. C. Sansom, *Biochemist*. **30**, 34 (2008).
16. L. A. Kelley, M. J. Sternberg, *Nat Protoc*. **4**, 363 (2009).
17. D. Eramian *et al.*, *Protein Science*. **15** (2006).
18. R. J. Read, G. Chavali, *Proteins: Struct Funct Bioinfo*. **69**, 27 (2007).
19. Y. Zhang, *Current Opinion in Structural Biology*. **18**, 342 (2008).
20. Y. Zhang, *Proteins: Structure, Function, and Bioinformatics*. **69**, 108 (2007).

Caffeinated alcoholic beverage consumption is associated with binge drinking among Canadian college students

Kerry Weinstein*¹, Zofia Czajkowska¹, Amélie Nantel-Vivier¹, Robert O. Pihl¹

¹Department of Psychology, McGill University, 1205 Dr. Penfield Avenue, Montreal, Quebec, Canada, H3A 1B1

ABSTRACT

Introduction: Binge drinking, characterized by a pattern of excessive alcohol intake on a single occasion, is a growing epidemic among college students. Mixing alcohol with caffeinated energy drinks is also increasing in popularity. Caffeine suppresses the user's ability to accurately assess her level of intoxication and, consequently, the user tends to drink more without realizing the effects. Few studies to date, however, have focused on the association between mixing alcohol with energy drinks and binge drinking. **Methods:** Our study surveyed 221 Canadian college students on their mixing and binge drinking behaviours. We expected to find no significant gender differences in the proportions of both mixers and binge drinkers or in the frequencies of mixing and binge drinking. **Results:** Binge drinkers were more likely to mix than non-binge drinkers, and mixers were more likely to binge drink than non-mixers. Additionally, t-test results showed that mixers were more motivated to drink for the sake of getting drunk than non-mixers were. Surprisingly, these two groups did not significantly differ in the degree to which they felt risk-related behavioral states when they consumed, even though mixers reported significantly more drinking-related life interference. **Conclusion:** Our results demonstrate that preventative programs aimed at reducing high-risk alcohol binge drinking need to consider mixing energy drinks and alcohol intake as a risk factor.

KEYWORDS

Alcohol abuse, Binge drinking, Energy drink, Caffeine

*Corresponding author:

kerry.weinstein@mail.mcgill.ca

Received: 3 January 2010

Revised: 5 March 2010

INTRODUCTION

Alcohol abuse by college students is currently recognized as a substantial public health problem (1). This abuse is characterized by heavy patterns of drinking despite recurrent social, interpersonal, physical or legal problems as a result of alcohol use. Binge drinking, relative to other forms of alcohol consumption, has recently received increased attention among both addiction and public health researchers due to its inherently risky nature and its growing popularity among young adults (2). This form of drinking is defined as the consumption of a sufficiently large amount of alcohol to place the drinker at increased risk of experiencing alcohol-related problems and to place others at increased risk of experiencing second-hand effects (3). For the typical adult, this corresponds to the consumption of five or more drinks in a row for men and four or more drinks in a row for women, due to gender

differences in body mass and alcohol metabolism rates (4). Binge drinking is rampant among American college populations, with recent estimates showing that at least 40–45% of college students engage in heavy drinking episodes each year (2). Although men have historically been found to drink more than women, recent data suggests a further narrowing of gender differences in heavy drinking among young adults (5). This change is at least partly explained by period effects, such as rapidly changing gender roles and the related changes in attitudes to women's drinking.

Motivation plays a role in binge drinking as binge drinkers tend to desire a state of intoxication. This motivational state is suggested by the sheer frequency with which binge drinkers engage in binge drinking. Wechsler *et al.*'s College Alcohol Study, which was based on responses from 14,000 American college students, found that when students were divided by drinking pattern, the median number of drinks per week was 0.7 for non-binge drinkers and 3.7 for occasional binge drinkers (i.e., those who binged less than three times in the previous two weeks) (3). For frequent binge drinkers (i.e., those who binged three or more times in the previous two weeks), however, the median was considerably higher: 14.5 drinks per week. Alarming, 20% of college students were frequent binge drinkers. The College Alcohol Study also revealed that 6% of their sample met the DSM-IV criteria for alcohol dependence, while 31% met the criteria for alcohol abuse. Binge drinking and substance-related disorders may thus substantially overlap. Furthermore, the risk of experiencing a negative outcome, such as engaging in unplanned sexual behaviour or getting injured, increases with the frequency of binge drinking (1).

Recent research suggests that college students' binge drinking is facilitated by the practice of mixing alcohol with caffeinated energy drinks (6, 7). Energy drinks are typically a mixture of caffeine, plant-based stimulants (e.g. guarana), simple sugars, amino acids (e.g. taurine), herbs (e.g. ginseng) and vitamins. Not all contain caffeine; however, the more popular ones do, such as *Red Bull*[®], *Guru*[®], or *Rockstar*[®]. Indeed, caffeine is the main biologically active component of energy drinks, with content ranging from 50 mg (comparable to one cup of coffee) to an alarming 505 mg per can. These drinks are selectively and aggressively marketed to college students, and recent estimates suggest that 34% of 18–24 year olds are regular users (7). Moreover, the ingestion of energy drinks in combination with alcohol is becoming increasingly popular (6, 7). In a 2007 survey of 496 American college students, a quarter of the sample reported mixing alcohol with energy drinks in the past month (8). Of these mixers, half had consumed more than three energy drinks per occasion. Furthermore, while significantly more females (53%) than males (42%) reported to use energy drinks alone, similar proportions of women and men said that they mix energy drinks with alcohol (57% versus 50%, respectively). These results indicate that gender does not influence college students to mix energy drinks and alcohol.

Finally, mixing is not an exclusively American phenomenon. In a survey of 450 students at the University of Messina in Italy, 56.9% of students reported using energy drinks, and 48.4% of this subpopulation frequently mixed energy drinks with alcohol (9). In addition, 35.8% of mixers had ingested this combination more than three times in the past month. No studies to our knowledge, however, have investigated the combined use of alcohol and energy drinks among college students in Canada.

Mixing alcohol with energy drinks has become increasingly popular due to the widely held belief that the stimulant effects of energy drinks counteract the depressant effects of alcohol. Users reason that mixing allows one to drink more for a longer period of time without feeling the associated negative effects to the same extent as alcohol alone. Since 2000, researchers have conducted several peer-reviewed studies centered on this assumption. These studies concluded that energy drinks do not prevent intoxication (10, 11). Rather, the high levels of caffeine found in energy drinks simply mask the intoxicating effects of excess alcohol intake by lessening how drunk the users perceive themselves to be. As measured by physiological indices, however, these individuals are just as intoxicated as they would have been without concurrent ingestion of caffeine. To illustrate, a double-blind study by Ferreira *et al.* found no significant differences in the blood alcohol levels, physiological parameters (heart rate and blood pressure) or biochemical parameters (glucose, cortisol, dopamine) of volunteers who drank alcohol alone compared to alcohol mixed with energy drinks (10). However, those who ingested the combination reported a reduced perception of motor coordination impairment, as well as a reduced intensity of some subjective symptoms of alcohol intoxication such, as headache and dry mouth.

The problem with mixing, therefore, is that caffeine decreases the user's ability to gauge her level of impairment (10), and this can have detrimental consequences. For instance, in a study by Fillmore *et al.*, participants who expected the caffeine in their mixed drinks to compensate for alcohol's depressant effects performed significantly worse on the same psychomotor tests than a second group who were told that the caffeine would have no compensatory effect (11). The latter group seemed to enlist their own compensatory mechanisms whereas the former did not, due to the mistaken belief that caffeine would ameliorate their performance. Thus, mixing energy drinks with alcohol sends the false and dangerous message that the stimulants found in these drinks protect against the effects of alcohol.

Not surprisingly, this false expectation impairs users' assessment of risk and can thereby promote high-risk behaviour, as illustrated by O'Brien *et al.* (6). The authors found that students who mixed energy drinks with alcohol reported nearly double the amount of heavy episodic drinking per month than non-mixers (6.4 days ver-

sus 3.4 days per month), twice as many episodes of weekly drunkenness than non-mixers (1.4 days versus 0.73 days per week), and had a higher prevalence of alcohol-related consequences than non-mixers, including being taken advantage of or taking advantage of another sexually, riding with a drunk driver, being physically injured and requiring medical treatment. Mixers were at a higher risk for these outcomes, even after adjusting for the amount of alcohol consumed.

Although the research community has not fully acknowledged the potential health risks associated with mixing, the aforementioned studies suggest cause for concern. Further research is necessary to understand the mechanisms that relate mixing to an increased risk for alcohol-related consequences. Few studies to date have investigated binge drinking as a potential mediator of this relationship. Moreover, no studies to our knowledge have investigated the association between mixing and binge drinking among Canadian college students. The current study, therefore, investigates the relationship between mixing alcohol with energy drinks and binge drinking among college students at a Canadian university. We hypothesized that no significant gender differences would be found in proportions of mixers and binge drinkers, or in frequency of mixing and binge drinking. We also hypothesized that students who mix would be more likely to binge drink than non-mixers and that binge drinkers would be more likely to mix than non-binge drinkers. Additionally, we expected that mixers would be more motivated to drink for the sake of getting drunk than non-mixers. Finally, we predicted that mixers would feel significantly less risk-related behavioural states (feeling in control, aggressive, daring and sexually uninhibited) when they drink than non-mixers. Paradoxically, we also expected mixers to report significantly more life interference associated with their drinking than non-mixers.

METHODS

PARTICIPANTS

Participants were undergraduate students ages 17-27 (mean age of approximately 20 years), recruited through an advanced undergraduate psychology course at a major metropolitan university in Montreal, Quebec. Age limits were set in order to obtain a sample representative of typical undergraduate populations at North American universities. All participants, except one, met the local legal drinking age of 18 years old. Mature students were excluded because they would likely not exhibit the same drinking behaviours, nor be influenced in the same ways as typical college-aged students. Participants were selected on a voluntary basis, and given course credit for their participation.

MATERIALS

All participants received the Voluntary Anonymous Survey of Drinking Behaviour, which was constructed by the investigators for the purpose of this study. The survey method was chosen because self-reporting is the most common method of data collection used in research on the college student population. Also, past research has demonstrated the accuracy of self-reporting in the assessment of alcohol use (12). The survey contained preliminary demographic questions regarding the participant's age and gender. Next, the definition of 'one drink' was provided (a 12-ounce bottle or can of beer or a 4-ounce glass of wine or a 12-ounce bottle or can of wine cooler or a shot of liquor, either straight or in a mixed drink) to ensure that all of the responses regarding quantity of alcohol consumption were standardized. We then asked 28 questions concerning the participant's: (a) binge drinking behaviour, (b) mixing behaviour, (c) history of alcohol initiation, (d) parents' drinking behaviour and (e) parents' alcohol-specific socialization practices (measures taken to manage or prevent their children's alcohol use). Only items from the first two categories were relevant to our study; the others were used for concurrent studies.

With a slight departure from the traditional definition, our study defines binge drinking as the consumption of five or more drinks per occasion, for both males and females. We asked students to indicate the number of occasions on which they had consumed five or more drinks in the past month. Students who reported at least one occasion of this behaviour were qualified as "binge drinkers" and those that indicated an absence of this behaviour were "non binge drinkers."

The majority of the survey items were based on visual analogue scales (13). This method has been shown to be effective in measuring characteristics or attitudes that range across a continuum of values, making them otherwise difficult to quantify (14). Students were asked to rate on a linear continuum (ranging from never to regularly) how often they drink alcohol in conjunction with energy drinks, how often they drink alcohol with the intention of getting drunk and how often drinking has interfered with important areas of their life. Students were also asked to rate on a linear continuum the extent to which, when they drink, they expect to feel: loss of control to in control, careful to daring, submissive to aggressive and sexually inhibited to sexually uninhibited. We asked students about these behavioural states specifically because the extremes falling to the right end of the spectrum (i.e., feeling in control, daring, aggressive and sexually uninhibited) are all associated with risky behaviour, especially when intoxicated (1).

PROCEDURE

Students were notified a week in advance that the study's survey would be distributed during regular class time, and that their participation would merit course credit. On the day of the study, they were reminded that participation was voluntary and anonymous, and that they could withdraw at any time without consequences. To ensure that students did not feel pressured to participate, the professor (also the study's head researcher) was absent throughout the entire in-class procedure. Research assistants distributed the survey, and gave instructions regarding the visual analogue method. As each survey was handed in, a research assistant separated the last page (containing the participant's identification) from the rest of the survey and placed it in a separate box. This guaranteed both the survey-taker's anonymity and the receipt of course credit given by a third party.

RESULTS

In total, 221 undergraduates participated in the study. The sample comprised 54 males (24.4%), 161 females (72.9%) and six others who did not indicate their gender (2.7%). Ages ($N = 202$) ranged from 17 to 27 years with a mean of 20.32 ($SD = 1.392$).

Table 1. Summary of t-test results for binge drinking frequency between genders

GROUP STATISTICS				
	N	MEAN	STD. DEVIATION	STD. ERROR MEAN
MALES BINGE PAST MONTH	43	3.58	3.81	.580
FEMALES BINGE PAST MONTH	147	2.15	2.43	.201

INDEPENDENT SAMPLES TEST

	t	df	SIG. (2-TAILED)	MEAN DIFFERENCE
BINGE PAST MONTH	2.33*	52.4	.024	1.43

* $p < .05$, therefore significant.

66.1% of students ($N = 146$) were designated as 'binge drinkers' because they reported to have consumed five or more drinks on at least one occasion in the past month. Their mean binge drinking frequency was 3.37 times a month ($SD = 2.91$). Similar proportions of males and females (66.7% versus 65.8%) qualified as binge drinkers. As can be seen in Table 1, t-test results revealed that the genders did significantly differ in their binge drinking frequency, with males binge drinking almost twice as often as females in the past month ($t = 2.331$, $p < 0.05$).

45.7% ($N = 101$) of students said that they had previously mixed alcohol with energy drinks at least once and were therefore categorized as 'mixers'. This group reported that they mixed alcohol with energy drinks on average 32.5% of the time that they drank ($SD = 26.13$). When a history of mixing (yes versus no) was cross tabulated with gender, no significant gender differences were found (Table 2). Similarly, t-test results displayed in Table 3 show that the genders did not significantly differ in their mixing frequency ($t = -1.081$, $p > 0.05$).

When binge drinking in the past month (yes versus no) was cross tabulated with a history of mixing, results showed that 53% of binge drinkers had mixed alcohol with energy drinks, whereas only 35% of non-binge drinkers had, indicating that binge drinkers are statistically more likely to mix than non-binge drinkers are (see Table 4). Conversely, when a history of mixing (yes versus no) was cross tabulated with binge drinking in the past month, 77% of mixers qualified as binge drinkers, whereas only 61% of non-mixers did, indicating that mixers are statistically more likely to binge drink than non-mixers are (Table 5). T-test results were performed to investigate group differences between mixers and non-mixers. Mixers reported a significantly higher motivation to drink for the sake of getting drunk than non-mixers did ($t = 3.516$, $p < 0.01$). No statistically significant differences between the two groups were detected for the degree to which they felt risk-related behavioral states when they consumed (feeling in control, daring, aggressive, sexually uninhibited). Mixers did, however, report significantly more life interference as a result of their drinking than non-mixers did ($t = 2.866$, $p < 0.01$). See Table 6 for a summary of these results.

Table 2. Summary of crosstab analysis for *history of mixing* with *gender*

GENDER			
	MALE	FEMALE	TOTAL
YES MIX ENERGY COUNT	23		
EXPECTED COUNT	24.3	75	98
ADJUSTED RESIDUAL	-.4	73.7	98.0
		.4	
NO MIX ENERGY COUNT	28	80	108
EXPECTED COUNT	26.7	81.3	108.0
ADJUSTED RESIDUAL	.4	-.4	
TOTAL COUNT	51	155	206
EXPECTED COUNT	51.0	155.0	206.0

Adjusted Residuals are $< |1.3|$, therefore the association between mixing energy (yes versus no) and gender (male versus female) is not statistically significant.

Table 3. Summary of t-test results for mixing frequency between genders

GROUP STATISTICS				
	N	MEAN	STD. DEVIATION	STD. ERROR MEAN
MALES BINGE PAST MONTH	43	3.58	3.81	.580
FEMALES BINGE PAST MONTH	147	2.15	2.43	.201

INDEPENDENT SAMPLES TEST

	t	df	SIG. (2-TAILED)	MEAN DIFFERENCE
MIX ENERGY	-1.08	98.2	.282	-3.92

$p < .05$, therefore significant.

Table 4. Summary of crosstab analysis for binge drinking past month with history of mixing

GENDER			
	MALE	FEMALE	TOTAL
YES BINGE COUNT	78	68	146
EXPECTED COUNT	69.6	76.4	146.0
ADJUSTED RESIDUAL	2.5	-2.5	
NO BINGE COUNT	23	43	66
EXPECTED COUNT	31.4	34.6	66.0
ADJUSTED RESIDUAL	-2.5	2.5	
TOTAL COUNT	101	111	212
EXPECTED COUNT	101.0	111.0	212.0

Adjusted Residuals are $> |1.3|$, therefore the association between binge drinking in past month (yes versus no) and a history of mixing (yes) is statistically significant.

Table 5. Summary of crosstab analysis for history of mixing with binge drinking past month

GENDER			
	MALE	FEMALE	TOTAL
YES MIX COUNT	78	23	101
EXPECTED COUNT	69.6	31.4	101.0
ADJUSTED RESIDUAL	2.5	-2.5	
NO MIX COUNT	68	43	111
EXPECTED COUNT	76.4	34.6	111.0
ADJUSTED RESIDUAL	-2.5	2.5	
TOTAL COUNT	146	66	212
EXPECTED COUNT	146.0	66.0	212.0

Adjusted Residuals are $> |1.3|$, therefore the association between a history of mixing (yes versus no) and a binge drinking in past month (yes) is statistically significant.

Table 6. Summary of t-test results for group differences between mixers and non-mixers

GROUP STATISTICS					
	MIX ENERGY	N	MEAN	STD. DEVIATION	STD. ERROR MEAN
DRINK TO GET DRUNK	YES NO	100 109	59.5 44.4	28.0 34.2	2.80 3.28
CONTROL	YES NO	100 107	47.9 47.6	21.5 21.5	2.15 2.08
DARING	YES NO	100 106	68.4 64.9	20.5 21.2	2.05 2.06
AGGRESSIVE	YES NO	97 103	55.0 53.8	18.7 21.0	1.90 2.07
SEXUALLY UNINHIBITED	YES NO	99 108	71.5 68.5	21.8 20.4	2.19 1.96
LIFE INTERFERENCE	YES NO	101 111	18.9 10.7	23.1 18.1	2.30 1.72

INDEPENDENT SAMPLES TEST

	t	df	SIG. (2-TAILED)	MEAN DIFFERENCE
DRINK TO GET DRUNK	3.52**	204.4	.001	15.16
CONTROL	.111	205	.912	.331
DARING	1.20	204	.230	3.50
AGGRESSIVE	.419	198	.675	1.18
SEXUALLY UNINHIBITED	1.00	205	.318	2.94
LIFE INTERFERENCE	2.87**	189.2	.005	8.23

** $p < .01$, therefore significant.

DISCUSSION

In support of our initial hypothesis, our study did not find significant gender differences in the proportions of binge drinkers as well as mixers within our sample of college students. Mixing frequency not significantly different across genders. We did unexpectedly find that males binge drink significantly more often than females; however, these gender analyses need to be interpreted with caution due to the fact that our definition of binge drinking was the same for both genders (the ingestion of five or more drinks in a row on one occasion). Because past research has shown that women get more intoxicated per gram of alcohol consumed, we likely underestimated female binge drinking

(4). This is certainly a limitation of our study, and future studies should make sure to take this gender specificity into account in their operationalization of binge drinking.

Second, in support of our hypothesis, our study found that binge drinkers would be more likely to mix than non-binge drinkers and that mixers would be more likely to binge drink than non-mixers. We expect that these contingencies can be attributed to the widely held (and false) assumption among college students that the stimulant effects of energy drinks counteract the depressant effects of alcohol, thereby minimizing alcohol-induced impairment (10, 11). Consequently, mixers are more likely to drink heavily, often to the point of bingeing. We suggest that this same rationale could explain our finding that mixers reported a significantly greater motivation to drink for the sake of getting drunk than non-mixers did. We conjecture that mixers use energy drinks as a means of counteracting the unpleasant depressant effects of alcohol intoxication, thereby allowing them to drink in larger quantities for longer periods of time.

Our most surprising finding was the lack of significant differences between mixers and non-mixers on any of the risk-related feelings associated with drinking (feeling in control, daring, aggressive, sexually uninhibited). We had hypothesized that mixers would feel less prone to risk-related behavioural states when they drink due to caffeine's counteracting effect on perceptions of impairment. However, our lack of significant findings could be attributed to how our survey only asked students how they feel when they drink alcohol and not additionally how they feel when they mix. Future studies should investigate differences in students' expectations for when they drink alcohol alone versus in conjunction with energy drinks, as this might reveal more reasons why students are motivated to mix.

We also found that mixers reported significantly more life interference associated with their drinking, supporting another of our hypotheses. This result corroborates past research suggesting that the combination of alcohol and energy drinks, as opposed to alcohol alone, increases alcohol's abuse liability and may lead to more detrimental risk-taking behaviour (6).

In addition to the aforementioned limitation concerning our lack of a gender-specific measure of binge drinking, our study has other limitations that warrant attention. First, our sample size was relatively small ($N = 221$), which of course limits the application of our results in a broader context. Moreover, our sample consisted of three times more females than males, and this female overrepresentation is not representative of the typical college student population. Third, our sample of students came from a single psychology course which makes it, again, not representative of the general college population. Finally, we qualified students with a history of mix-

ing alcohol and energy drinks as "mixers" regardless of whether they had only mixed once or regularly. The same rule applied to our qualification of "binge drinkers." Perhaps surveying the same participants repeatedly over a set period of time (i.e., a longitudinal approach), rather than our method of surveying participants at only one point in time (i.e., a cross-sectional approach), could be used to qualify students as "mixers" or "binge drinkers" while accounting for the frequency of these respective behaviours.

Despite its limitations, our study is nonetheless the first of its kind to investigate the consumption of caffeinated alcoholic drinks and its association with binge drinking among college students at a Canadian university. The concurrent ingestion of energy drinks and alcohol is particularly dangerous because users lose the ability to accurately assess their level of intoxication, thus encouraging them to drink alcohol in larger quantities, often to the point of bingeing. This impairment, in turn, increases their potential for engaging in risky behaviours. Thus, knowledge about the effects of the interaction between alcohol and energy drinks is relevant to preventative programs aimed at reducing high-risk alcohol consumption and alcohol-related injuries resulting from car accidents, assaults and other high risk behaviour. More conclusive research in this area might also have implications for warranted policy measures, such as requiring that energy drinks carry a warning label concerning the danger of consuming these beverages with alcohol.

REFERENCES

1. H. Wechsler *et al.* *J. Am. Coll. Health* **50**, 203-217 (2002).
2. H. Wechsler, S.B. Austin, *J. Stud. Alcohol* **59**, 122-123 (1998).
3. H. Wechsler, A. Davenport, G. Dowdall, B. Moeykens, S. Castillo, *J. Am. Med. Assoc.* **272**, 1672-1677 (1994).
4. H. Wechsler, G. Dowdall, A. Davenport, E. Rimm, *Am. J. Public Health* **47**, 57-68 (1994).
5. C. Emslie, H. Lewars, G.D. Batty, K. Hunt, *Public Health* **123**, 12-14 (2009).
6. M.C. O'Brien, T.P. McCoy, S.D. Rhodes, A. Wagoner, M. Wolfson, *Acad. Emerg. Med.* **15**, 453-460 (2008).
7. C.J. Reissig, E.C. Strain, R.R. Griffiths, *Drug Alcohol Depend.* **99**, 1-10 (2009).
8. B.M. Malinauskas, V.G. Aeby, R.F. Overton, T. Carpenter-Aeby, K. Barber-Heidal, *Nutrition J.* **6**, 1-7 (2007).
9. A. Oteri, F. Salvo, A.P. Caputi, G. Calapai G, *Alcohol Clin. Exp. Res.* **31**, 1677-1680 (2007).
10. S.E. Ferreira, M.T. de Mello, S. Pompeia, M.L. de Souza-Formigoni, *Alcohol Clin. Exp. Res.* **30**, 598-605 (2006).
11. M.T. Fillmore, E.L. Roach, J.T. Rice, *J. Stud. Alcohol* **63**, 745-754 (2002).
12. B. Borsari, P. Muellerlaile, *Alcohol Clin. Exp. Res.* **33**, 826-838 (2009).
13. A. Bond, M. Lader, *Br. J. Med. Psychol.* **47**, 211-218 (1974).
14. M.E. Wewer, N.K. Lowe, *Res. Nurs. Health* **13**, 227-236 (1990).

Epigenetic modifiers enhance Vesicular Stomatitis Virus-mediated oncolysis in the refractory PC3 cell line

Marnie Goodwin Wilson^{1, 2}, Thi Lien-Anh Nguyen², Laura Shulak², Peyman Nakhaei^{1, 2} and John Hiscott^{1, 2}

¹Department of Microbiology and Immunology, McGill University, Duff Medical Building, 3775 University Street, Montreal, Quebec, Canada, H3A 2B4

²Lady Davis Institute for Medical Research, Sir Mortimer B. Davis - Jewish General Hospital, 3755 chemin Côte Ste Catherine, Montréal, Québec, Canada, H3T 1E2.

ABSTRACT

Introduction: Vesicular Stomatitis Virus (VSV) is an oncolytic virus that preferentially replicates in and kills cancerous cells. However, many cancer cell lines are resistant to VSV treatment alone. Previous work has shown that treating cancerous cells with histone deacetylase inhibitors makes them more susceptible to VSV infection and oncolysis. We hypothesize that treatment with a histone deacetylase inhibitor, Suberoylanilide hydroxamic acid (SAHA or Voronistat), and a methyltransferase inhibitor, 5-aza-2'-deoxycytidine (5-AZA or Decitabine), will result in an increase in VSV replication and virus-induced oncolysis *in vitro*. **Methods:** PC3 prostate cancer cells were treated with 1 μ M SAHA, 1 μ M 5-AZA or both. Of these samples, half were infected with oncolytic Vesicular Stomatitis Virus expressing green fluorescent protein VSV AV1 – GFP at a multiplicity of infection of 1×10^{-2} , 24 hours after treatment. Cells were then collected and subjected to either FACS analysis or protein extraction at 12, 24, 48 and 72 hours post-infection. We confirmed increases in cell death by western blotting for cleavage of Poly A Riboprotein, an important downstream effector of the Caspase pathway, as well as Caspases 8 and 9, hallmarks for the extrinsic and intrinsic apoptotic pathways respectively. **Results:** Treatment with SAHA, 5-AZA or a combination of both resulted in increases in VSV replication and cell death. These observations were consistent over four time points spanning 72 hours. **Discussion:** Treatment with histone deacetylase inhibitor/methyltransferase inhibitor combination increases VSV replication and cell death in tumour cell lines resistant to VSV infection. In combination with previous work, this data suggests that modulation of the antiviral response and apoptotic pathways increases susceptibility to VSV.

KEYWORDS

Epigenetics, Cellular Transformation, Oncolytic Virus, Apoptosis

*Corresponding author:

marnie.gwilson@gmail.com

Received: 10 January 2010

Revised: 16 March 2010

INTRODUCTION

Cancer is an extremely prevalent disease, causing approximately 500 000 deaths and nearly 1.5 million new cases annually in the United States (16). Many current cancer therapies lack efficacy, and can even induce therapeutic resistance in cancer cells (19). Further, since current cancer treatments often have low specificity for cancerous cells, they are often toxic and highly detrimental to the health of the patient (17).

Transformation occurs when a cell acquires a cancerous or malignant phenotype, characterized by uncontrolled cell proliferation (4). Clinical manifestations of cancer result if the body does not recognize and eliminate these cells. Oncolytic viral (OV) therapy uses non-pathogenic, replication-competent viruses selected or engineered to grow in and destroy tumour cells (5). During the evolution of malignancies, genetic abnormalities accumulate and provide cancer cells with growth and survival advantages, but compromise host antiviral defences (20). Most prominently, the interferon system, which is responsible for cell-cell communication during infection, is down-regulated or absent in many transformed cells (23, 34). Although the interferon pathway is most commonly associated with defence against infection, it has also been shown to play a role in cancer immunology (28, 34, 37). Infected cells secrete interferon molecules, which bind to receptors on neighbouring cells and trigger the production of molecules that protect against further virus infection (14, 18).

Vesicular Stomatitis Virus (VSV) is a negative-stranded RNA virus and a well-characterized oncolytic virus (4, 5). It replicates preferentially in cells that have acquired defects of the interferon pathway. In normal cells, interferon is produced, which protects surrounding cells from VSV infection, resulting in rapid clearance of the virus and recovery (23). Conversely, transformed cells are unable to mount a response against the mutated virus and are killed (2). This results in selective replication in transformed cells, increasing the specificity of the treatment and decreasing the potential for adverse side effects, illness or systemic infection (13). Side effects due to oncolytic virus treatment are generally limited to flu-like symptoms, a vast improvement over the side effects of current chemotherapies (1, 3). Unfortunately, many transformed cell lines, including most primary tumours, are resistant to VSV-mediated oncolysis (35). Resistance often occurs when cell lines have not lost their ability to mount an interferon response. Several studies have combined OVs with other cancer therapeutics to combat problems related to tumour cell resistance (6, 11, 12, 15, 28, 38, 39). Small molecule inhibitors of various cellular processes are candidates for such combinations.

Histone deacetylase inhibitors are one such candidate (7). Epigenetic alterations of chromatin, the scaffold of histone proteins that bind DNA in the nucleus result in abnormal gene expression of cancer cells (25). Acetylation occurs on lysine residues of histone tails and thereby alters their electrostatic interactions with DNA (26). Acetylation and deacetylation of histones is a dynamic and tightly regulated process, resulting in transcriptional control and alterations in gene expression (25, 31). Acetylation is mediated by protein histone acetyltransferases (HATs) and is generally associated with chromatin decondensation and gene expression. Meanwhile, histone deacetylation, which is mediated by histone deacetylases (HDACs), results in chromatin conden-

sation and silencing of gene expression (27). Epigenetic modifications also play an important role in cell division, both through the modulation of gene products involved in the progression of the cell cycle and because near-complete histone deacetylation and condensation of chromatin are required to complete mitosis (7). In transformed cells, histone modifications are often dysregulated, resulting in aberrant transcription of genes and the loss of cell cycle control (26, 30). HDI treatment has been repeatedly shown to blunt the cellular antiviral response, which in turn makes OV treatment more effective (29, 30).

Methyltransferase inhibitors (MTIs) are another epigenetic-based cancer therapeutic (10). Methylation of gene promoters is a common means of gene silencing, and is used in the methylation of certain tumour suppressors, such as p53 and proapoptotic and anti-metastatic genes (22, 36). Unlike acetylation, which affects the histone scaffold, DNA methylation transfers a methyl group directly to the 5' position of specific cytosine residues in DNA (10, 24). Most MTIs do not directly inhibit the methyltransferase enzyme; rather, they are derivatives of cytosine with different chemical groups (for instance, a nitrogen-based group) substituted in the 5' position (10). These cytosine derivatives intercalate into the DNA of rapidly dividing cells, thus altering the target for methyltransferase and inhibiting its activity (10). The requirement that cells be rapidly dividing is the basis for the tumour-selective mechanism of MTI therapy (24). MTI treatment is often used in combination with HDI treatment in preclinical experiments as well as clinical trials (32, 33). The two have been shown to produce a synergistic effect both *in vitro* and *in vivo*.

HDIs and MTIs have been shown to act synergistically in a number of ways, indicating that their combined effect could further sensitize transformed cells to VSV-mediated oncolysis. This project investigates whether the addition of MTIs to the established combination of VSV and HDIs can further enhance the therapeutic benefits of OV use in refractory cell lines.

METHODS

VIRUS

VSV Δ 51 expressing Green Fluorescent Protein (GFP) is a recombinant derivative of VSV Δ 51, a naturally occurring interferon (IFN) inducing mutant of the VSV Indiana serotype. Viruses were propagated and purified, as described in (35), in Vero cells.

CELL TREATMENT AND INFECTION

PC3 prostate cancer cells were plated at a 1:4 dilution and left overnight in RPMI media (Wisent) supplemented with 10% foetal bovine serum (FBS) and 1% Penicillin/ Streptomycin mixture. Cells were then either left untreated or treated with

1 μM concentrations of either the histone deacetylase inhibitor suberoylanilide hydroxamic acid (Vorinostat, denoted SAHA), the methyltransferase inhibitor 5-aza-2'-deoxycytidine (Decitabine, denoted 5-AZA), or both. Of these samples, half were infected with VSV AV1 – GFP at a multiplicity of infection (MOI) of 1×10^{-2} 24 hours after treatment. Cells were then collected for flow cytometry (FACS) analysis, protein extraction or RNA extraction at 12, 24, 48 and 72 hours post-infection. Cells were either immediately used (in the case of FACS analysis) or kept at -80°C until needed (in the case of protein extraction).

FLOW CYTOMETRY

Cells were washed once with PBS, then trypsinized in 0.25% trypsin (Wisent), diluted to 1:4 in PBS and centrifuged at 1200 rpm for five minutes. Supernatant was discarded and cells were stained with Annexin-V APC (BD Biosciences) as per the manufacturer's instructions. Cells were subjected to FACS analysis (10^5 events per measurement) on a FACS Calibur (Beckton-Dickson) and analyzed using FCS express V3 Software. FACS analysis showed expression of GFP (indicative of viral replication) and the binding of Annexin-V (indicative of cell death) for each sample.

PROTEIN EXTRACTION AND WESTERN BLOTTING

Cells were treated with protease inhibitor cocktail (Sigma Aldrich) and lysed using Triton-X lysis buffer. Protein samples were stored at -20°C until needed. Samples were run on 14% polyacrylamide gels, transferred to nitrocellulose membranes, blocked for one hour with milk and stained with antibodies to PARP, Caspase-3, Caspase-9 and Caspase-8, as well as VSV and actin (all from Cell Signaling Technology).

RESULTS

ENHANCEMENT OF VSV REPLICATION AND ONCOLYSIS IN PRETREATED CELLS

Treated and infected cells were harvested and analyzed by FACS at 24 and 48 hours post-infection. A GFP-expressing virus was used to indicate virus replication while Annexin-V staining was used to indicate cell death. An increase in viral replication (most prominent at 24 hours post-infection) and cell death (most prominent at 48 hours post-infection) was observed when cells were pre-treated with both HDI SAHA and MTI 5-AZA.

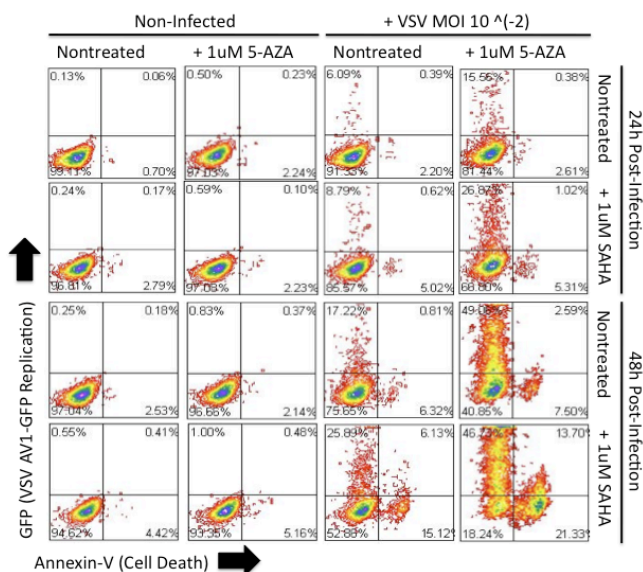


Fig. 1. Use of SAHA/5-AZA combination treatment results in increased VSV replication and cell death. FACS analysis showed viral replication (indicated by GFP) and cell death (indicated by Annexin-V) at 24 and 48 hours after VSV infection under various treatment conditions. Increases in both VSV replication and cell death in cells subjected to both treatments were observed.

CONSISTENT INCREASES IN VIRUS REPLICATION AND CELL DEATH

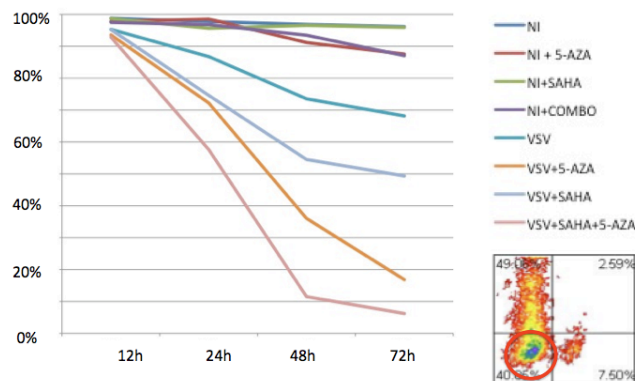


Fig. 2. Decreases in uninfected, viable cell populations are seen after combination treatment. Percentages of uninfected, viable cells were determined using FACS analysis. Marked decreases in this population are observed when both treatments are used (VSV+SAHA+5-AZA), while single treatments also enhance VSV replication and cell death. Treatment with SAHA, 5-AZA or the combination without VSV infection results in only a small decrease in viability.

Proportions of non-treated, non-infected cells were determined via FACS analysis by taking percentages from the bottom left quadrant, as indicated (no Annexin-V binding or GFP expression), at 12, 24, 48 and 72 hours after VSV infection. Amounts

of viable uninfected cells decreased when cells were treated with either 5-AZA or SAHA, while a more marked decrease resulted from treatment by both compounds together. Treatment with either SAHA, 5-AZA or the combination without VSV infection resulted in little cell death, indicating that increased activity was due to an increase in VSV replication and virally-induced oncolysis.

INCREASES DEMONSTRATED BY WESTERN BLOTTING
Increases in the VSV component proteins Polymerase, G Glycoprotein and Phosphoprotein/Nucleoprotein were seen after treatment. The most marked increase was seen in cells subjected to both treatments, while cells treated with either only Decitabine or only SAHA also showed increased virus replication. This pattern was reproducible both 24 and 48 hours following virus infection.

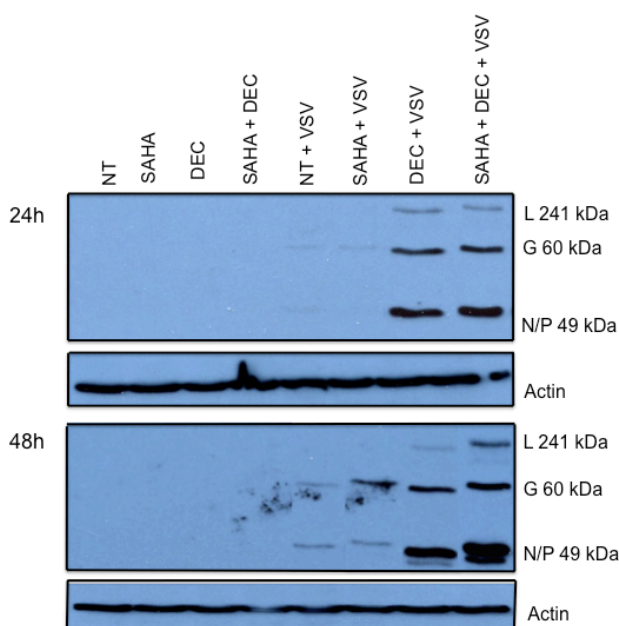


Fig. 3. VSV replication is increased following single treatment of either SAHA or 5-AZA. Notably, a more marked increase was observed following treatment with both inhibitors. These patterns of changes in VSV replication were consistent at 24 and 48 hours post-infection.

WESTERN BLOTTING DEMONSTRATES INCREASED CASPASE ACTIVITY IN TREATED CELLS

Western blotting showed an increase in the cleaved forms of Caspases 3 and 9 following HDI and MTI treatment. Meanwhile, we noted a slight upregulation of Caspase 8 as a result of VSV infection. This upregulation appeared unaffected by pre-treatment with SAHA, 5-AZA or a combination thereof. This is consistent with previous data in the field, which has shown that HDIs and MTIs induce apoptosis by the intrinsic apoptotic

pathway without affecting the extrinsic apoptotic pathway (8, 9, 10). Meanwhile, VSV induces apoptosis via both pathways (21). Western blotting also showed an increase in VSV replication.

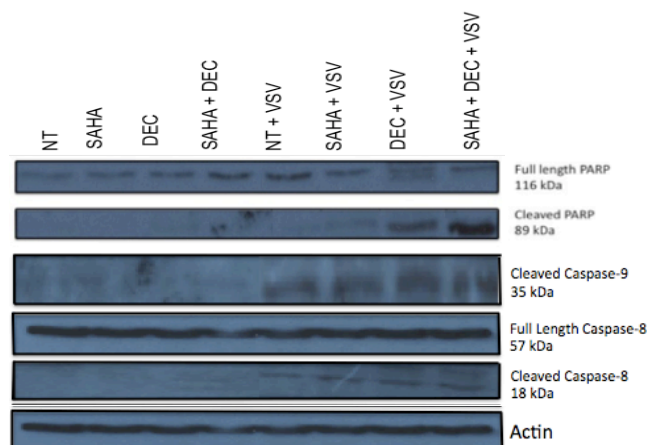


Fig. 4. Treatment with SAHA and 5-AZA at 48 hours post-infection increases activity of the intrinsic apoptotic pathway, but not the extrinsic pathway. Cleavage of Caspase-9, a hallmark of the intrinsic apoptotic pathway, is increased when cells are pre-treated with SAHA or 5-AZA, and shows a more marked increase in the case of double treatment. Meanwhile, these treatments do not affect the activity of Caspase-8, a hallmark of extrinsic apoptosis.

DISCUSSION

The PC3 cell line is generally considered to be resistant to VSV-mediated oncolysis. As such, this cell line is a valuable tool for the study of treatments to enhance virus replication in resistant cell lines. The antiviral response of this cell line is well documented, aiding the detection of variances resulting from pre-treatment. This cell line could therefore prove useful in future research to assess the potential utility of OV combination treatment.

Previous experiments have assessed the utility of VSV/HDI combination in PC3 cells. In untreated cells infected with VSV, a number of gene products relating to the IFN cascade were induced. Treatment with HDIs blunted the induction of this response (28). As expected, a down-regulation of the antiviral response was accompanied by a dramatic increase in VSV replication and oncolysis. PC3 prostate cancer cells, which are normally minimally sensitive to VSV oncolysis, were quickly killed by VSV replication when infected in the presence of HDIs (28). Little to no VSV replication and almost no cell death was observed in normal cells or in infected PC3 cells that had not undergone HDI treatment (28). This effect was also observed in mouse models. VSV replicated rapidly and showed enhanced therapeutic benefit in mice treated with HDIs.

FACS ANALYSIS SHOWS INCREASES IN VSV REPLICATION AND CELL DEATH IN TREATED CELLS.

VSV replication was assessed using FACS analysis. A dramatic increase in viral replication can be seen at 24 hours after infection in cells treated with both SAHA and 5-AZA (Fig. 1). A similarly dramatic increase in Annexin-V positive cells (indicative of cell death) is seen at 48 hours after infection (Fig. 1). This indicates some modulation of the host-cell mechanisms that increase susceptibility to VSV infection. Importantly, VSV infection alone resulted in very little virus replication, which confirms the PC3 cell line's high level of resistance to OV treatment. Treating with SAHA, 5-AZA or the HDI/MTI combination without VSV infection also resulted in very little cell death.

TREATMENT RESULTS IN CONSISTENT INCREASE IN VSV REPLICATION AND CELL DEATH OVER 72 HOURS

The proportions of uninfected, viable cells at 12, 24, 48 and 72 hours post-infection were determined using FACS analysis (Fig. 2). A steady decline in viability was observed when infected cells were subjected to pretreatment by both 5-AZA and SAHA. A less prominent decline was visible when cells were subjected to only one type of pretreatment. Very little decline was seen in untreated or uninfected cells. Statistical analysis is required to determine whether these results indicate an additive or synergistic effect. These changes in the replication of VSV were consistent with data obtained by western blot (Fig. 3).

ENHANCED ACTIVITY IN THE INTRINSIC APOPTOTIC PATHWAY INCREASES CELL DEATH

Increases in cell death were further investigated using western blotting for components of the Caspase pathway. An increase in the cleavage of Poly-ADP Ribose Polymerase (PARP), a cellular protein that assists in the repair of DNA cleavage, was observed (Fig. 3). Cleavage of PARP results in an arrest in DNA repair, the depletion of ATP, and ultimately cell death. Treatment also resulted in an increase in the cleavage of Caspase-9, indicating an increase in the activity of the intrinsic apoptotic pathway (Fig. 3). This is consistent with past results, which indicate that HDI and MTI treatment both act via this intrinsic pathway alone (8, 9, 10). No increase in Caspase-8 was seen, which indicates that the extrinsic pathway is unaffected by these treatments. VSV and actin were observed as controls. An increase in VSV replication similar to that seen using FACS analysis was detected by western blotting. Actin expression remained consistent, an indication of similar protein loading concentrations.

Several interesting avenues exist for further research. Previous results from our laboratory indicate that treatment with HDIs regulates components of the IFN response, including the adaptor molecule RIG-I, the cytokines IFN α and IFN β , the intracellular messenger protein IRF7, ISG56 (induced by interferon signal-

ing and having antiviral activity) and MxA (a GTPase directly involved in the inhibition of VSV replication). However, how these components will respond to low-dose SAHA treatment or to the SAHA/5-AZA combination is not yet known. Since the doses of both treatments used in this study are significantly lower than most previously reported, it is reasonable to postulate that there will be some modification of the effects of treatment on cellular processes. RT-PCR will be used to demonstrate changes in RNA levels of various proteins that mediate interferon response. Although *in vitro* studies have shown promising potential therapeutic benefits of this treatment, the use of animal models is an essential step in the evaluation of potential cancer therapeutics. Experiments evaluating the efficacy of these treatments in immunocompetent tumour xenograft animal models are currently underway.

Oncolytic viruses provide a novel approach to cancer therapy and may greatly improve patient care. There is already evidence that epigenetic therapeutics, including HDIs, may increase susceptibility to VSV treatment. The results of this study indicate that treatment with MTIs alone, or in combination with HDIs, can also increase susceptibility to VSV infection, virus-induced oncolysis and cell death.

REFERENCES

1. S. Balachandran, G. Barber, *IUBMB life* **50**, 135-138 (2000).
2. S. Balachandran, G. Barber, *Cancer Cell* **5**, 51-65 (2004).
3. S. Balachandran, M. Porosnicu, G. Barber, *J. Virol.* **75**, 3474 (2001).
4. G. Barber, *Oncogene* **24**, 7710-7719 (2005).
5. J. Bell, B. Lichty, D. Stojdl, *Cancer Cell* **4**, 7-11 (2003).
6. A. Bieler, K. Mantwill, T. Dravits, A. Bernshausen, G. Glockzin, N. K'bler-Vargas, H. Lage, B. Gansbacher, P. Holm, *Hum. Gene. Ther.* **17**, 55-70 (2006).
7. M. Dokmanovic, C. Clarke, P. Marks, *Mol. Cancer Res.* **5**, 981 (2007).
8. H. Duan, C. Heckman, L. Boxer, *Mol. Cell Biol.* **25**, 1608 (2005).
9. F. Facchetti, S. Previdi, M. Ballarini, S. Minucci, P. Perego, C. Porta, *Apoptosis* **9**, 573-582 (2004).
10. J. Goffin, E. Eisenhauer, *Ann. Oncol.* **13**, 1699 (2002).
11. M. Goldsmith, A. Aguila, K. Steadman, A. Martinez, S. Steinberg, M. Alley, W. Waud, S. Bates, T. Fojo, *Mol. Cancer Ther.* **6**, 496 (2007).
12. M. Goldsmith, M. Kitazono, P. Fok, T. Aikou, S. Bates, T. Fojo, *Clin. Cancer Res.* **9**, 5394 (2003).
13. J. Heiber, J. Hyun, M. Obuchi, G. Barber, *Cytokine* **48**, 47-47 (2009).
14. J. Hiscott, *Cyto. Growth Fact. Rev.* **18**, 483-490 (2007).
15. N. Hoti, W. Chowdhury, J. Hsieh, M. Sachs, S. Lupold, R. Rodriguez, *Mol. Therapy* **14**, 768-778 (2006).
16. A. Jemal, R. Siegel, E. Ward, Y. Hao, J. Xu, T. Murray, M. Thun, *CA: a cancer journal for clinicians* **58**, 71 (2008).
17. D. Kalvakolanu, S. Balachandran, P. Roberts, L. Brown, H. Truong, A.

- Pattnaik, D. Archer, G. Barber, *Trends Microbiol.* **7**, 166-171 (1999).
18. T. Kawai, S. Akira, *Nature Immunol.* **7**, 131-137 (2006).
19. P. La Rosee, K. Johnson, A. Corbin, E. Stoffregen, E. Moseson, S. Willis, M. Mauro, J. Melo, M. Deininger, B. Druker, *Blood* **103**, 208 (2004).
20. G. Lagger, A. Doetzlhofer, B. Schuettengruber, E. Haidweiger, E. Simboeck, J. Tischler, S. Chiocca, G. Suske, H. Rotheneder, E. Wintersberger, *Mol. Cell. Biol.* **23**, 2669 (2003).
21. C. Lallemand, B. Blanchard, M. Palmieri, P. Lebon, E. May, M. Tovey, *Oncogene* **26**, 328-338 (2006).
22. D. Lavelle, J. Desimone, M. Hankewych, T. Kousnetzova, Y. Chen, *Leukemia Res.* **27**, 999-1007 (2003).
23. B. Lichty, A. Power, D. Stojdl, J. Bell, *Trends. Mol. Med.* **10**, 210-216 (2004).
24. F. Lyko, R. Brown, *JNCI* **97**, 1498 (2005).
25. P. Marks, X. Jiang, *Cell Cycle* **4**, 549 (2005).
26. P. Marks, V. Richon, R. Rifkind, *JNCI* **92**, 1210 (2000).
27. S. Minucci, P. Pelicci, *Nat. Rev. Cancer* **6**, 38-51 (2006).
28. T. Nguyen, H. Abdelbary, M. Arguello, C. Breitbach, S. Leveille, J. Diallo, A. Yasmeeen, T. Bismar, D. Kirn, T. Falls, *Proc. Natl. Acad. Sci.* **105**, 14981 (2008).
29. I. Nusinzon, C. Horvath, *Proc. Natl. Acad. Sci.* **100**, 14742 (2003).
30. A. Otsuki, A. Patel, K. Kasai, M. Suzuki, K. Kurozumi, E. Chiocca, Y. Saeki, *Mol. Ther.* **16**, 1546-1555 (2008).
31. M. Peart, G. Smyth, R. Van Laar, D. Bowtell, V. Richon, P. Marks, A. Holloway, R. Johnstone, *Proc. Natl. Acad. Sci.* **102**, 3697 (2005).
32. S. Shaker, M. Bernstein, L. Momparler, R. Momparler, *Leukemia Res.* **27**, 437-444 (2003).
33. A. Soriano, H. Yang, S. Faderl, Z. Estrov, F. Giles, F. Ravandi, J. Cortes, W. Wierda, S. Ouzounian, A. Quezada, *Blood* **110**, 2302 (2007).
34. D. Stojdl, B. Lichty, S. Knowles, R. Marius, H. Atkins, N. Sonenberg, J. Bell, *Nature Medicine* **6**, 821-825 (2000).
35. D. Stojdl, B. Lichty, B. Tenover, J. Paterson, A. Power, S. Knowles, R. Marius, J. Reynard, L. Poliquin, H. Atkins, *Cancer Cell* **4**, 263-275 (2003).
36. S. Suh, H. Pyun, J. Cho, W. Baek, J. Park, T. Kwon, J. Park, M. Suh, D. Carson, *Cancer letters* **160**, 81-88 (2000).
37. V. Tumilasci, S. Olieri, T. Nguyen, A. Shamy, J. Bell, J. Hiscott, *J. Virol.* **82**, 8487 (2008).
38. R. Vanoosten, J. Earel, T. Griffith, *Apoptosis* **12**, 561-571 (2007).
39. T. Watanabe, M. Hioki, T. Fujiwara, M. Nishizaki, S. Kagawa, M. Taki, H. Kishimoto, Y. Endo, Y. Urata, N. Tanaka, *Exp. Cell. Res.* **312**, 256-265 (2006).

Re-tuning the Walker-Kasting global carbon cycle box model using a parameter sensitivity analysis

Simon Yang^{*1}, David A. Carozza¹, Lawrence A. Mysak¹

¹Department of Atmospheric and Oceanic Sciences, McGill University, Burnside Hall, 805 Sherbrooke Street West, Montreal, Quebec, Canada, H3A 2K6

ABSTRACT

Introduction: The Walker-Kasting global carbon cycle box model is a simple representation of the Earth system used to study climatic events. This model has a high number of parameters whose sensitivity must be tested in order to better understand which of them dominate the behaviour of the model. In this study, we perform a parameter sensitivity analysis. Moreover, we use these results to re-tune the model to preindustrial conditions using a quantitative criterion. We then compare our results to those determined by Walker-Kasting. **Methods:** We achieved the parameter sensitivity analysis by calculating, for each parameter, an index that measures the impact of a change in the initial parameter value on the equilibrium solutions. The most sensitive parameters were determined and then tuned in the model by comparing the model equilibrium solutions to a set of 32 experimental values. **Results:** We found that nine of the tuning parameters were sensitive to a change to their initial value. Furthermore, we discovered that 5 of these parameter values were identical to those determined by Walker-Kasting, thus affirming their work. **Discussion:** A sensitivity analysis is interesting to perform because it allows the users of a model to more fully comprehend the way in which the model reacts to changes in its parameters. Sensitivity analysis is fundamental in the tuning of a model (for example, to a particular period in the Earth's history) since it allows researchers to consider only the most important parameters.

KEYWORDS

Walker-Kasting, Box model, Parameter sensitivity analysis

*Corresponding author:

simon.yang@mail.mcgill.ca

Received: 11 January 2010

Revised: 17 March 2010

INTRODUCTION

A box model is a simplified version of a complex system such that the components of the system are reduced to linked boxes (or reservoirs). Models of this type are employed to simulate processes in the climate system in a rudimentary way, and are used to determine whether model output satisfactorily describes an observed phenomenon. Because they are simple in structure and computationally efficient, box models are ideal for analyzing climate processes that occur on long time scales. In particular, a box model of the Earth system depicts the components of the Earth system (atmosphere, ocean, terrestrial biosphere, etc.) as boxes that are linked by exchanges of mass, energy or both.

In general, box models possess a large number of parameters that must be tuned with respect to a set of experimental data. This is the case because box models are not inherently based on

physical laws, but on parameterizations of those laws. Researchers perform such a tuning procedure by determining the set of model parameter values that generates the best equilibrium results (steady state solutions) in terms of a specific criterion, such as minimizing the root mean squared error between the model and experimental results.

An important element in the development of a box model is therefore the determination of which parameters have the greatest impact on the model equilibrium results. Such a procedure must be undertaken since it is computationally unfeasible to run a model, even a computationally simple one, for all values of the parameter space. Therefore, it is interesting to know which parameters are the most sensitive since it shows which parameters need to be considered with greater accuracy and which parameters can be ignored in the tuning process.

In this study, we perform the first sensitivity analysis for the Walker-Kasting (1) box model (denoted WK92) and thus determine the most influential model parameters. These results allow us to tune the model to preindustrial conditions using a quantitative criterion. Furthermore, we compare our tuning results to those of the qualitative approach used by WK92, and discuss applications of our sensitivity analysis.

METHODS

MODEL

The preindustrial global carbon cycle is the biogeochemical cycle that comprises both: i) the carbon stored within different reservoirs of the Earth system and ii) the exchange of carbon between these components. The WK92 box model is a simple representation of the preindustrial global carbon cycle, which consists of eight model reservoirs: atmosphere, terrestrial biomass, cold surface ocean, warm surface ocean, thermocline, Deep Atlantic Ocean, Deep Indian Ocean and Deep Pacific Ocean (Fig. 1).

The model is governed by 32 ordinary differential equations that represent thermohaline (temperature and salinity) fluxes and mixing fluxes of carbon and nutrients between the reservoirs, as well as biogeochemical processes such as photosynthesis, respiration and the oceanic biological pump, which are biological processes that transport carbon from the ocean surface to the deep ocean. For each reservoir, the model calculations include: atmospheric CO_2 concentration, lysocline depth (the ocean depth below which the rate of dissolution of calcium carbonate increases dramatically), average surface air temperature and $\delta^{13}\text{C}$ for each reservoir. Table 1 lists the prognostic variables. Note that $\delta^{13}\text{C}$ is the ratio of the rarer ^{13}C isotope of carbon to the more common ^{12}C isotope, relative to a generally recognized standard ratio of

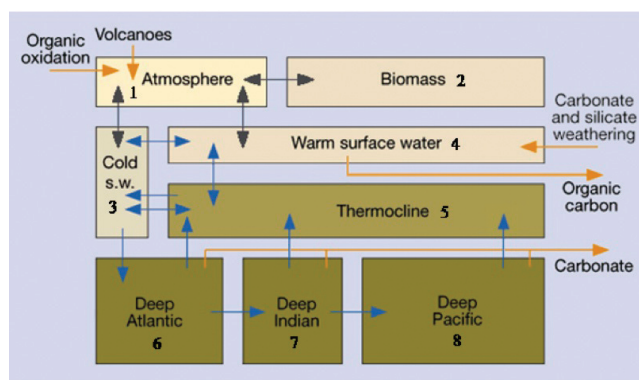


Fig. 1: Schematic of the WK92 model reservoirs (adapted from Dickens, 1999). Exchanges of carbon internal to the model are represented by blue and black arrows. Blue single- and double-headed arrows between the ocean reservoirs represent thermohaline and mixing fluxes, respectively. Black arrows between the atmosphere and biomass represent respiration and photosynthesis, whereas those between the atmosphere and ocean reservoirs represent diusive exchanges of carbon. Exchange fluxes external to the model are represented by orange arrows. Figure taken from Carozza (2009)

Table 1: Walker and Kasting (1992) model prognostic variables. PAL = preindustrial atmospheric level; 1 PAL = 280 ppmv. In the WK92 model, there are six equations for each of P, Σ , and A in the ocean reservoirs and one equation for each of T_S and $[\text{CO}_2]$. In addition, there is one equation for M_{Bio} , three equations for R in the deep ocean reservoirs and eight equations for $\delta^{13}\text{C}$. Note that this adds up to 32 equations.

Variable	Name	Chemical Representation	Unit
P	Dissolved phosphate	HPO_4^{2-}	mmol m^{-3}
Σ	Total dissolved carbon	$\text{HCO}_3^- + \text{CO}_3^{2-} + \text{H}_2\text{CO}_3$	mol m^{-3}
A	Alkalinity	$\text{HCO}_3^- + 2\text{CO}_3^{2-}$	mol m^{-3}
$[\text{CO}_2]$	Carbon dioxide	$\text{pCO}_{2(g)}$ or $\text{pCO}_{2(aq)}$	PAL
T_S	Surface temperature	-	K
M_{Bio}	Biomass	-	10^{18} mol C
R	Pelagic carbonates	-	10^{18} mol C
$\delta^{13}\text{C}$	$\delta^{13}\text{C}$	-	‰

the two. It is an important variable because a change indicates a flux of carbon into or out of the system in question. A list of the model parameters can be found in Table 2.

SENSITIVITY ANALYSIS

To calculate the sensitivity of the WK92 model parameters, we implemented the method described by Nordhaus (2). First, we determined an appropriate range for the model parameters under consideration. Each range was defined by a minimum and a maximum value (extreme values), and was determined based on a literature review of the specific parameter. We then compared the equilibrium results of the simulations with the extreme parameter values to the results with the initial parameter value by means of the following sensitivity index:

$$(1) \quad I_i = \sqrt{\frac{1}{n} \sum_t \left(\frac{X_i^M(t) - X_i^*}{X_i^*} \right)^2},$$

where $X_i^M(t)$ is the time series of the i^{th} model variable for the extreme parameter values, X_i^* is the time series of the i^{th} model variable for the initial parameter value, and n is the number of points in the time series. Note that the time series of the model variable i that is under investigation, $X_i^M(t)$, evolves in time until it reaches equilibrium and is thus a function of time. However, the time series of the model variable under the initial parameter value, X_i^* , is a constant function, since it begins at the equilibrium value. The sensitivity index therefore does not only measure the difference between the equilibrium values for the initial and extreme parameter values, but also the distance between the two time series.

The deviation is then normalized by dividing the difference $X_i^M(t) - X_i^*$ by X_i^* , so that the quantity in parentheses in Equation 1 is dimensionless. This normalization allows us to compare sensitivity indices for every parameter. The I values were then averaged to obtain an extreme sensitivity index I for each parameter. To take both the maximum and minimum parameter results into account, the two sensitivity indices are averaged. The initial, minimum and maximum values for each model parameter, the sensitivity indices and the averaged sensitivity index I are given in Table 3. The nine most sensitive parameters are presented in Figure 2.

Table 2: Model parameters and their description

Parameter	Description
f_{PT}	Fraction of particulate matter dissolved in the thermocline
R_{CP}	Ratio of particulate matter organic carbon to phosphorus
R_{CO}	Ratio of particulate matter CaCO_3 to organic carbon
z_1	Overall lysocline depth
z_2	Rate of change of lysocline with respect to $[\text{CO}_3^{2-}]$
C_{bio}	Initial biomass
a_T	Total surface area of surface ocean reservoirs
uv	Upwelling velocity in m/y
vmv	Vertical mixing velocity in m/y
$swmt$	Surface water mixing time in years
$tcmt$	Thermocline mixing time in years
α	Planetary albedo
f_{PD}	P_4 / P_8
P_R	Concentration of phosphate in river water
τ_{OA}	CO_2 dissolution time in years
M_{atm}	CO_2 mass in the atmosphere
τ_{Bio}	Forest growth and decay time in years
$sfcarb$	Reactive pelagic carbonate per square meter
a_3 / a_T	Fraction of cold surface ocean area to ocean area
C_{surf}	Earth's surface heat capacity
P_4	Phosphate in the warm surface ocean
P_8	Phosphate in the Deep Pacific

Table 3: Initial, minimum, and maximum parameter values and sensitivity index 1. The subscripts are the reservoir numbers (Fig. 1)

Parameter	Initial value	Test value	Sensitivity index I	Average
f_{PT}	0.925	0.950 0.900	0.165 0.092	0.128
R_{CP}	120.000	140.000 100.000	0.072 0.077	0.074
R_{CO}	0.090	0.200 0.030	0.382 0.670	0.526
z_1	5.800	6.300 5.300	0.033 0.029	0.031
z_2	50.000	60.000 40.000	0.020 0.032	0.026
C_{bio}	0.200	0.400 0.100	0.048 0.186	0.117
uv	1.150	1.380 0.920	0.032 0.046	0.028
vmv	10.500	12.600 8.400	0.034 0.043	0.039
$swmt$	50.000	60.000 40.000	0.011 0.015	0.013
$tcmt$	250.000	300.000 200.000	0.008 0.009	0.009
α	0.300	0.308 0.292	0.020 0.018	0.019
f_{PD}	0.040	0.048 0.032	0.019 0.019	0.019
P_R	0.001	0.001 0.001	0.024 0.014	0.019
τ_{OA}	10.000	12.000 8.000	0.001 0.001	0.001
M_{atm}	0.050	0.060 0.040	0.001 0.001	0.001
τ_{Bio}	50.000	60.000 40.000	0.000 0.000	0.000
$sfcarb$	0.0004	0.0008 0.0002	0.0000 0.0000	0.000
a_3/a_T	0.360	0.432 0.288	0.044 0.055	0.037
C_{surf}	50.300	60.360 40.240	0.000 0.000	0.000
$care afr$	0.003	0.005 0.001	0.000 0.000	0.000

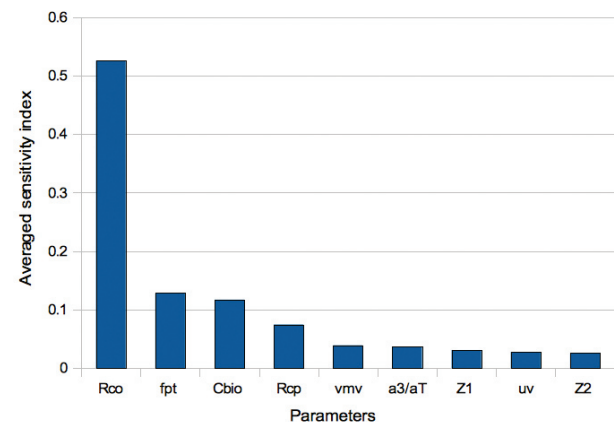


Fig. 2: Averaged sensitivity index I (see table 3) for the nine most sensitive model parameters, presented in decreasing order.

Table 4: Selected proxy values and their sources. The subscripts of the variables refer to a specific reservoir (see Fig.1) i.e., P_3 refers to phosphate in the cold surface water reservoir.

Variables	units	Range	selected value	source
P_3	$10^{-3}molm^{-3}$	0.7 - 1.0	0.85	Walker and Kasting (1992) fig.7 p.163
P_4	$10^{-3}molm^{-3}$	0.1 - 0.2	0.15	Walker and Kasting (1992) fig.7 p.163
P_5	$10^{-3}molm^{-3}$	0.2 - 2.5	1.5	WOCE (1990-1998) Atlas volume 4 : Indian Ocean
P_6	$10^{-3}molm^{-3}$	1.0 - 2.5	1.75	Walker and Kasting (1992) fig.7 p.163
P_7	$10^{-3}molm^{-3}$	2.3 - 2.5	2.4	WOCE (1990-1998) Atlas volume 4 : Indian Ocean
P_8	$10^{-3}molm^{-3}$	2.0 - 3.25	2.625	Walker and Kasting (1992) fig.7 p.163
Σ_3	$10^{-3}molm^{-3}$	2.14 - 2.23	2.185	Broecker and Peng (1982), fig.2-9 p.70
Σ_4	$10^{-3}molm^{-3}$	1.90 - 2.02	1.96	Broecker and Peng (1982), fig.2-9 p.70
Σ_5	$10^{-3}molm^{-3}$	2.0 - 2.3	2.15	WOCE (1990-1998) Atlas volume 4 : Indian Ocean
Σ_6	$10^{-3}molm^{-3}$	2.16 - 2.20	2.18	Broecker and Peng (1982), fig.2-9 p.70
Σ_7	$10^{-3}molm^{-3}$	2.34 - 2.40	2.37	Broecker and Peng (1982), fig.2-9 p.70
Σ_8	$10^{-3}molm^{-3}$	2.33 - 2.38	2.355	Broecker and Peng (1982), fig.2-9 p.70
A_3	$10^{-3}molm^{-3}$	2.36 - 2.40	2.38	Broecker and Peng (1982), fig.2-9 p.70
A_4	$10^{-3}molm^{-3}$	2.275 - 2.34	2.31	Broecker and Peng (1982), fig.2-9 p.70
A_5	$10^{-3}molm^{-3}$	2.3 - 2.35	2.325	WOCE (1990-1998) Atlas volume 4 : Indian Ocean
A_6	$10^{-3}molm^{-3}$	2.325 - 2.355	2.34	Broecker and Peng (1982), fig.2-9 p.70
A_7	$10^{-3}molm^{-3}$	2.375 - 2.39	2.382	Broecker and Peng (1982), fig.2-9 p.70
A_8	$10^{-3}molm^{-3}$	2.44 - 2.475	2.458	Broecker and Peng (1982), fig.2-9 p.70
M_{Bio}	mol C	-	0.2×10^{15}	Walker and Kasting (1992)
T_S	$^{\circ}C$	-	15.0	Walker and Kasting (1992)
pCO_2	ppmv	-	280	Walker and Kasting (1992)
$z_{9,6}$	km	-	4.0	Broecker and Peng (1982), fig.2-14 p.77
$z_{19,7}$	km	-	4.0	Broecker and Peng (1982), fig.2-15 p.77
$z_{19,8}$	km	3.5 - 4.0	3.75	Broecker and Peng (1982), fig.2-16 p.77
$\delta^{13}C_1$	‰	-	-7	Ruddiman (2001), fig.11-10 p.242
$\delta^{13}C_2$	‰	-	-22.0	Panchuk et al. (2008)
$\delta^{13}C_3$	‰	1.0 - 2.0	1.5	Broecker and Peng (1982), fig.6-13 p.310
$\delta^{13}C_4$	‰	1.5 - 2.4	1.95	Broecker and Peng (1982), fig.6-12 p.309
$\delta^{13}C_5$	‰	-	1.2	WOCE (1990-1998) Atlas volume 4 : Indian Ocean
$\delta^{13}C_6$	‰	0.5 - 1.5	1.0	Broecker and Peng (1982), fig.6-12 p.309
$\delta^{13}C_7$	‰	-	0.4	WOCE (1990-1998) Atlas volume 4 : Indian Ocean
$\delta^{13}C_8$	‰	-0.5 - 0.8	0.65	Broecker and Peng (1982), fig.6-12 p.309

Table 5: Parameters that are to be tuned and their test values. The values in bold are the values that were selected during the tuning, i.e., together, these values are the combination of parameters that gave the equilibrium solutions that were closest to the experimentally derived values.

Parameter	WK92 value	test values
R_{CO}	0.09	0.03, 0.045, 0.06, 0.075, 0.09 , 0.105, 0.12, 0.135
f_{PT}	0.925	0.9, 0.91, 0.92, 0.925 , 0.93, 0.94
C_{bio}	0.2	0.10, 0.15, 0.20, 0.25, 0.30 , 0.35, 0.40
R_{CP}	120.0	100.0, 110.0, 120.0, 130.0 , 140.0
vmv	10.5	9.45, 10.5 , 11.55
a_3/a_T	0.362033	0.2896 , 0.362033, 0.4344396
z_1	5.8	5.3, 5.8 , 6.3
uv	1.15	0.92, 1.15 , 1.38
z_2	50.0	40.0, 50.0, 60.0

TUNING

GENERAL METHOD

In the original work of WK92, the set of model parameters was qualitatively determined by arbitrarily selecting a set of parameters and then adjusting those parameters until a reasonable match to the experimental results was found. As an application to the sensitivity analysis described in the previous section, we have re-tuned the WK92 box model using the most sensitive model parameters.

The goal of tuning is to determine the parameter values that give equilibrium solutions that best reproduce experimentally derived values (Table 4). To achieve this, we must first find the experimentally determined values. Based on the nine most sensitive

parameters (Fig. 2), values between the minimum and maximum parameter value were chosen to be part of the tuning process (Table 5). The number of values chosen for each parameter, which ranged from three to eight, depended on the sensitivity of the parameter. Otherwise put, the more sensitive parameters required greater accuracy, and thus more values were used for their calculation.

Equilibrium runs involving every combination of these chosen parameter values were then implemented. This procedure can represent a tremendous number of runs and is why only the most sensitive parameters were used in the tuning. In our study, we performed 408 240 simulations (each running for a period of 2 million model years with a time-step of 1000 model years) to determine the best set of nine tuning parameters. Every set of equilibrium variables was compared to the set of experimental values using the following cost function:

$$(2) \quad \sqrt{\sum_{i=1}^{32} \left(\frac{Xe_i - Xp_i}{Xp_i} \right)^2}$$

where Xe_i is the i^{th} member of the 32 equilibrium solutions, and Xp_i is the i^{th} member of the 32 experimentally derived values. Again, the function is normalized (the difference $Xe_i - Xp_i$ is divided by Xp_i) so as to make the quantity in parentheses in (Eq. 2) dimensionless. A cost, or normalized cumulated root mean squared error, was calculated for every set of equilibrium solutions. Finally, the set of equilibrium solutions that had the smallest cost value was selected as the optimal set of parameter values and equilibrium solutions (Table 5).

EXPERIMENTAL DATA

We reviewed the literature to find experimental preindustrial values of the 32 dependent variables. Important sources for experimental values were *Tracers in the Sea* by Broecker and Peng and *Ocean Biogeochemical Dynamics* by Sarmiento and Gruber (3, 4). These texts provided us with the concentration of phosphate, alkalinity, the lysocline depth and $\delta^{13}C$ values for several of the model boxes. Moreover, the World Ocean Circulation Experiment (WOCE) website provided vertical cross section maps of the concentration of alkalinity, phosphate, $\delta^{13}C$ and total dissolved carbon for the Deep Indian Ocean and the thermocline (5). Although the WOCE data represents the present day, we assume that they are a reasonable representation of these two reservoirs in the preindustrial era. The $\delta^{13}C$ values for terrestrial biomass and the atmosphere were taken from Ruddiman (6). We often found plausible ranges of values rather than specific results, and therefore selected the value to tune by taking the

average of the maximum and minimum for a given range. Note that measurements in the thermocline vary tremendously as it is a non-homogeneous layer. The experimentally derived data for this reservoir were therefore estimates chosen from the middle of the thermocline layer. The 32 experimental values of the model variables and the associated references are listed in Table 4.

RESULTS

Figure 2 presents the averaged sensitivity index of the nine most sensitive parameters. The most sensitive parameter is R_{CO} . When tested from its initial value to its minimum value, we found a sensitivity index of 0.67 (Table 3). This implies that the 32 model variables change by an average factor of 0.67 when R_{CO} is changed from its initial value to its minimum. We find that other parameters, such as z_2 or α , are less sensitive and therefore less important since they change the model variables by a smaller factor. Some parameters, such as C_{surf} , have no influence on the model equilibrium solutions (Table 3).

Table 4 presents the 32 model prognostic variables, the experimental range of these variables and the selected value applied in the tuning procedure. The WK92 parameter values, the values examined in the tuning procedure, and the values that were selected from the tuning (bold) are given in Table 5.

DISCUSSION

SENSITIVITY

R_{CO} , the parameter that occurs in most of the model equations, is more sensitive than the other parameters. Hence, a change in its value will affect the model equilibrium solutions more than the other parameters, making it the most important tuning parameter. In addition, changes in certain parameters exhibit a sensitivity index of zero in equilibrium solutions (Table 3). This result can be explained by analyzing the model equations. Considering the C_{surf} parameter, Table 3 indicates that a change in the value of C_{surf} does not influence any of the equilibrium solutions. It does not, for example, affect T_s , the average global surface temperature. The equation relating C_{surf} and T_s is the following:

$$(3) \quad \frac{d}{dt} T_s = \frac{Q - F_{IR}(T_s)}{C_{surf}},$$

where the terms in the numerator of the right hand side represent incoming and outgoing solar radiation, respectively. At equilibrium, $dT_s = 0$, and since C_{surf} is constant, $Q - F_{IR}(T_s)$ must be zero. Hence, changing the value of C_{surf} will not affect the

equilibrium value of T_s , and accordingly, the sensitivity of C_{surf} with respect to T_s is zero. For this reason, C_{surf} is not a relevant tuning parameter. In a similar manner, the other parameters that exhibit a sensitivity index of zero are also not pertinent tuning parameters.

Note that for a simulation where carbon is being released into the atmosphere, $Q - F_{IR}(T_s)$ is not zero because the amount of outgoing solar radiation, $F_{IR}(T_s)$, is changing. In this case, the argument presented in the previous paragraph is not valid. Choosing two different values of C_{surf} for the same carbon emission scenario will indeed generate two different evolutions of T_s . Hence, although a parameter such as C_{surf} is irrelevant with respect to tuning the model, it is nevertheless important in the evolution of a simulation where the model is being forced by a release of carbon.

TUNING

We found that five out of the nine most sensitive parameter values resulting from our tuning procedure were identical to those determined by WK92 (Table 5). This is a strong affirmation of the parameters determined by WK92. Among the remaining four parameters, the difference between the original parameter values and those we calculated can be explained by the fact that our tuning procedure was more rigorous; it contained significantly more model simulations and a greater number of experimentally derived values for the dependent variables.

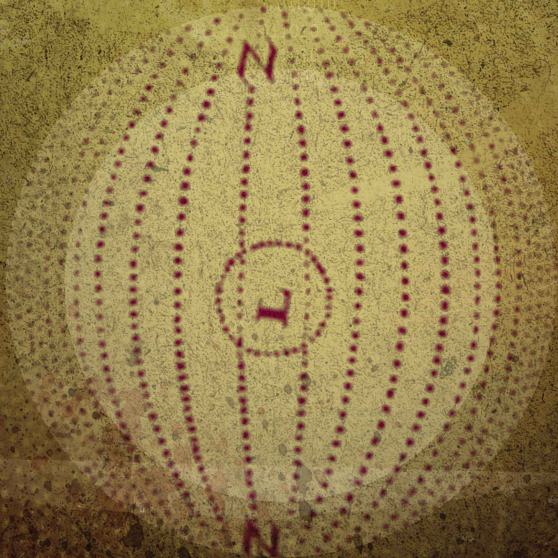
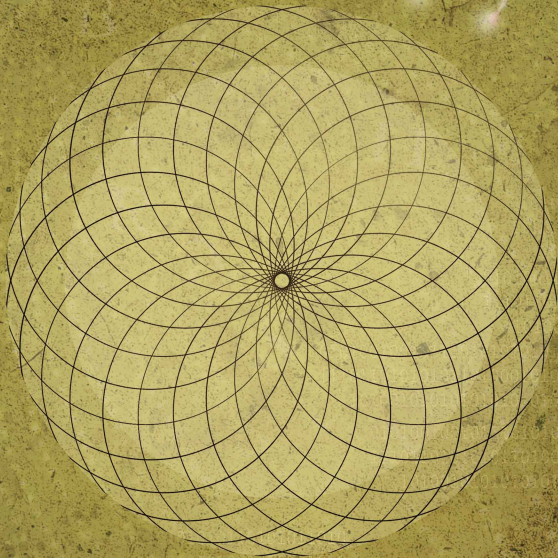
The goal of this study was to perform a sensitivity analysis on the parameters of the WK92 carbon cycle box model. The sensitivity analysis allowed us to understand which parameters most affected the equilibrium solutions and study how the model reacted to a change in parameter values. Furthermore, it permitted us to calculate the nine most sensitive parameters, to use this set of parameters to quantitatively tune the WK92 model and to compare and contrast our tuned parameter results to those originally determined qualitatively by WK92. In future work, these sensitivity results will be used to tune the WK92 box model to the Paleocene/Eocene boundary period (approximately 55 million years ago) so that it may be used to analyze the Paleocene Eocene thermal maximum, a period of abrupt and intense global warming (7, 8).

ACKNOWLEDGMENTS

S.Y. was supported by an Undergraduate Student Research Award from the Natural Sciences and Engineering Research Council of Canada (NSERC). This work was also supported by an NSERC discovery grant awarded to L.A.M.

REFERENCES

1. J.C.G. Walker, J.F. Kasting, *Palaeogeography, Palaeoclimatology, Palaeoecology* **97** 151–189 (1992).
2. W.D. Nordhaus, *Managing the Global Commons* (The MIT Press, Cambridge, Massachusetts, 1994).
3. W.S. Broecker, T.H. Peng, *Tracers in the Sea* (Eldigio Press, Lamont Doherty Geological Observatory, Palisades, 1982).
4. J.L. Sarmiento, N. Gruber, *Ocean Biogeochemical Dynamics* (Princeton University Press, Princeton, 2006).
5. WOCE, *World Ocean Circulation Experiment Atlas volume 4* (1990–1998) <http://www.pord.ucsd.edu/whp/atlas/indian/index.html>.
6. W.F. Ruddiman, *Earth's Climate, Past and Future* (W.H. Freeman and Company, New York, 2001).
7. G.R. Dickens, M.M. Castillo, J.C.G. Walker, *Geology* **25** 259–262 (1997).
8. D. Carozza, *Carbon cycle box modeling studies of the Paleocene-Eocene thermal maximum* (M.Sc. Thesis, McGill University, Montreal, Canada, 2009).



ISSN 1718-0775



01

9 771718 077004